LA-13688-MS

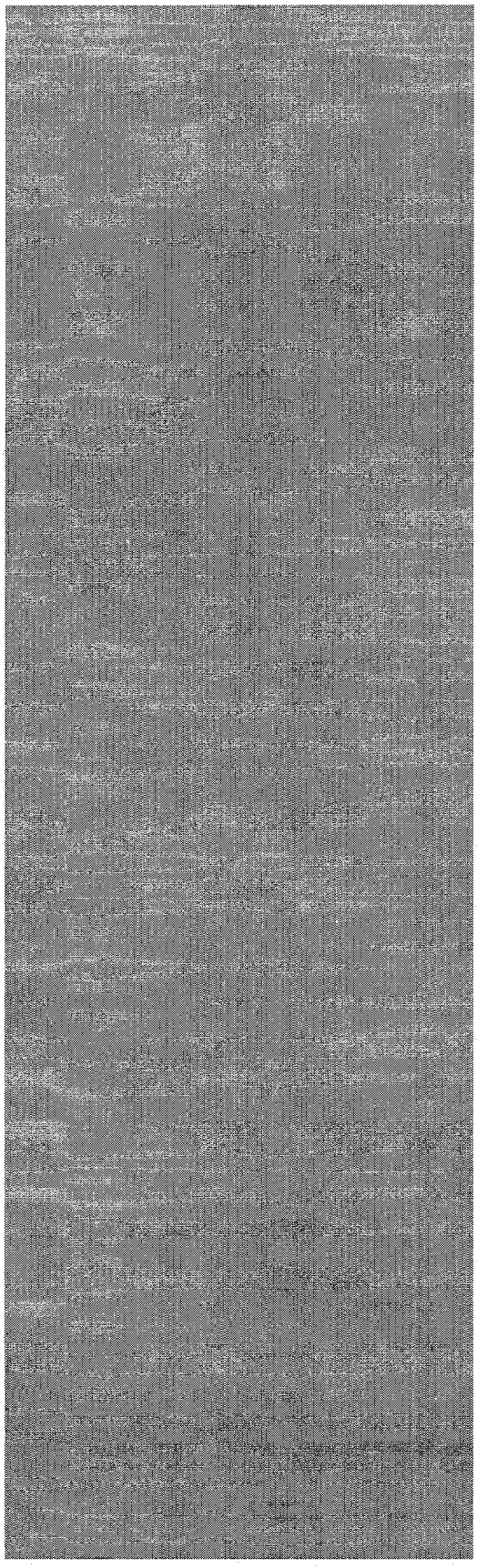

Calculations of the Response of Shielded Detectors to Gamma Rays at MeV-Range Energies

Los Alamos
NATIONAL LABORATORY

Los Alamos National Laboratory is operated by the University of California for the United States Department of Energy under contract W-7405-ENG-36.

Edited by Martha Lee DeLanoy, Group CIC-1

This work was supported by the U.S. Department of Energy, Office of Research and Development of the Office of Nonproliferation and National Security.

An Affirmative Action/Equal Opportunity Employer

DISCLAIMER

Portions of this document may be illegible in electronic image products. Images are produced from the best available original document.

LA-13688-MS

Issued: March 2000

Calculations of the Response of Shielded Detectors to Gamma Rays at MeV-Range Energies

R. C. Byrd

Los Alamos
NATIONAL LABORATORY
Los Alamos, New Mexico 87545

CONTENTS

CALCULATIONS OF THE RESPONSE OF SHIELDED DETECTORS TO GAMMA RAYS AT MeV-RANGE ENERGIES

by

R. C. Byrd

ABSTRACT

Nuclear instruments designed to detect gamma rays at energies from 0.1 to 10 MeV respond primarily to the electrons produced by gamma-ray scattering and absorption in either the instrument itself or in the surrounding materials. Although tabulated attenuation coefficients are very useful for estimating macroscopic quantities such as bulk energy depositions, such quantities are averages over several different phenomena at the microscopic level. For detectors with active elements that are thin compared with an electron range, the competing effects of inscattering and outscattering result in complicated responses, as evidenced by the strong energy dependence of the resulting pulse-height spectra. Thus, for some applications the macroscopic averages are entirely sufficient, but for others a full microscopic analysis is needed. We first review the literature on the responses of several types of detectors to gamma rays at energies below 10 MeV, and then we use a series of simple Monte Carlo calculations to illustrate the important physics issues. These simple calculations are followed by thorough studies of the energy and angle responses of two proposed instruments, including their responses to instantaneous pulses of large numbers of simultaneous incident photons.

---

1. INTRODUCTION

Objective. This report presents calculations of the gamma-ray responses of two of the three programmatic detectors being proposed for the next generation of space-based instruments deployed to verify international nuclear arms-control treaties. Such calculations are a significant departure from the largely empirical approach used to design the previous systems. For example, the corresponding detectors in the current version of the Advanced Radiation Detection System (Advanced RADEC II, or ARII) were based on observations of nuclear testing obtained using earlier space- and ground-based systems. The proposed detectors have no such direct heritage, yet they must provide comparable performance with much more modest physical resources. To compensate, the proposed system uses sophisticated correlations between a variety of measurements in order to reliably detect and identify candidate nuclear events against the varying background of space radiation. In turn, these analyses require a

detailed understanding of the detectors' response to both the signal and backgrounds; without testing, however, that understanding can only come from computer simulations like those presented here.

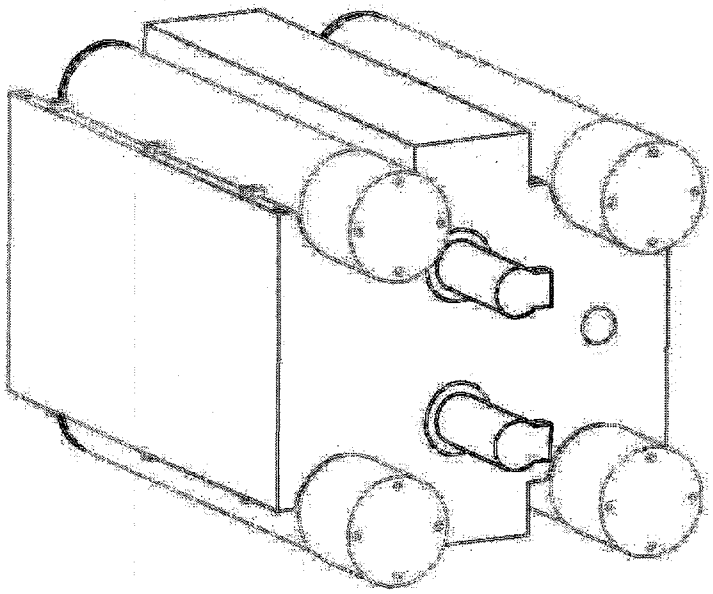

Figure 1.1. Layout of the proposed SABRS instrument package, showing the four SPG plastic scintillators embedded in the corners of the SAN detector's polyethylene moderator.

Detector Layout. The most obvious difference between the present and proposed instruments is the physical arrangement of the detector components. To minimize size and mass, SABRS (Space and Atmospheric Burst Recording System) combines the SPG prompt gamma-ray detector and the SAN neutron detector in a single package rather than using separate instruments. One view of the current layout is shown in **Figure 1.1**. For the SPG instrument, the critical issue is the identification of a candidate nuclear event by requiring a fast coincidence between four separate plastic scintillators. In order to reduce the rate of chance fourfold and cosmic-ray twofold coincidences, these scintillators should be separated as widely as possible within the overall package. As shown, the four scintillators are therefore placed along the outer corners of the combined SPG/SAN package. The SAN instrument, like the neutron detector in the existing system, is based on multiple polyethylene-moderated ^{3}He counters. As described in Ref. 1, the dimensions of the polyethylene block and the locations of the two main ^{3}He tubes were chosen primarily to maximize the fast-neutron counting efficiency per unit mass. In the combined instrument package, the polyethylene moderator for the SAN detector provides low-Z shielding for the SPG plastic scintillators, which in turn provide additional moderation for incident neutrons.

Coupled Responses. The combination of the SPG and SAN instruments in a single package results in several questions about the gamma-ray responses of the two detector systems. For the SPG instrument, the asymmetric layout, the large amount of low-Z shielding, and the fourfold coincidence are all unusual features for a prompt gamma-ray detector. For the SAN instrument, the standard goal of gamma-ray rejection is complicated by a proposal to use current measurements to extend the detector's dynamic range beyond that for conven-

tional pulse counting. Basically, pulse counting rejects gamma rays by means of a pulse-height threshold, but current measurements include both neutron and gamma-ray contributions. This ambiguity suggests that estimates of the SAN gamma-ray response be included as a natural adjunct to the SPG calculations. The present report therefore covers the gamma-ray responses of plastic scintillators and ^{3}He ionization counters, as well as the effect of different shielding options. Furthermore, because neither the SPG nor SAN detector exists in even prototype form, we also include the corresponding calculations for comparison with results for two existing ARII instruments, the Advanced Prompt Gamma (APG) detector and the X-ray Detector System (XDS). We do not include calculations for the third SABRS programmatic detector, the SDG (SABRS Delayed Gamma) instrument, which is physically separated from the SPG/SAN package and has no impact on its design. Furthermore, optimizing the SDG detector primarily involves minimizing the production of bremsstrahlung background by incident high-energy electrons, which would require a completely separate set of calculations.

Effective Areas. One issue central to the present work is the use of effective detector areas instead of the more customary efficiencies, which are defined as the probability of detecting a particle that strikes the detector surface. In its simplest form, the effective area (or area-efficiency product) is calculated by multiplying the efficiency by the detector's projected area: $A_{\text{eff}} = \varepsilon A$. An operational definition of A_{eff} that greatly simplifies its calculation for complicated geometries merely divides the number of detected particles N by the incident particle fluence Φ_N. For our application, a related quantity is the deposited energy E produced by an incident energy fluence Φ_E, which can be regarded as the area of an equivalent "black" detector that is totally absorbing for incident energy instead of particles. For incident plane waves, effective area is therefore similar to the absolute efficiency commonly used for point sources, which is calculated as the product of the efficiency ε and the solid angle subtended by the detector. Just as absolute efficiency makes it easy to calculate count rates for point sources, for our plane-wave application the effective energy-absorbing area A^E_{eff} provides a direct connection between the incident signal, the detector, and the resulting output.

Electron Transport. Another recurring issue in the present calculations is the central importance of electron transport for the response of a variety of detectors to incident gamma rays at energies from 100 keV to 10 MeV. At lower energies, the physics of gamma-ray interactions can usually be adequately represented by the photoelectric absorption calculated using simple attenuation coefficients.[2] At MeV-range energies, however, the most important interaction process is Compton scattering, which produces energetic electrons in both the detector and the surrounding materials. For detectors like the SPG and APG scintillators, the dimensions are usually large compared with the electron range, so electron transport across the detector boundaries has only a small effect except at the highest energies. If the detector's sensitive volume is thin, however, the most important electron source is often its surroundings, which are commonly referred to as gamma-ray converters or as radiators of secondary electrons, concepts often associated with neutron interactions. Regardless of the origin of the electrons, most escape from a thin detector without depositing their full energy. Nevertheless, in our energy range the calculations repeatedly show that the net deposited energy is very similar to that for a bare detector in which all the recoil electron energy is deposited at the interaction site. In short, all the deposited energy comes from electrons, and the gain from the surroundings nearly compensates for the loss to escape. Because this assumption is exactly the one made by the macroscopic attenuation coefficients, the simple calculation gives almost

the correct answer, although certainly for the wrong reasons. This remarkable result recurs throughout our discussion.

Contents. After this introduction in Chap. 1, Chap. 2 uses a literature search as the basis for a set of calculations with simple slab geometries, which illustrates much of the physics for gamma-ray interactions in shielded and unshielded ^{3}He ionization chambers and in plastic scintillators. The ionization chambers represent a simplified version of the SAN detector, and the shielded scintillators correspond to the SPG detector. To provide a comparison with existing instruments, this discussion is followed in Chap. 3 by a study of the corresponding behavior for the Si photodiodes in the APG and XDS detectors. In the energy range from 0.1 to 10 MeV, all of these topics are related by mechanisms of electron production and transport. Chapter 4 then adapts the results from these simple slab geometries to studies of the energy- and angle-dependent detection efficiencies of the more complex SPG geometry. Chapter 5 follows an aside to investigate a technique that uses the ratios between the responses of the four scintillator elements to estimate the direction of the incident gamma-ray signal. Chapter 6 returns to the calculated pulse-height responses to develop a technique for converting the calculated response to single incident photons into the corresponding response to a single pulse containing a large number of simultaneous photons. Chapter 7 repeats the scintillator analyses for the detection efficiency, directionality, and pulse response for the case of the ^{3}He counters in the SAN instrument. A summary and suggestions for further work are given in Chap. 8.

2. BASIC DETECTOR PHYSICS

Overview. A recurring theme in this report is the importance of electron transport in understanding the response of nuclear instruments to gamma rays in the energy range from 0.1 to 10 MeV. Gamma-ray response is the central design issue for the SPG instrument, and gamma-ray rejection is almost as critical for the SAN instrument. As discussed in Chap. 1, many of the important issues of gamma-ray transport and secondary-electron production are most obvious for detectors with thin active elements, for example, for ^{3}He gas instead of plastic scintillators. For the SAN detector, the dominant response mechanism at the energies of interest is the production of Compton electrons in the polyethylene moderator and the stainless-steel counter walls, not the direct interactions in the ^{3}He gas. In Sec. 2.1 we therefore begin with a discussion of gamma-ray interactions in ^{3}He ionization chambers, and we follow in Sec. 2.2 with calculations for a simple version of such a detector. In Sec. 2.3 we investigate the behavior of a similar CH_2+Ta+BC400 setup that represents the BC400 scintillators in the SPG detector. In Chap. 3 we discuss similar issues for other detector arrangements that represent the shielded Si photodiodes used in several existing ARII instruments. Finally, in Chap. 4 we return to the actual SPG geometry in order to adapt our basic discussion to the more detailed analyses of the responses of the SPG and SAN instruments as functions of incident gamma-ray energy and angle.

2.1. ^{3}He Neutron Counter Literature

Gamma-Ray Interactions. Fundamentally, all nuclear instrumentation operates as ionization detectors, so discriminating between uncharged neutrons and gamma rays usually requires distinguishing between the electrons produced by gamma-ray interactions and the recoil products from neutron scattering or capture reactions. The two production rates are comparable at MeV-range energies, so the key feature is the much lower ionization density produced by the lightweight and hence rapidly moving electrons. The most common discrimination technique simply sets a pulse-height threshold that accepts the recoil signals but eliminates the smaller pulses caused by electrons. For example, the neutron detectors in this report are based on the n+^{3}He capture reaction, whose p+^{3}H reaction products together have a recoil energy of 764 keV, most of which is deposited very near the reaction site. For comparison, the electrons from a 1-MeV gamma ray can deposit at most a few keV along an ionization track that crosses the entire gas volume. In both cases charge multiplication occurs in a small region around the anode wire, but the difference in charge localization results in a slower rise time for the gamma-ray pulses, which could in principle provide a basis for gamma-ray rejection. Unfortunately, nuclear radiation fields contain large numbers of gamma rays, so eventually the interaction rate reaches the point where pileup of even small gamma-ray pulses can cross the threshold for single-neutron detection. Even in the absence of pileup, the neutron interaction rate can exceed the pulse-counting capability of the electronics, which causes count-rate losses and eventually system paralysis. Previous satellite-based neutron detectors for treaty verification have avoided this problem by using multiple detectors with three different sensitivity ranges.[3] To reduce the numbers of electronic channels in the proposed SAN detector, however, the suggestion was made to use current-mode operation to extend the dynamic range beyond the pulse-counting regime. This suggestion therefore requires developing a detailed understanding of gamma-ray interactions in ionization detectors. To summa-

rize, there are three instrumental issues that must be dealt with in different combinations of pulse or current mode:

(1) dead-time losses at high neutron counting rates,
(2) gamma-ray pulse pileup that crosses the neutron threshold, and
(3) combined electron and charged-particle currents in mixed radiation fields.

On the basis of these issues, in our application there should occur three very different situations:

(1) For the instantaneous gamma-ray flash, pulse counting is impossible, but the signal may be large enough to trigger the neutron threshold.
(2) During the earliest part of the neutron signal, the instrument should be in pulse-counting mode, perhaps with significant dead time; there should be no counts from gamma-ray pileup, but there may be significant current from interactions of delayed gamma rays.
(3) Eventually, the neutron signal may die away but the delayed gamma rays will persist; again, the neutron threshold should not be exceeded, but the gamma-ray current may be measurable.

Gamma-Ray Rejection. A survey of the literature on ionization chambers[4] reveals several approaches for reducing the effect of incident gamma rays. The most direct technique is "balancing," in which the charge produced in a neutron counter is corrected by the compensating charge produced in a similar neutron-insensitive chamber. In the usual implementation,[5] the electron current generated between two dissimilar electrodes is measured and a compensating voltage is used to adjust the net output current to zero in the presence of a pure gamma-ray field. Given that our dynamic-range problem originated from the desire to avoid additional neutron counters, this balancing approach is of little advantage. More seriously, some form of realistic testing would be required in order to validate the technique for our very dynamic mixture of neutron and gamma-ray signals. For electron linacs, a second form of cancellation[6] uses two identical ^{3}He chambers and exploits the time correlation between the currents produced by the gamma-ray flash as compared with the uncorrelated pulses from arriving neutrons. By using a differential amplifier to sum the signals from the two chambers, the base-line shift caused by the gamma-ray flash can be cancelled while preserving the neutron pulses. In our case, however, the neutron signal is well separated from the gamma-ray flash, and the pulses for delayed gamma rays are not correlated for the two ^{3}He tubes. Accordingly, such balancing approaches are not particularly useful for our application. A more promising approach is referred to as the "Campbelling" technique,[7] which is widely used to extend the dynamic range of pulse-counting systems in reactor instrumentation. Basically, the amplitudes of the ionization pulses from the detector are integrated by a root-mean-square averaging circuit that increases the amplitudes of the large charged-particle pulses relative to the smaller gamma-ray pulses. Again, in view of the rapidly varying nature of our neutron and gamma-ray signals, such time-averaging techniques would need to be evaluated carefully. Perhaps the most relevant reference[8] is a recent empirical study of the gamma-ray sensitivity of ^{3}He neutron counters similar to those in the present proposal. The study focuses on optimization of the counter design with respect to gas mixture and pressure and to wall material and thickness, but the application, analysis, and conclusions are decidedly different from those of the present work. The presumed reasons for the discrepancy will be discussed below. In short, although some of the techniques in the literature may be adaptable to the present application, none could be readily adopted without further development.

2.2. Moderated ^{3}He Counter Tests

Layout. As suggested by some of the above references,[4,8] gamma-ray response at the MeV-range energies of interest can be a complicated combination of photoelectric absorption and Compton scattering in both the detector and its surroundings. Instead of investigating such issues using the complex SPG/SAN package, we can construct a series of slab-geometry setups that allow us to investigate the physics questions in a much simpler context. In particular, the use of slab geometries allows us to easily compare the results of our calculations with absorption estimates obtained from the standard Storm and Israel (SI) attenuation coefficients.[2] Because our discussion suggests that the central issues of electron transport are most dramatic for detectors with thin active elements, we begin our study with polyethylene-moderated ^{3}He ionization counters. **Figure 2.1** shows a schematic view of the test layout. The gamma rays are incident as a parallel plane wave from the left onto a 1-cm^2 detector face. The successive layers are 5 cm of polyethylene, 0.1 cm of stainless steel (SS), and 2 cm of ^{3}He gas at a 4-atm pressure, which form a narrow stack of materials with no backing. The thicknesses are not meant to be exact reproductions of the actual SPG materials, just as our narrow one-dimensional geometry cannot accurately reflect the competing effects of inscattering and outscattering in the true geometry. Our approach will instead emphasize changes in the response as we construct different versions of this hypothetical detector: bare ^{3}He alone, shielded SS+^{3}He, and the full CH_2+SS+^{3}He setup.

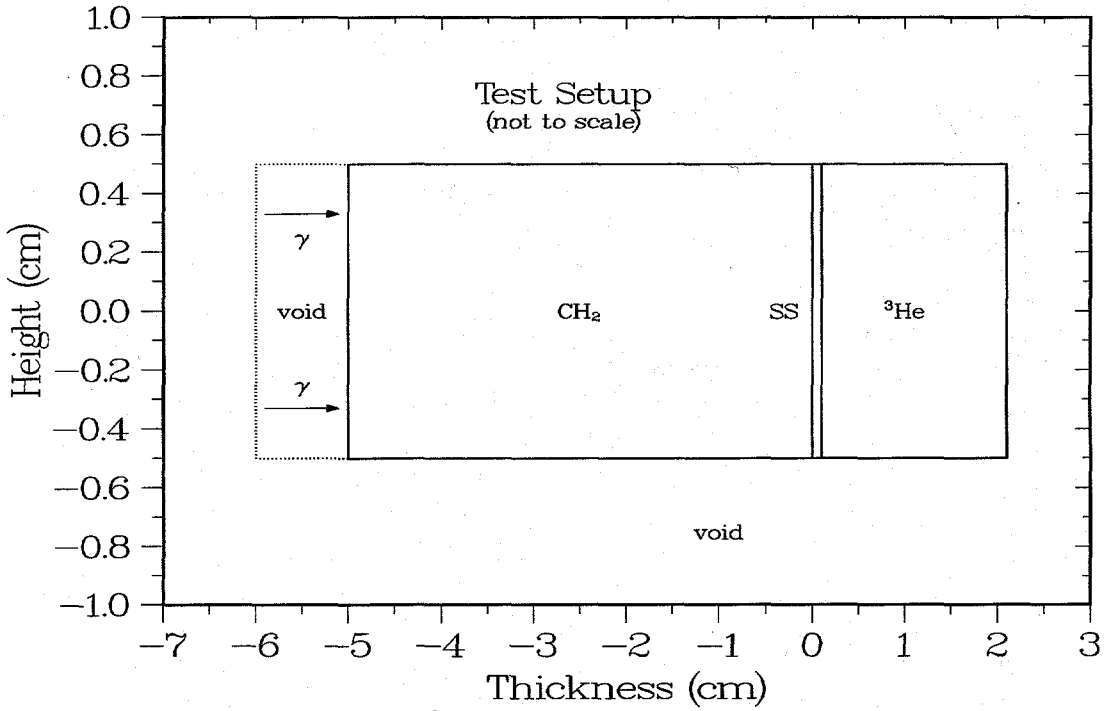

Figure 2.1. Layout of the ^{3}He test setup used to explore the effect of different arrangements of materials on the SPG and SAN gamma-ray responses.

Calculation Technique. The calculations throughout this report use the MCNP4A Monte Carlo radiation transport code[9] with photon and electron libraries obtained from the Radiation Safety Information Computational Center (RSICC).* Sensitivity tests were also

* RSICC, P.O. Box 2008, Oak Ridge, TN 37831-6362.

made with the current MCNP4B version of the code; as shown in Chaps. 4 and 7, differences are sometimes apparent but they do not affect our conclusions. Our calculations focus on the connection between the incident gamma rays and the production and transport of secondary electrons. Although these electrons could in turn produce secondary photons through bremsstrahlung, there is no evidence that such processes are significant when compared with the incident gamma-ray signal itself. Similarly, for environmental monitoring of electron fluxes, the interactions of the electrons themselves are more important than the effect of any bremsstrahlung they produce. Thus, only four different tallies are used to accumulate quantities of interest: an F2 current tally for electrons crossing a surface; an F4 flux tally of particles tracks averaged over a volume; an F6 heating tally for the total energy deposited within a volume; and an F8 pulse-height tally of the energy deposition by individual photons. The difference between the F6 tally for average heating and the F8 tally for individual energy losses will be a crucial issue in our discussion. For comparison with the MCNP results, calculations of the gamma-ray energy absorption are also made using the SI attenuation coefficients. Although the two resulting curves cannot be distinguished in Figure 2.2, these coefficients include options for either escape or absorption of the Compton-scattered photon. In contrast, both options assume that all recoil electron energy is deposited at the site of interaction.

Basic Quantities. A first look at the behavior of the calculations comes from **Figure 2.2**, which shows the energy deposited in the ^{3}He gas for several variations of the test setup. The energy deposition has been expressed as an effective energy-absorbing area by dividing by the incident energy fluence in MeV/cm^2; for our 1-cm^2 surface area, this fluence is numerically equal to the incident photon energy. The curves show SI absorptions; most of the plotting symbols show the same quantities as obtained from monoenergetic MCNP heating tallies. The different results are for the bare ^{3}He gas (dotted and ◇), for the SS-shielded gas (dashed and ○), and for the full CH_2+SS shielding (solid and ●). The three most prominent features are the rapidly decreasing photoelectric absorption below about 20 keV, the onset and broad plateau for Compton scattering above 50 keV, and the rapid SS shielding cutoff at about the same energy. Note that the added CH_2 shielding can only attenuate the incident fluence and reduce the energy deposition, because the model allows only outscattering, not inscattering. In general, the agreement between the two sets of results is excellent, although the somewhat higher MCNP values suggest that there are some three-dimensional effects caused by the longer path lengths associated with a diverging secondary-electron beam. Also shown in the figure, however, are the results from MCNP pulse-height tallies at 10 keV, 100 keV, and 1 MeV for the same shielding arrangements: ^{3}He, SS+^{3}He, and full CH_2+SS+^{3}He. These effective areas were calculated as energy-weighted sums of the pulse-height tally per energy bin; alternatively, a *F8 energy-deposition tally could have been used, which does not provide a spectral distribution but does allow use of variance-reduction techniques. For the bare ^{3}He case in particular, the agreement remains excellent at 10 keV, but it becomes questionable at 100 keV and is very poor at 1 MeV.

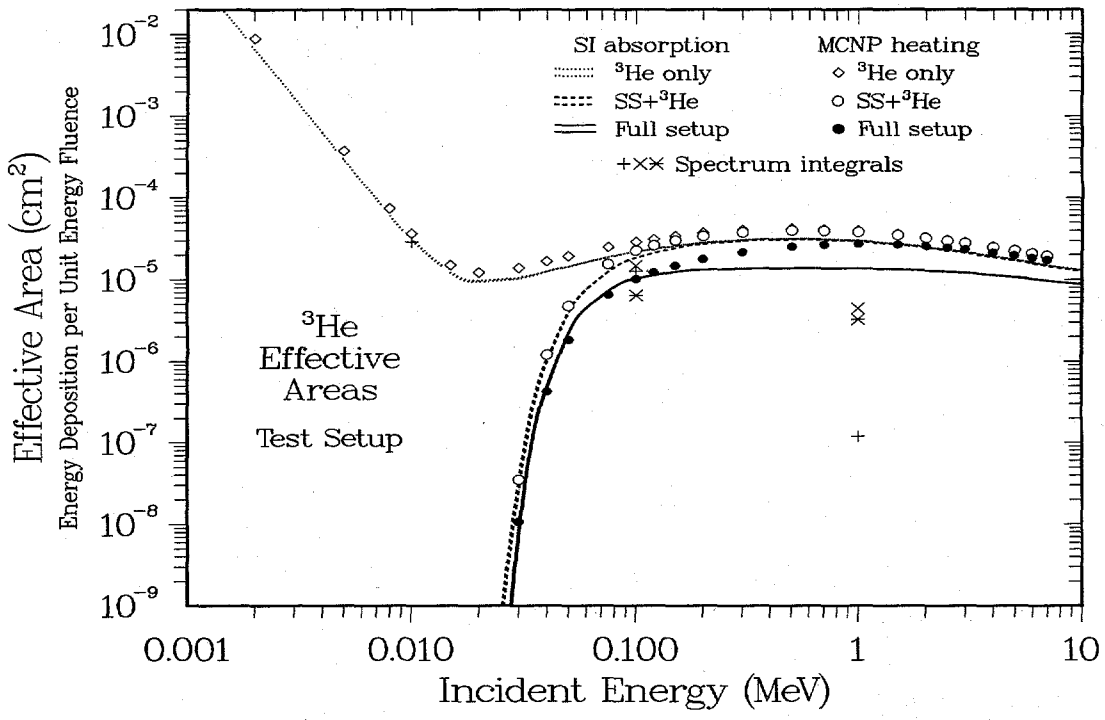

Figure 2.2. Energy dependence of the effective energy-absorbing area for different arrangements of the ^{3}He test setup in Figure 2.1.

Deposited-Energy Spectra. The key to understanding the discrepancies for the pulse-height tallies in Figure 2.2 is contained in the differential pulse-height spectra shown in **Figure 2.3**, **Figure 2.4**, and **Figure 2.5** for the three different energies. If within range, in each case the expected location of the Compton edge is shown by a vertical arrow. The energy-weighted sum of the counts in the spectrum gives the effective areas shown in Figure 2.2. At 10 keV (Figure 2.3) the spectrum consists of a Compton distribution, a prominent photopeak, and a few counts at intermediate energies that can only result from multiple scattering. This interpretation is consistent with the energy dependence shown in Figure 2.2, where the 10-keV point is almost at the end of the region dominated by photoelectric absorption. At 100 keV (Figure 2.4) the spectrum contains neither a photopeak nor a Compton edge, but there is a suggestion of structure in the spectrum, which indicates the onset of more complex interaction processes. Inspection shows that adding the SS shielding causes a big increase in the spectrum at low pulse heights but little change at high pulse heights. This behavior suggests that counts at low pulse heights are associated with Compton electrons from the SS that have lost some of their energy before reaching the gas. Conversely, the counts at the highest pulse heights are from interactions in the gas. Adding CH_2 reduces the magnitude of the spectrum but does not greatly affect the shape, which is consistent with simple attenuation in the added material. Electron energy-loss tables indicate that the maximum energy deposition in the gas should be about 14 keV, which explains the absence of a Compton edge at 28 keV. Next, at 1 MeV there is almost no response from the bare ^{3}He gas. Adding the SS shielding gives a large increase in the signal, and there is again clear indication of structure in the spectrum. We also point out that the behavior of the calculated spectra shown here is very similar to that of the measured spectra for Si diodes shown in Ref. 10. Finally, for contrast **Figure 2.6** shows the corresponding MCNP spectrum as calculated without electron transport. The nonelectron spectrum contains about 1/40 the number of counts, but the average energy depo-

sition per interaction is more than 30 times greater, so the resulting effective area agrees to within about 20%. However, this spectrum is clearly unphysical, because no electron track across the ^{3}He gas volume can deposit 0.8 MeV.

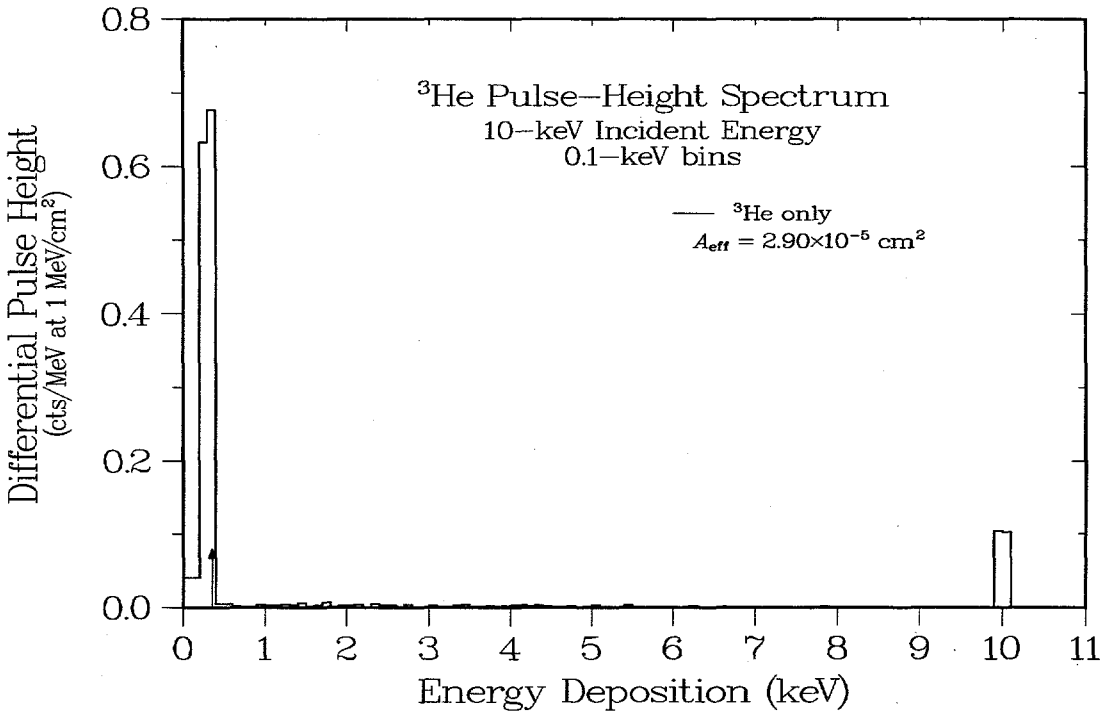

Figure 2.3. Pulse-height spectrum produced by interactions of 10-keV gamma rays with the unshielded ^{3}He gas volume in Figure 2.1. The energy-weighted area leads to the effective area in Figure 2.2.

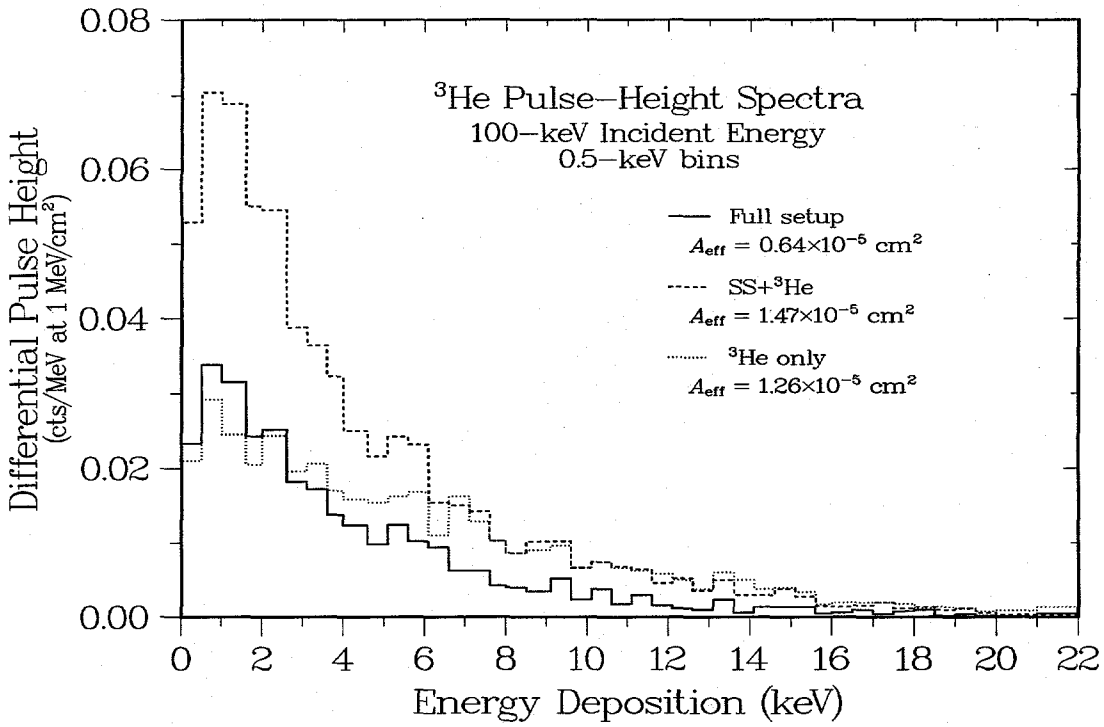

Figure 2.4. Pulse-height spectra as in Figure 2.3, but for 100-keV incident gamma rays and different combinations of shielding materials.

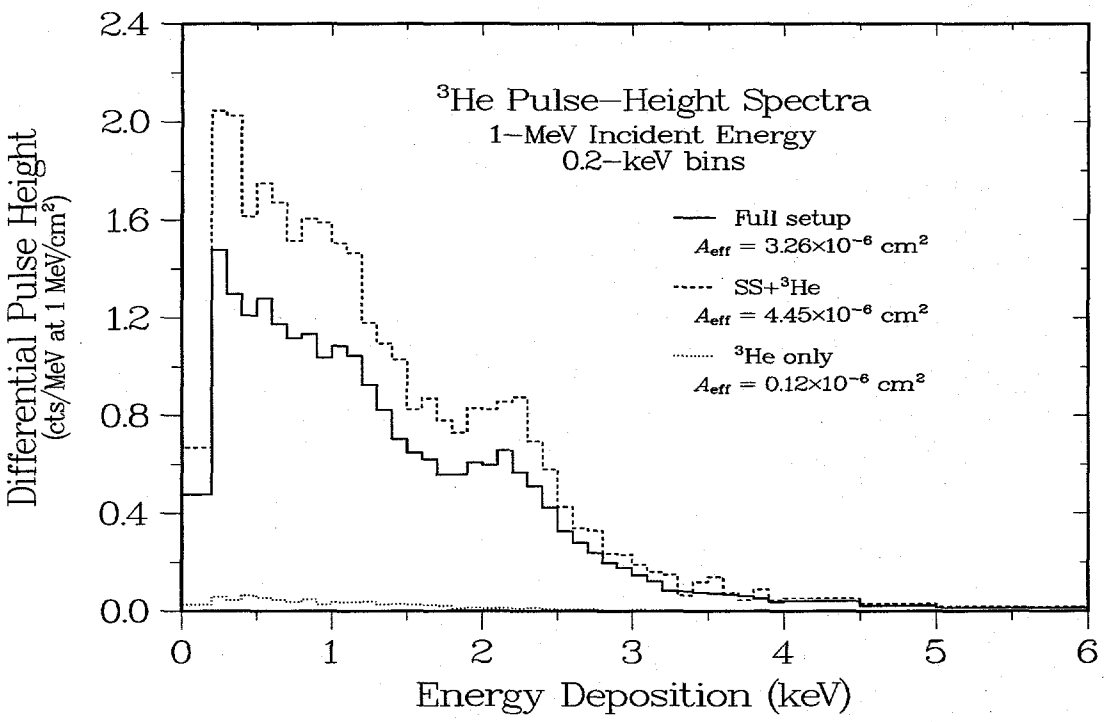

Figure 2.5. Pulse-height spectra as in Figure 2.4, but for 1-MeV incident gamma rays.

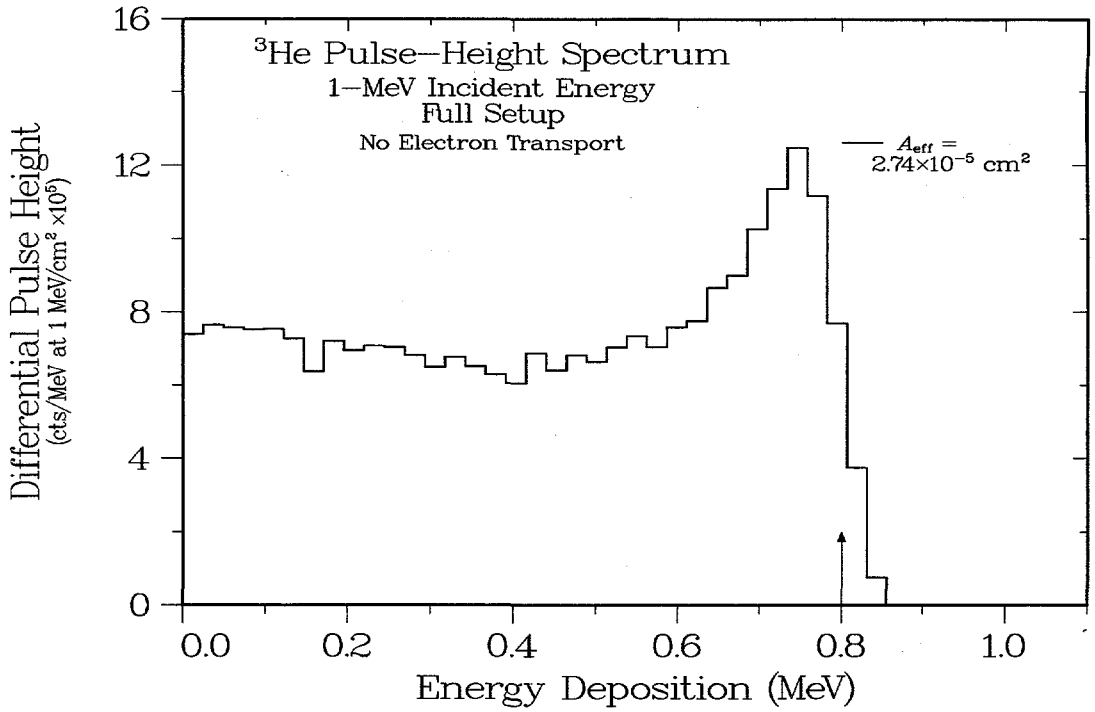

Figure 2.6. Pulse-height spectrum for 1-MeV incident photons as in Figure 2.5, but calculated without electron transport.

Electron Fluences. As a check on the interpretation of the 1-MeV spectrum in Figure 2.5, in **Figure 2.7** we show the electron flux crossing the boundary between the SS shielding and the ^{3}He gas. The mean energy value is at about one-half the incident energy, and the high-energy cutoff is consistent with a Compton energy of 0.8 MeV. Again, adding the layer of CH_2 changes only the magnitude of the spectrum, not its shape. For electrons at these energies, the range in SS is about 0.25 g/cm^2, or 0.03 cm—that is, the secondary-electron emission is clearly a skin effect. In the ^{3}He gas, electrons at 0.4–0.8 MeV have an expected energy loss of about 2.0–2.7 keV, just as seen in Figure 2.5. Finally, the areas and energy losses for Figure 2.5 and Figure 2.7 are completely consistent with the A_{eff} values shown as spectrum integrals in Figure 2.2. Thus, the important features for energy deposition in ^{3}He gas at MeV-range energies are all consistent with production of secondary electrons in the surrounding SS shielding. It is also important to note that the situation becomes even more complicated at energies above 1.5 MeV, because Compton electrons from the CH_2 begin to penetrate the SS shielding and interact with the ^{3}He gas.

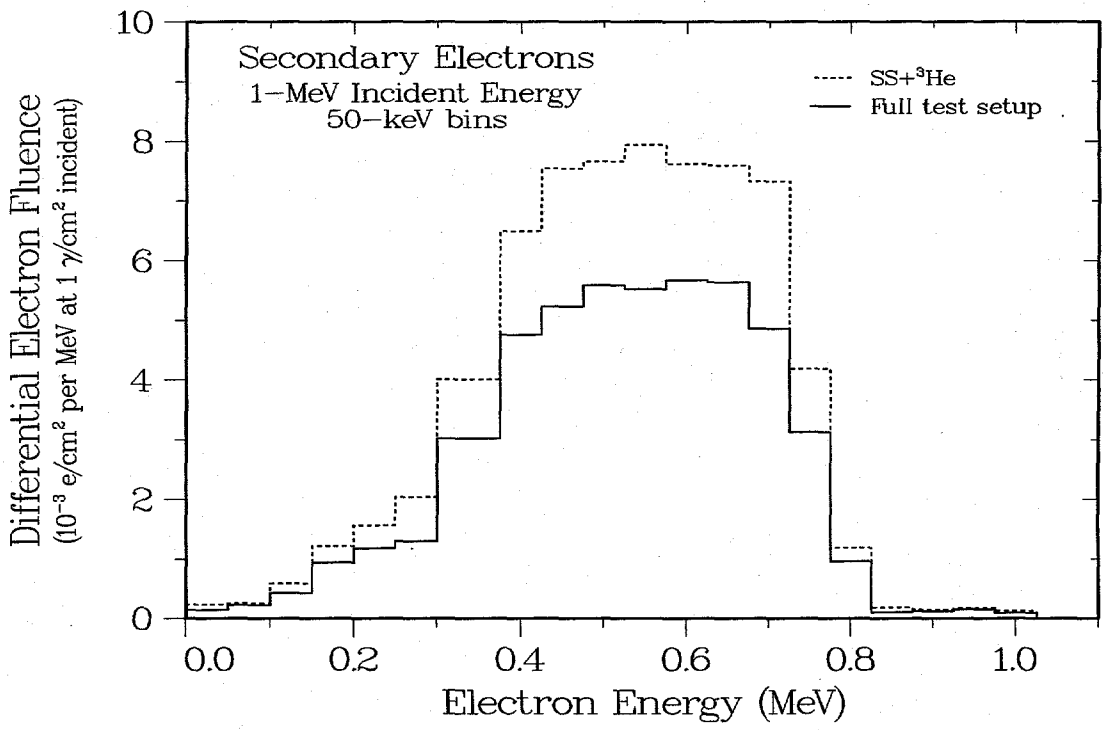

Figure 2.7. Electron fluence spectra corresponding to the 1-MeV pulse-height spectra in Figure 2.5.

Complete Model. Using the insight provided by the pulse-height and electron spectra, in **Figure 2.8** and **Figure 2.9** we can replot the effective areas from Figure 2.2, but now including electron-transport effects by using MCNP pulse-height tallies (spectrum integrals) instead of heating values. The MCNP ^{3}He-only values (◇) follow the corresponding SI curve up to about 70 keV, where the gas thickness can no longer completely stop the Compton electrons; as the spectrum behavior changes from E to ΔE, the energy deposited, and hence the effective area, begins to decrease. Adding the SS shielding (○) has two effects: it introduces the expected low-energy cutoff, and above 400 keV it increases the number of electrons entering the gas, which causes the effective area to rise almost to the SI value. Finally, adding the CH_2 layer (●) increases the attenuation at lower energies, but at higher energies it contributes additional electrons to the gas, which causes the effective areas above 4 MeV to increase slightly. Our interpretation is consistent with the results for shielded ionization counters reported in Ref. 4, which indicate that the count rate in the gas increases almost tenfold as the incident gamma-ray energy increases from 279 keV to 2.7 MeV. When count rate is converted to effective area by assuming a ΔE spectrum and dividing by the incident energies, the result is the essentially constant A_{eff} value observed here. Finally, the comparison between Figure 2.2 and Figure 2.8 emphasizes that MCNP heating tallies and SI energy absorptions must be used with care. The two approaches give consistent results because an MCNP heating tally transports the gamma rays through the materials between successive interactions by assuming simple photon attenuation. Although calculationally efficient, this approach can be seriously in error for thin layers.

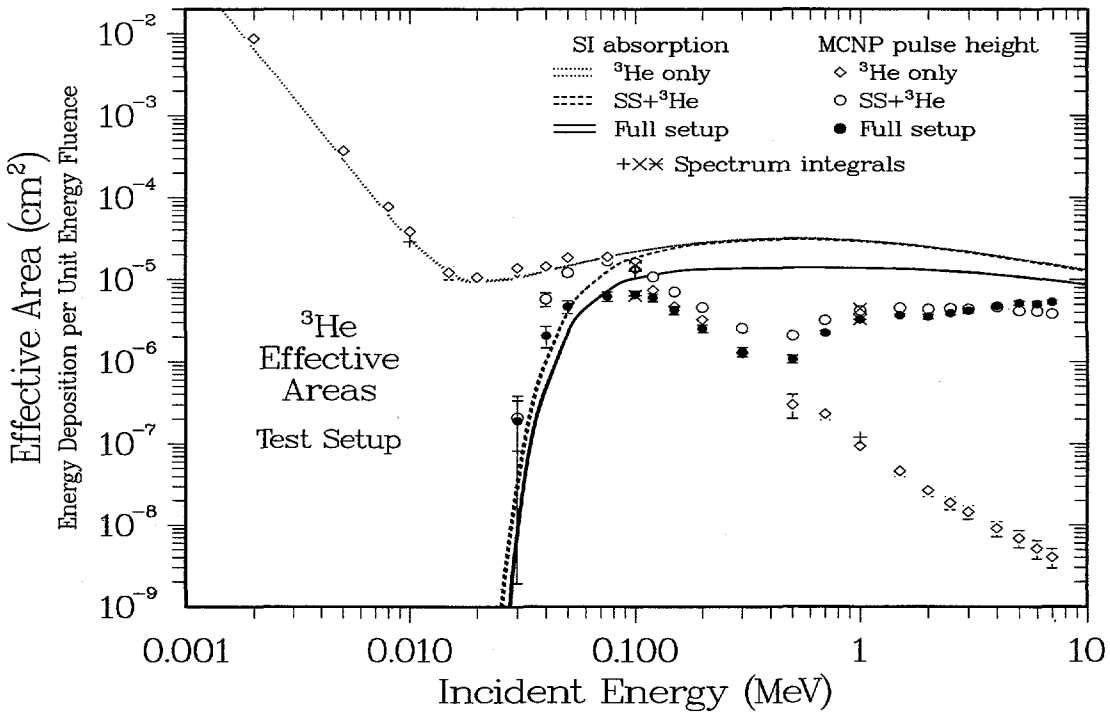

Figure 2.8. Complete effective-area excitation functions for various arrangements of the shielding materials in Figure 2.1. (Compare with the corresponding heating calculations in Figure 2.2.)

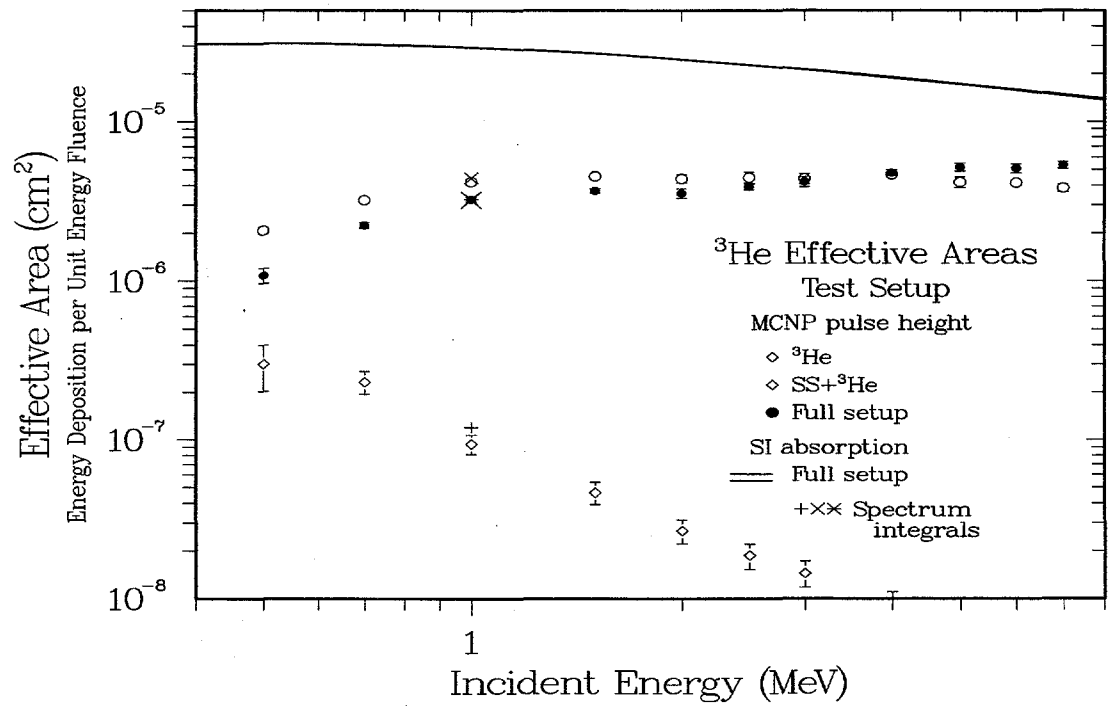

Figure 2.9. Detail of Figure 2.8, showing the effective areas for the full shielded detector over the region of greatest interest.

Gas Mixtures. One issue for actual counters is the addition of small amounts of electronegative gases such as Ar to the pure ^{3}He assumed in the above calculations. As discussed

in Ref. 8, this addition reduces the operating voltage and can improve the pulse rise time, but it also introduces a high-Z gas component that may increase the counter's gamma-ray sensitivity. Based on ^{3}He:Ar gas mixtures[11] that vary from 2:1 to 98:1, we have rerun our effective-area calculations assuming a 5% Ar gas mixture. The SI and MCNP results shown in **Figure 2.10** indicate that the effect for the bare ^{3}He+Ar mixture can be very large at low energies, but at high energies it is almost negligible when compared with the contribution from the SS shielding in the full assembly.

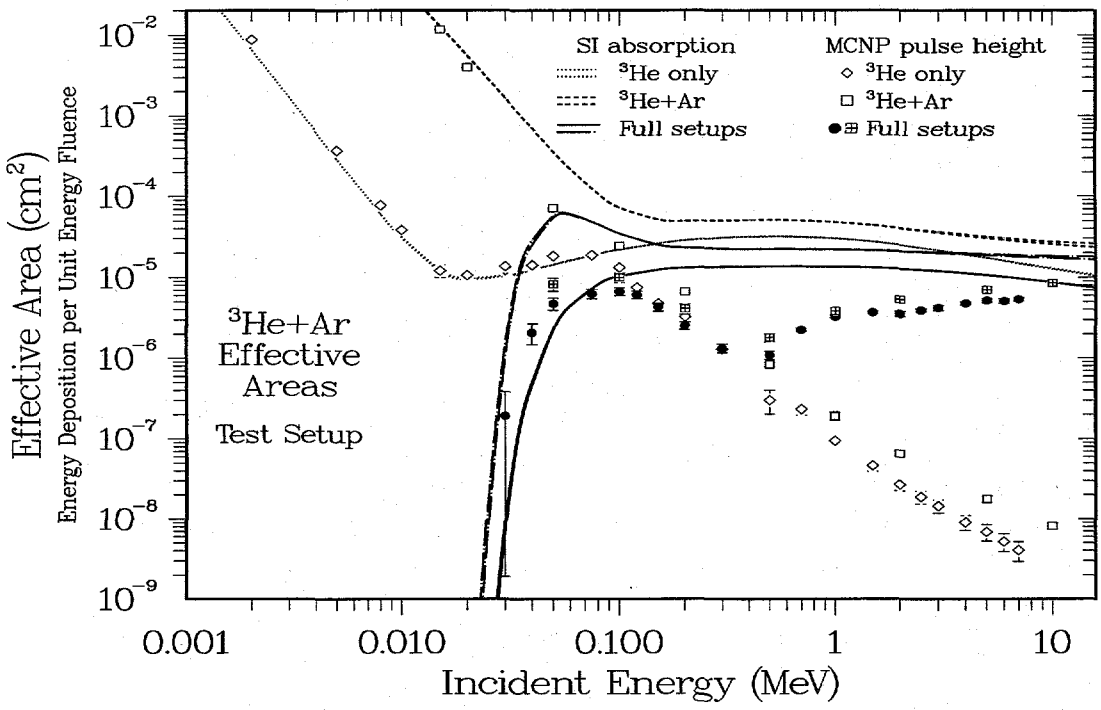

Figure 2.10. Effective areas as in Figure 2.8, but for counter tubes containing either ^{3}He only or a 20:1 mixture of ^{3}He+Ar gases.

Shielding Variations. Another important issue for actual counters is the choice of material for the chamber walls. Again, it is reasonable to expect that the use of higher-Z components will result in increased gamma-ray sensitivity, as reported in Ref. 8. **Figure 2.11** shows the results from a set of calculations using hypothetical 0.1-cm tube walls made of Be, Al, SS, and Pb. Below 100 keV there are the expected large differences in cutoff energy; for Pb shielding, the difference between the SI coefficients that assume either escape or absorption of secondary photons (from scattering and fluorescence) is clearly apparent at energies just above the K edge. At MeV-range energies, however, the effect of different shielding materials is surprisingly small, especially for the full CH_2-shielded assemblies shown in **Figure 2.12** and in more detail in **Figure 2.13**. This lack of effect disagrees with the experimental results in Ref. 8, perhaps because the data were derived from pileup measurements for a gamma-ray source with a maximum energy of 1.5 MeV, which would be more sensitive to the very large differences at lower energies. Furthermore, the analysis in Ref. 8 focuses on the count rate of events above a minimum pulse-height threshold, whereas our analysis is based on total energy deposition, that is, an energy-weighted integral over the full pulse-height spectrum.

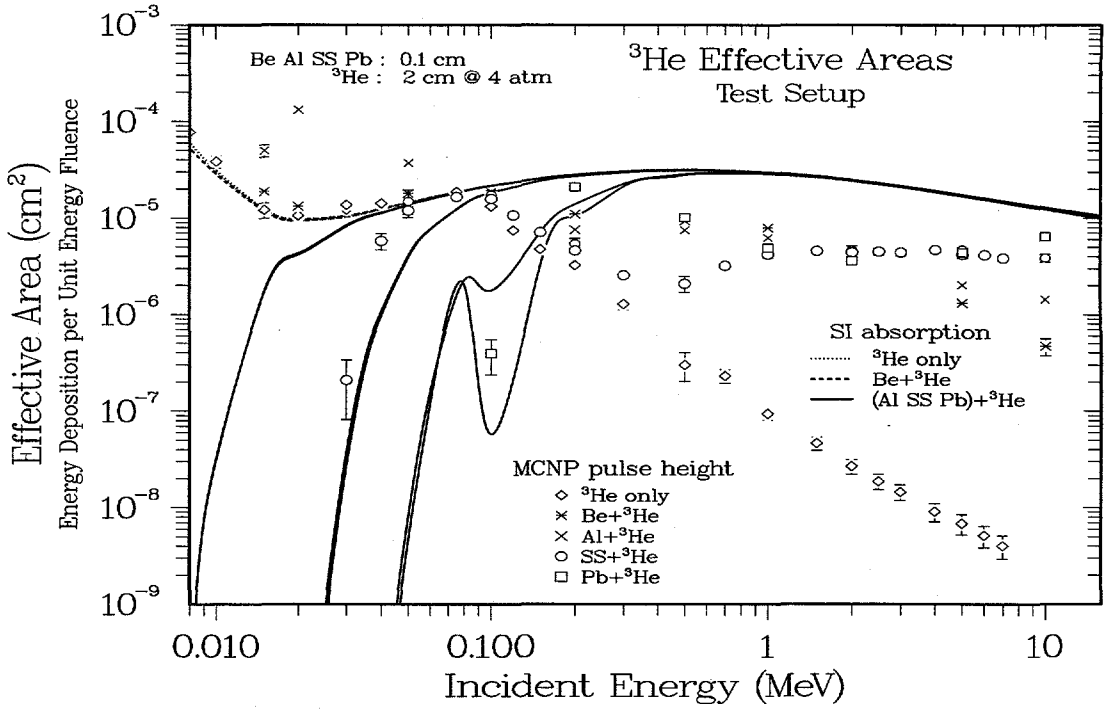

Figure 2.11. Effect of variations in tube wall materials (Be, Al, SS, or Pb) on the effective area of bare ^{3}He detector.

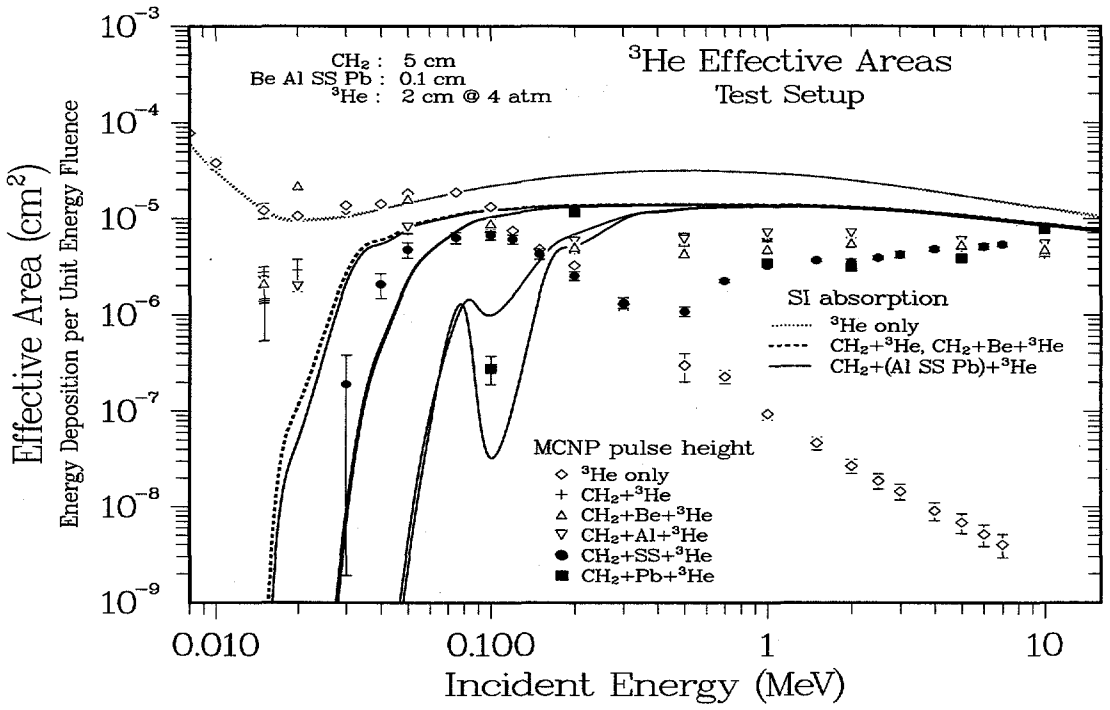

Figure 2.12. Effect of changes in tube wall materials on effective areas as in Figure 2.11, but for a ^{3}He detector with polyethylene moderation.

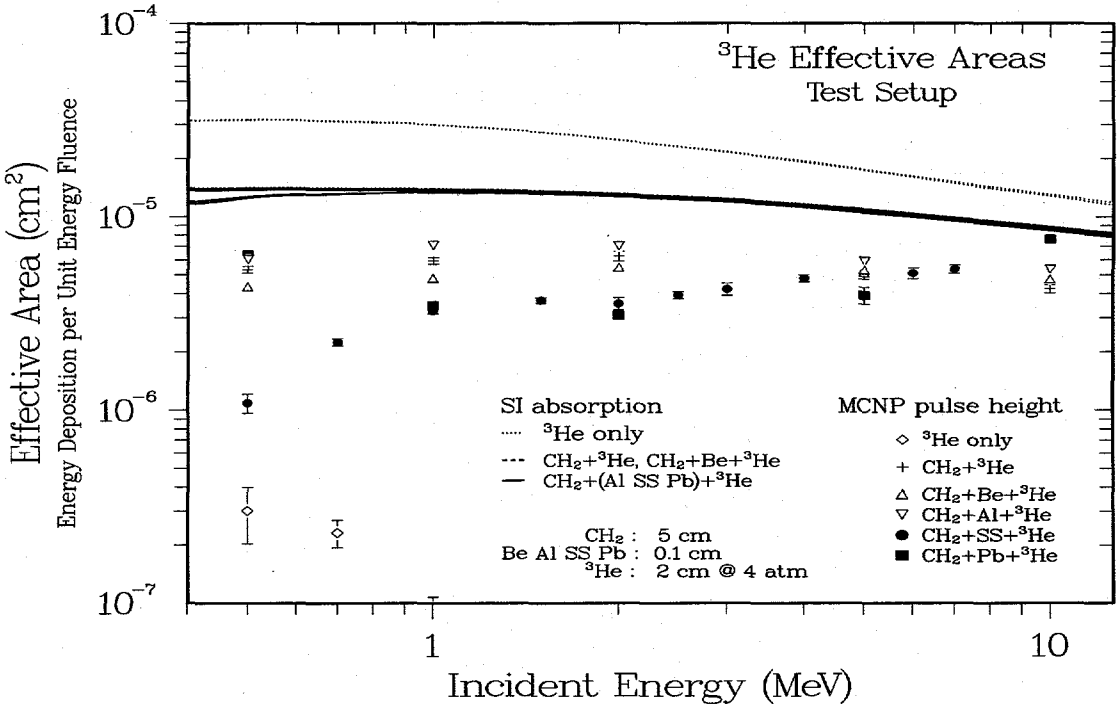

Figure 2.13. Detail of Figure 2.12, showing the lack of effect of changes in wall material over the energy range from 0.5 to 10 MeV.

2.3. Scintillator Responses

Gamma-Ray Interactions in Plastic Scintillators. A thorough discussion of calculations of the response of shielded plastic scintillators to MeV-range gamma rays is contained in Ref. 12. Included are comparisons between measurements and calculations using several different simulation codes, including MCNP. Unfortunately, the MCNP calculations did not include electron transport and therefore must be repeated; for the present work they are comparable to using an F6 heating tally. Nevertheless, the agreement between the measurements and the different calculations was uniformly excellent, which suggests that electron transport is not important if the scintillator dimensions are large compared with the electron ranges, which at 0.5–5 MeV are about 0.2–2 cm. The effective areas from the SI and MCNP heating calculations for different arrangements of the test setup are shown in **Figure 2.14**. The results for the bare BC400 scintillator are in almost exact agreement, but multiple-scattering effects lead to small differences for the other configurations, particularly for the different SI assumptions about the escape of secondary photons at the Ta *K* edge near 70 keV. Also note that the heating calculations are generally consistent with the spectral integrals obtained from the MCNP F8 pulse-height tallies, which is a very different result from the corresponding ^{3}He case in Figure 2.2. The calculated pulse-height spectra at 10 keV, 100 keV, and 1 MeV are shown in **Figure 2.15**, **Figure 2.16**, and **Figure 2.17**, respectively. The results are qualitatively similar to those for the ^{3}He setup in Figure 2.3, Figure 2.4, and Figure 2.5. At the lowest gamma-ray energies there are again photoelectric and Compton contributions, although the larger dimensions lead to more multiple scattering, as indicated by the counts that appear above the Compton energy. The spectrum for 100 keV is taken just above the Ta *K* edge, which explains the very low effective area and the small photopeak (see Figure 2.14). At 1 MeV the spectrum is almost entirely from Compton scattering, and the greater photon en-

ergy and longer attenuation length lead to much more multiple scattering, which would be a significant contribution to the pulse-height resolution observed experimentally. When compared with other calculations made without electron transport, some of the counts are moved from high to low energy depositions because of electron escape. Thus, the area of the spectrum is almost unchanged, but the energy-weighted integral and hence the effective area is decreased slightly. The effective areas calculated including electron transport (*F8 tallies) are shown in **Figure 2.18** and in detail in **Figure 2.19**. There appears to be no significant change in shape from the heating results, although the pulse-height areas at energies above 1 MeV are consistently lower.

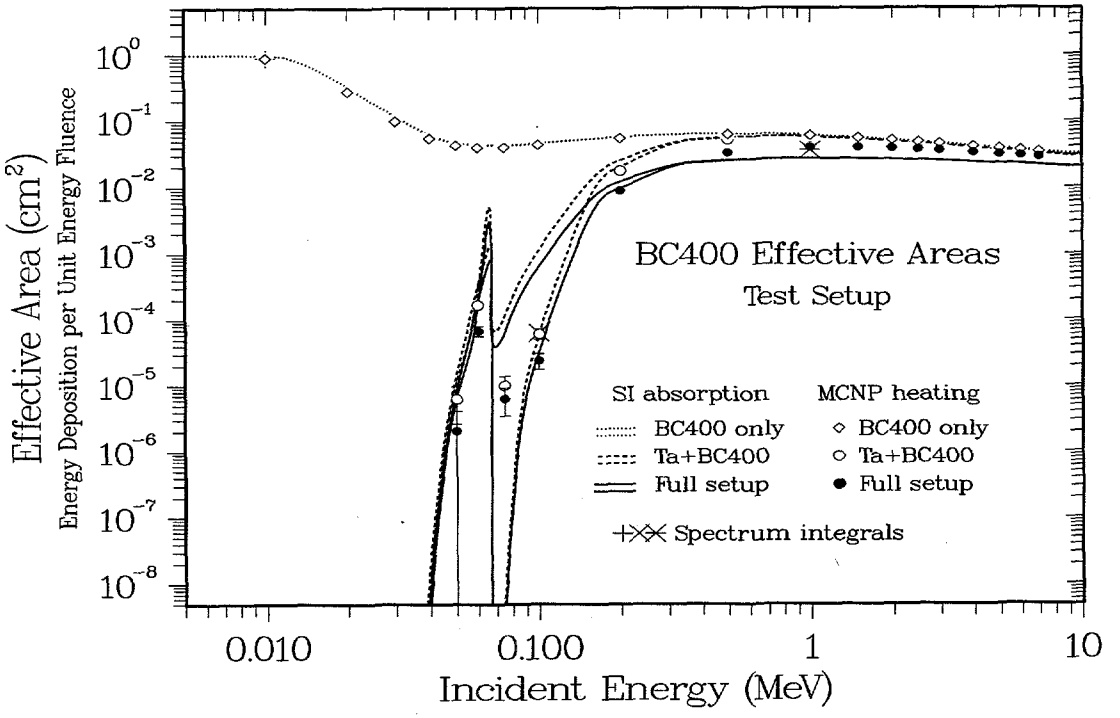

Figure 2.14. Effective areas obtained from heating calculations as in Figure 2.2, but for an SPG-like arrangement of polyethylene, Ta, and BC400 scintillator materials.

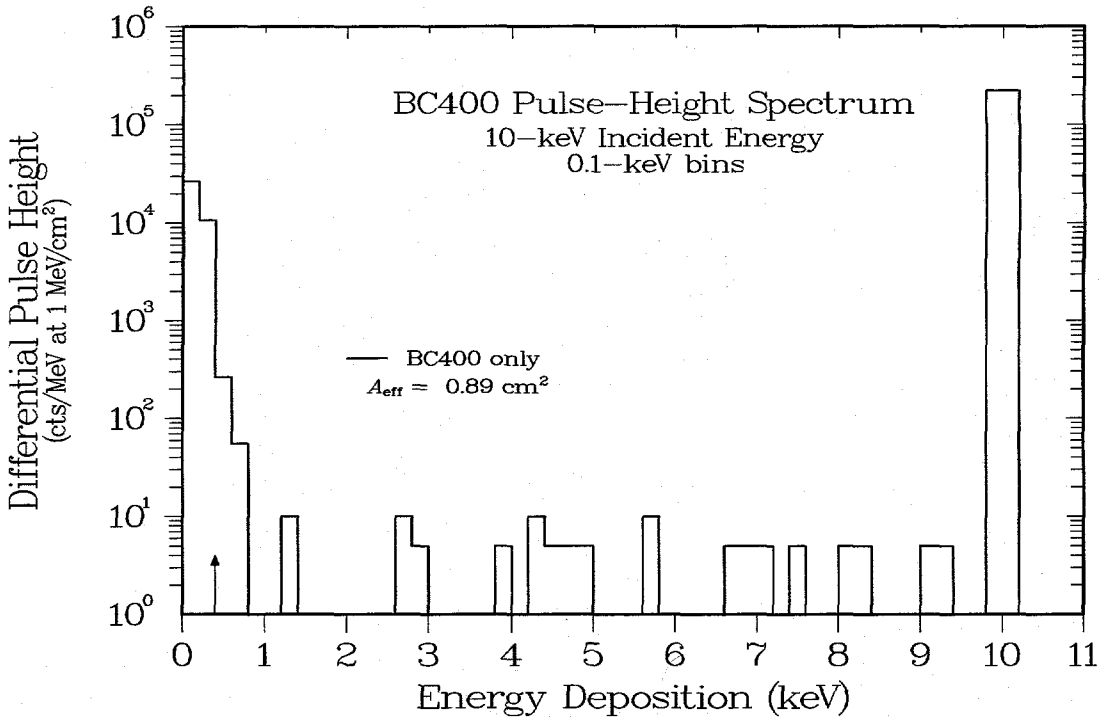

Figure 2.15. Calculated pulse-height spectrum produced by 10-keV gamma rays incident on the unshielded BC400 scintillator arranged as in Figure 2.1.

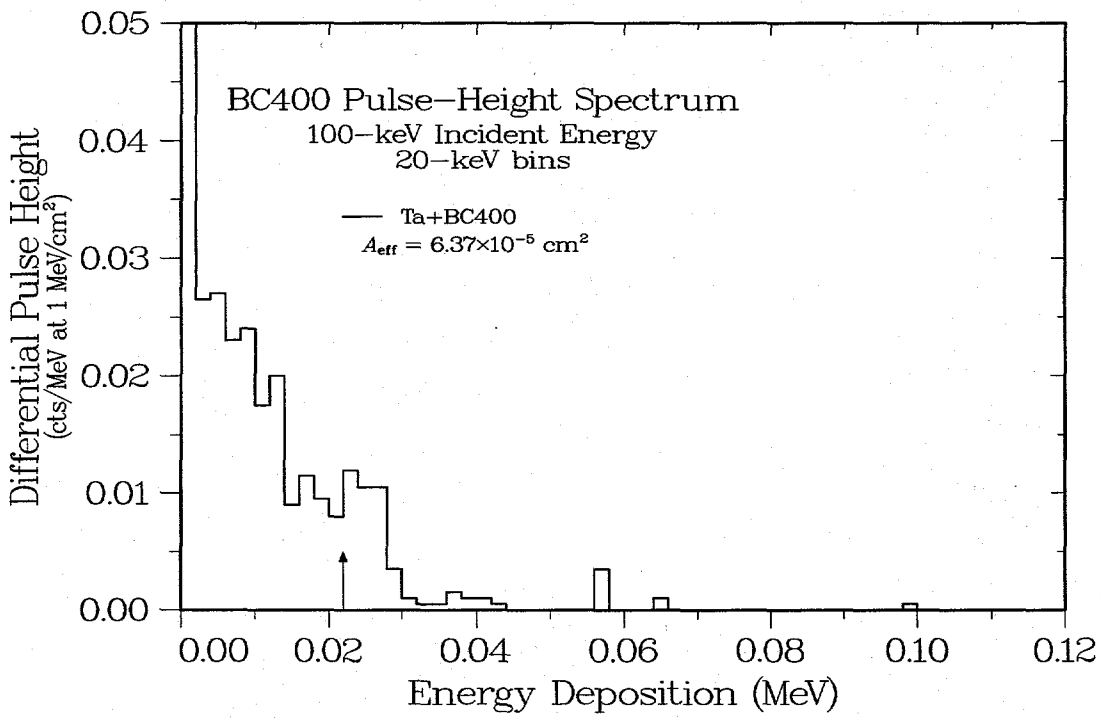

Figure 2.16. As in Figure 2.15, calculated pulse-height spectrum produced by 100-keV gamma rays incident on a Ta-shielded BC400 scintillator arranged as in Figure 2.1.

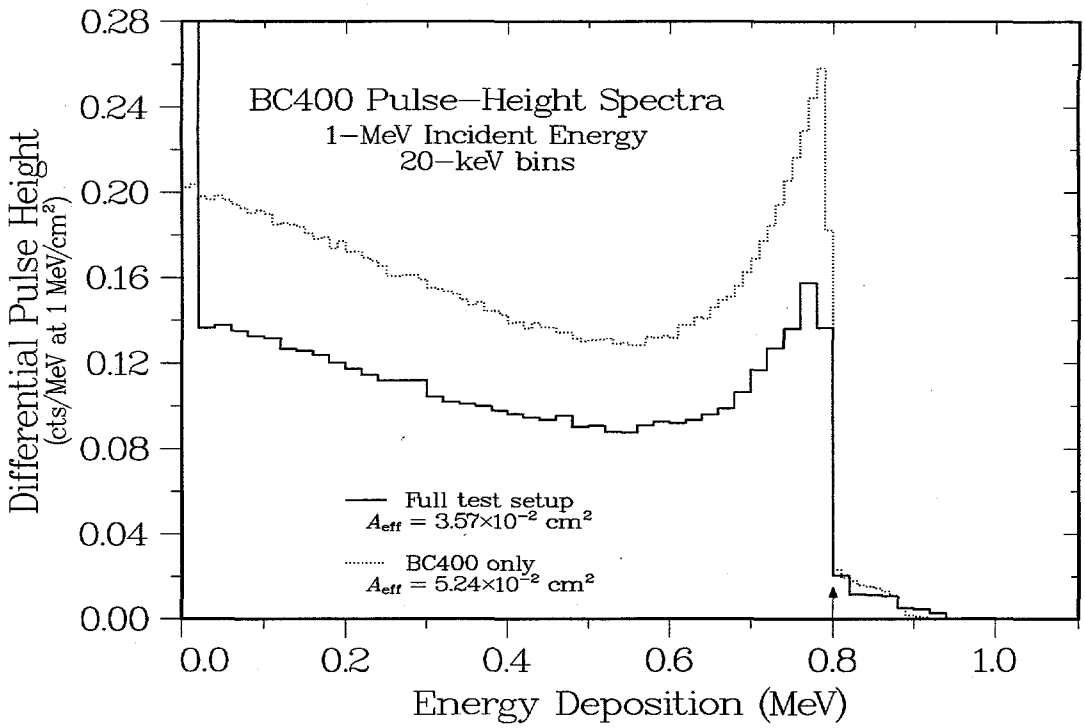

Figure 2.17. Pulse-height spectra as in Figure 2.16, but for 1-MeV gamma rays incident on either bare or fully shielded BC400 scintillators.

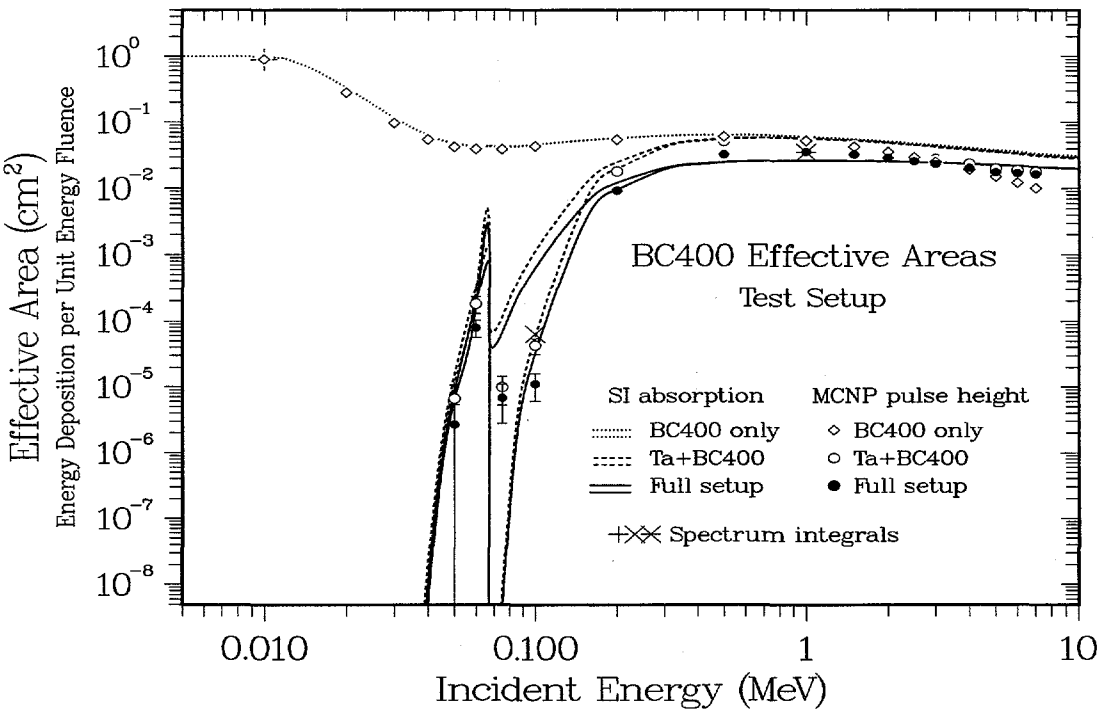

Figure 2.18. Complete effective-area energy functions for shielded and unshielded BC400 scintillators. (For comparison, see the corresponding heating results in Figure 2.14.)

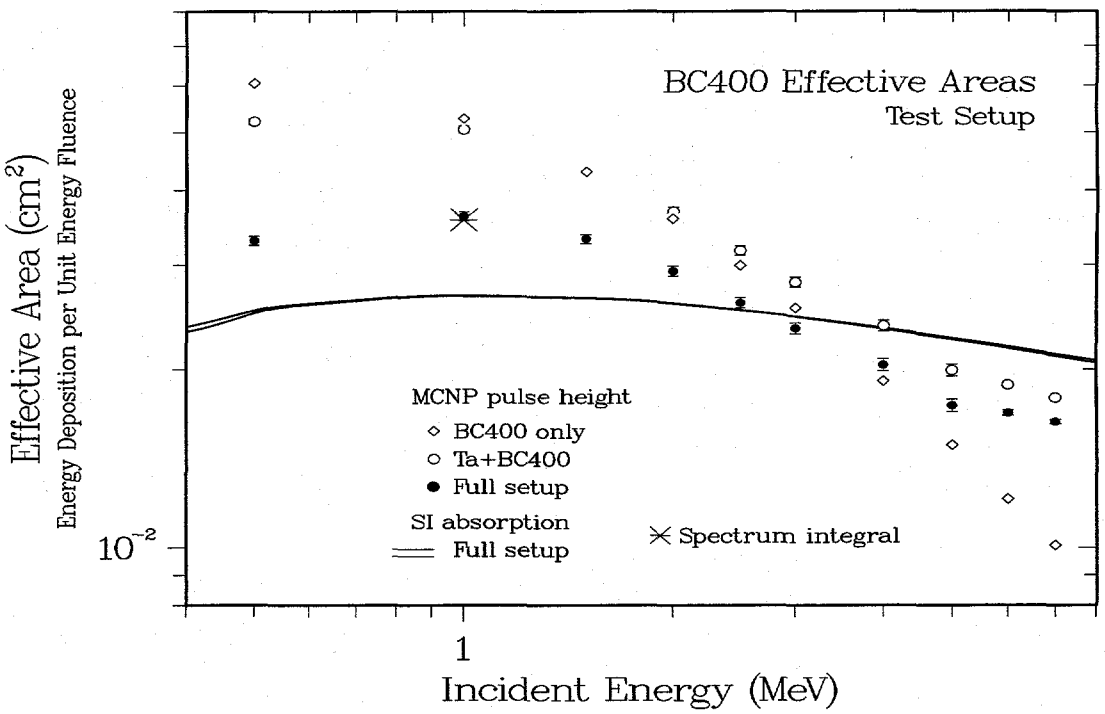

Figure 2.19. Enlarged detail of the energy dependence of the effective-area functions shown in Figure 2.18.

2.4. Discussion

Results. The test-setup calculations and discussions in this chapter have led to three important conclusions:

(1) There is generally good agreement between the SI absorptions and MCNP heating tallies unless the layer thicknesses are large enough that multiple scattering becomes an issue. This result reinforces the concept that heating tallies are similar to MCNP detector tallies, where the particles are transported between interaction sites assuming macroscopic attenuation factors. Thus, SI absorptions and heating tallies, while useful for reference and quick to calculate, are accurate only if the problem dimensions are large compared with the electron range.

(2) Conversely, electron-transport effects can be large whenever the problem dimensions are smaller or comparable to the electron ranges, as seen especially for the ^{3}He studies in Sec. 2.2.

(3) A surprising result is the degree of agreement between the simple SI effective areas for the shielded setups and those calculated with electron transport, even though the energy-loss mechanism may be completely wrong. A partial explanation is suggested by the shielding calculations for Figure 2.11, where the increase in electron production in higher-Z materials is apparently cancelled by the decrease in electron range, at least in our energy range. For thin detectors, most of the electrons produced within the detector escape without depositing much of their energy, but this loss is largely compensated by other electrons produced in the surrounding shielding.

Literature. Given the importance of electron transport in calculating the response of detectors to incident gamma rays, it might be expected that this issue would be prominent in published reports. Unfortunately, many of the relevant papers predate the development of the

simulations needed to unravel such complex phenomena, whereas more recent papers often focus not on detectors but on health-physics dosimetry, which is difficult to relate to the current application. For example, a notably prescient early article[13] observed that "a plastic scintillator or GM tube with a thick low-Z wall has a γ-ray efficiency that increases linearly with γ-ray energy." Here, efficiency refers to creating electrons in the detector wall and then counting them in the active element. For comparison, our effective areas are calculated as energy-weighted pulse-height integrals that are divided by the incident energy fluence. Thus, a counting efficiency that increases linearly with energy is equivalent to an effective area that is constant with increasing energy, so the two observations are consistent. Ironically, the above reference was only peripherally concerned with detection efficiency; the primary focus was measurements of neutron-capture cross sections, which involve gamma-ray energies similar to those in the present application. As another example, a more recent medical physics article[14] addresses the problem of determining the gamma-ray dose produced by secondary electrons in multilayer tissue. The abstract states in part:

> The results presented show that the complex physical mechanisms governing Co-60 interface dosimetry still make Monte Carlo condensed-history (macroscopic) techniques uncertain. It has been found that the EGS4 Monte Carlo system ... yields good agreement with experiments... .

These conclusions are echoed in our own work.

3. RELATED INSTRUMENTS

Motivation. The test calculations in Chap. 2 provide a wealth of insight into the mechanism for the SAN and SPG detectors' gamma-ray responses, but there are no comparable measurements because no prototype instruments have as yet been built. The closest parallel is the existing APG detector in the ARII instrument suite, which like the SPG has a plastic scintillator that is viewed by a high-sensitivity photomultiplier and a low-sensitivity photodiode. Because of very poor light collection, however, the APG scintillator channel is difficult to treat analytically, and the silicon photodiode actually has a larger response to the incident gamma rays directly than to the optical signal from the scintillator.[15] The latter situation may also exist for the XDS detector, which uses a Si photodiode to view the light output from a CsI scintillator. These issues are very similar to that encountered in Sec. 2.2 for ^{3}He ionization chambers, where the response from the gas itself is negligible compared with that from the chamber walls. To avoid this problem, the SPG design uses a gamma-ray-insensitive vacuum photodiode instead of a Si photodiode. Unfortunately, however, Si photodiodes are widely used in other satellite instruments. The calculations in this chapter therefore have a threefold purpose:

(1) to determine whether the observed APG diode response arises mainly from secondary electrons, thereby confirming the present ^{3}He predictions;
(2) to determine whether such direct response is likely in other cases; and
(3) to determine whether changes in shielding can reduce the direct response.

In addition, we will open with a literature review of articles on Si diode response.

Si Diode Literature. Because the use of Si diodes for radiation dosimetry is a relatively recent development, a number of useful references are available. In some cases, particularly those that emphasize low energies, the unlikely assumption is made that SI coefficients can be used to calculate detector responses at energies as high as 10 MeV.[16] In other cases the importance of contributions from the surrounding shielding is recognized experimentally, but these contributions are identified as fluorescence photons, not electrons, even at gamma-ray energies above 1 MeV.[17] In contrast, other authors have shown a good understanding of the central role of secondary electrons. One article[18] states:

> A 300-μ detector is virtually transparent to gamma rays and opaque to electrons. ... [When shielding is added,] the detector sensitivity using this geometry results from electron production from gamma-ray interactions in the absorber and detector.

The included measurements show that the shielded detector's counting rate increases by 43% as the gamma-ray energy increases from 662 to 1250 keV. More recently, portable dosimeters have been developed that cover a Si diode with "radiator" materials—air, polyethylene, or aluminum—specifically intended to convert incident gamma rays to electrons.[19] By further covering the low-Z radiator with a layer of higher-Z shielding, the dosimeter's energy response can be modified to exclude the effect of low-energy photons.[20] Finally, the most recent references describe the use of inexpensive Si photodiodes as dosimeters rather than optical transducers. One article[10] proposes an approximate method for correcting the response for the contribution of electrons produced in adjacent "buffer" materials and includes spectral measurements that are very similar to the ^{3}He calculations presented in Chap. 2. A second article[21] includes both measurements and calculations of count rates and pulse-height spectra

for both bare and shielded diodes as functions of gamma-ray energy. Significantly, the count rates are independent of shielding material from 200 keV to 2 MeV, just as suggested by our calculations below and in Sec. 2.2. In short, the literature for Si-diode gamma-ray detectors is much more instructive than that for ^{3}He counters, and the consensus is entirely consistent with our view that the principal response mechanism for thin detectors at MeV-range energies is the production of secondary electrons in the surrounding converter materials.

3.1. APG Diode Response

APG Diode with Cu Housing. Our discussion of the gamma-ray response of the Si photodiode in the APG detector is patterned on the corresponding ^{3}He and BC400 discussions in Chap. 2. **Figure 3.1** begins with the SI absorptions and MCNP heating tallies as in Figure 2.2, but now for a slab-geometry setup consisting of a bare 300-μm Si diode and the diode covered with three successive layers: the thin (0.02 cm) Cu diode housing, the high-*Z* Ta shielding (0.051 cm), and the outer Al instrument housing (0.3175 cm). The photoelectric cutoff at low energies behaves just as expected, but the convergence of all the absorption and heating values to essentially the same high-energy values is unexpected. Again, the individual plotting symbols at 10 keV and 1 MeV show the energy-weighted spectrum integrals. **Figure 3.2** and **Figure 3.3** repeat the SI absorptions for reference, but now the MCNP tallies are *F8 pulse-height tallies. The response of the bare diode is greatly reduced at high energies, but each additional layer of shielding material brings the detector's effective energy-absorbing area closer to the original attenuation estimates.

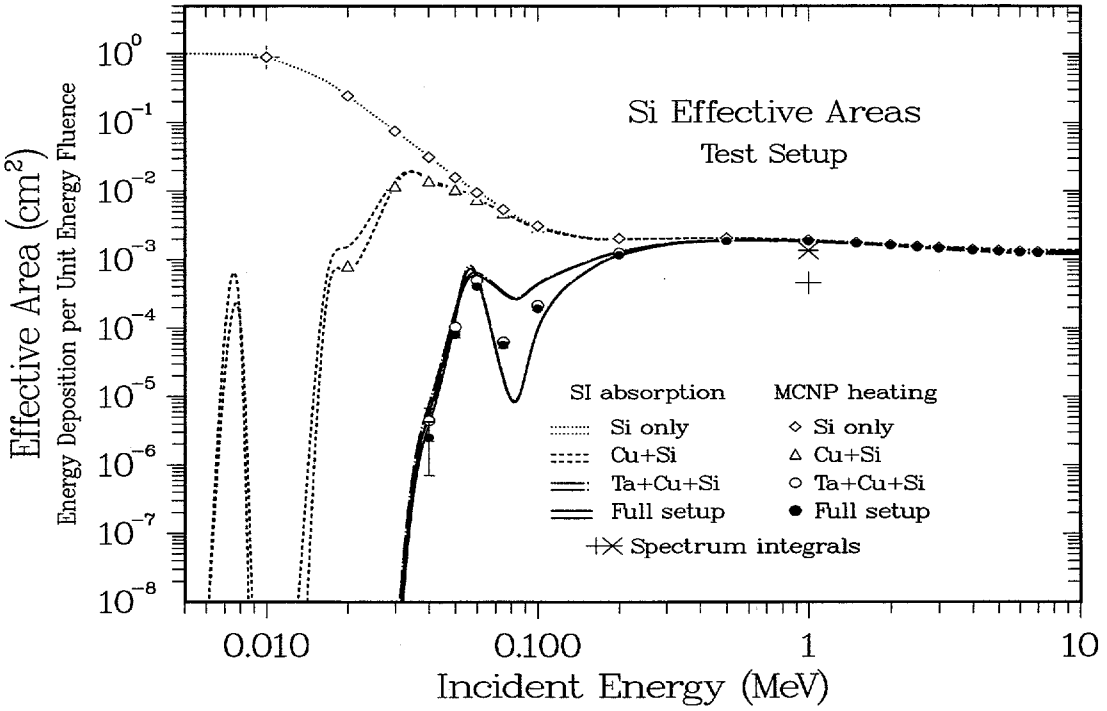

Figure 3.1. MCNP heating tallies and SI absorptions for a test version of the APG diode channel.

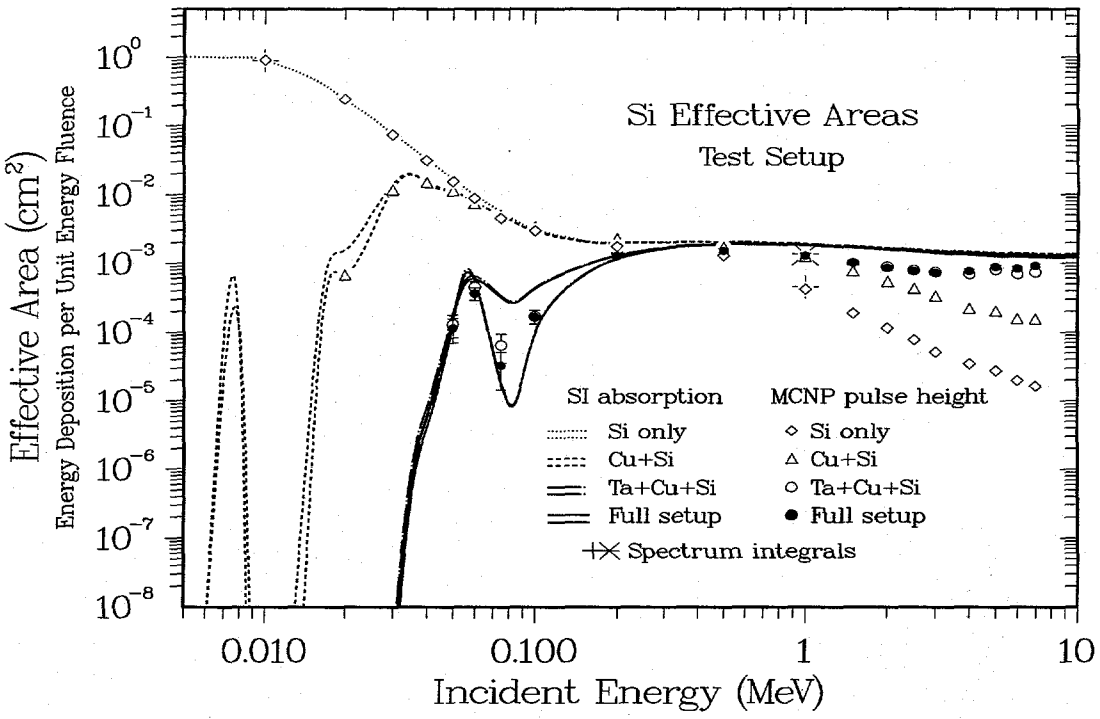

Figure 3.2. Energy-dependent effective areas for a simplified version of the shielded Si-diode detector used in the current APG detector.

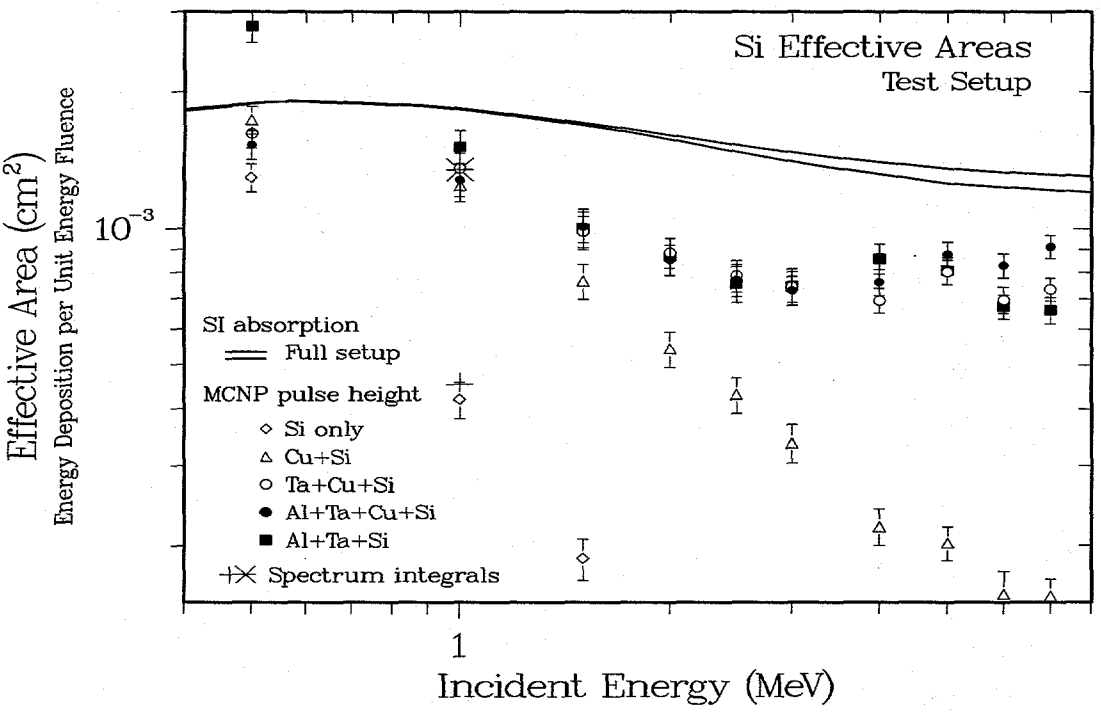

Figure 3.3. Detail of the effective-area functions shown in Figure 3.2.

Differential Energy-Loss Spectra. The 1-MeV pulse-height tallies for the bare and shielded diodes are shown in **Figure 3.4**, and the electron fluences entering the diode from the front (Ta) and rear (BC400) sides are shown in **Figure 3.5**. The relatively featureless energy-

loss spectrum for the bare diode is consistent with electrons that are created at a variety of depths and then escape without depositing their full energy. In contrast, the added counts for the electrons produced in the diode's surroundings appear as expected at about 0.2 MeV; the long high-energy tail is probably associated with divergence of the secondary-electron fluence. The calculated spectrum is very similar to the measured one for 1.25-MeV ^{60}Co gamma rays in Ref. 17, which attributed the low-energy peak not to electrons but to 80-keV fluorescence x-rays produced in the Pb shielding around the diode. For the calculated electron spectra in Figure 3.4, there is a clear difference between the forward-scattered component from the shielding versus the backscattered one from the BC400 scintillator. As expected, combining the electron fluences in Figure 3.5 with Si energy-loss tables allows us to reproduce the pulse-height spectra in Figure 3.4.

Discussion. Our first goal in this section has been to verify that the large diode response observed with the existing APG instrument is consistent with our model of secondary-electron production and energy loss in thin detectors. The calculations for the bare and shielded diodes support this view, as do the observations from several references in the literature search. Further, the effective areas in Figure 3.3 indicate that (1) the diode response does not depend strongly on either energy or shielding material, and (2) the response is almost the same as that obtained from SI absorptions and adopted in Ref. 12. Again, we conclude that in this energy range such coefficients can often provide answers that are approximately correct despite their overly simplistic interaction assumptions.

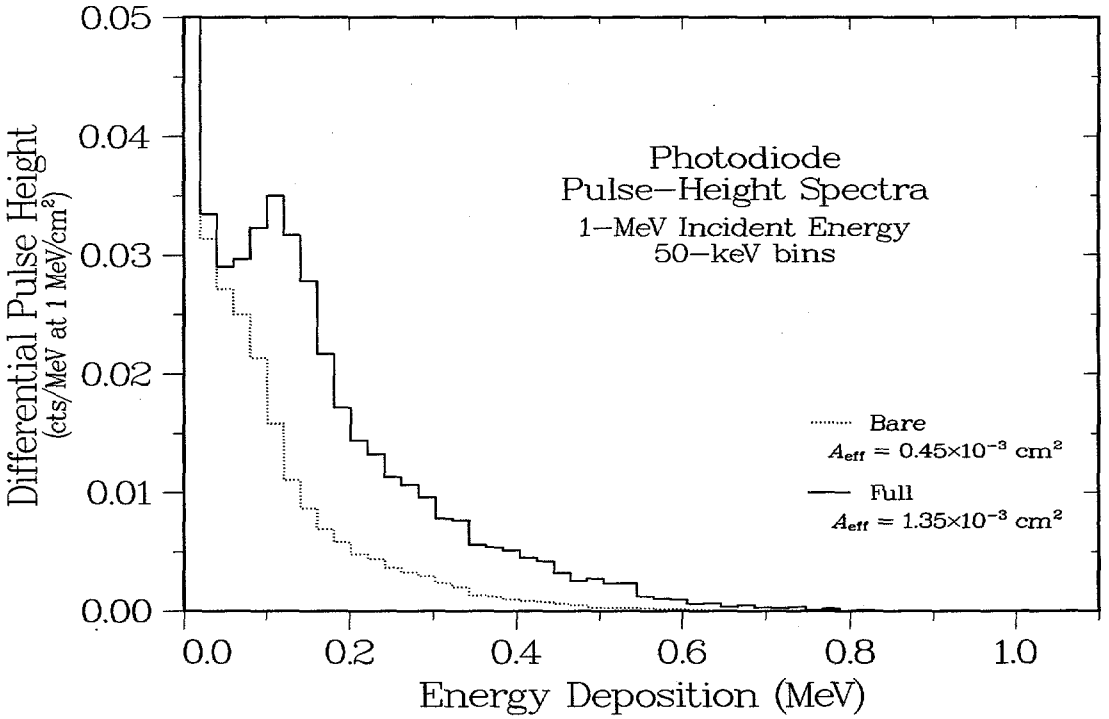

Figure 3.4. Bare and shielded diode pulse-height spectra produced by 1-MeV gamma rays.

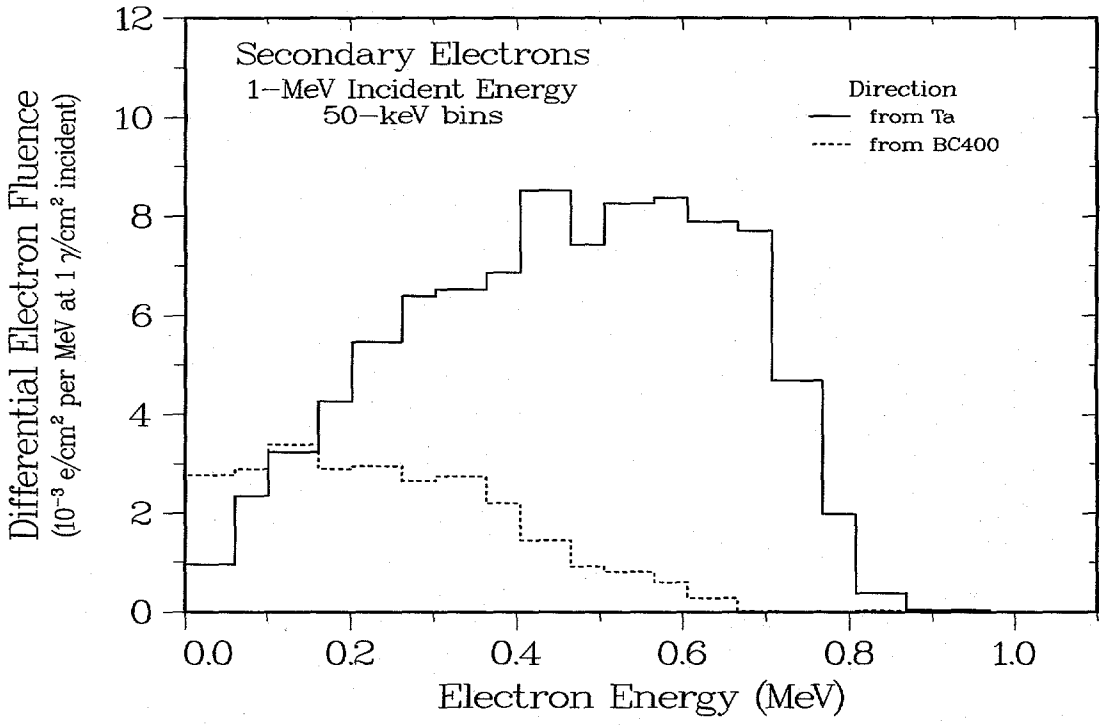

Figure 3.5. Fluence spectra of the electrons entering the Si diode from either the front (Ta) or back (BC400). The resulting pulse-height spectrum is shown in Figure 3.4.

3.2. XDS Diode and Scintillator Responses

Parameters and Results. Another example of an Si diode occurs in the ARII XDS detector, which also uses a Si photodiode, in this case to read out a CsI scintillator that is shielded by layers of Ag and Al. Instead of constructing a slab geometry as in Figure 2.1, we used a uniform angular distribution to illuminate the detector uniformly from all directions. The MCNP pulse-height results for the bare diode are shown in **Figure 3.6** for comparison with SI absorption values, which use plane-wave incidence as in the slab geometry. The discrepancy in projected area at the lowest energies comes from averaging the uniform illumination over all angles; the departure above 200 keV is the familiar result of electron escape from the diode. The electron fluences entering the diode from the Ag and CsI directions are shown in **Figure 3.7**. For uniform illumination there is no longer a forward or backward direction, so there is little difference in magnitude for the electron fluences from both directions. **Figure 3.8** shows the resulting diode pulse heights; the addition of shielding approximately doubles the number of counts in the pulse-height spectrum, thereby doubling the diode's effective area.

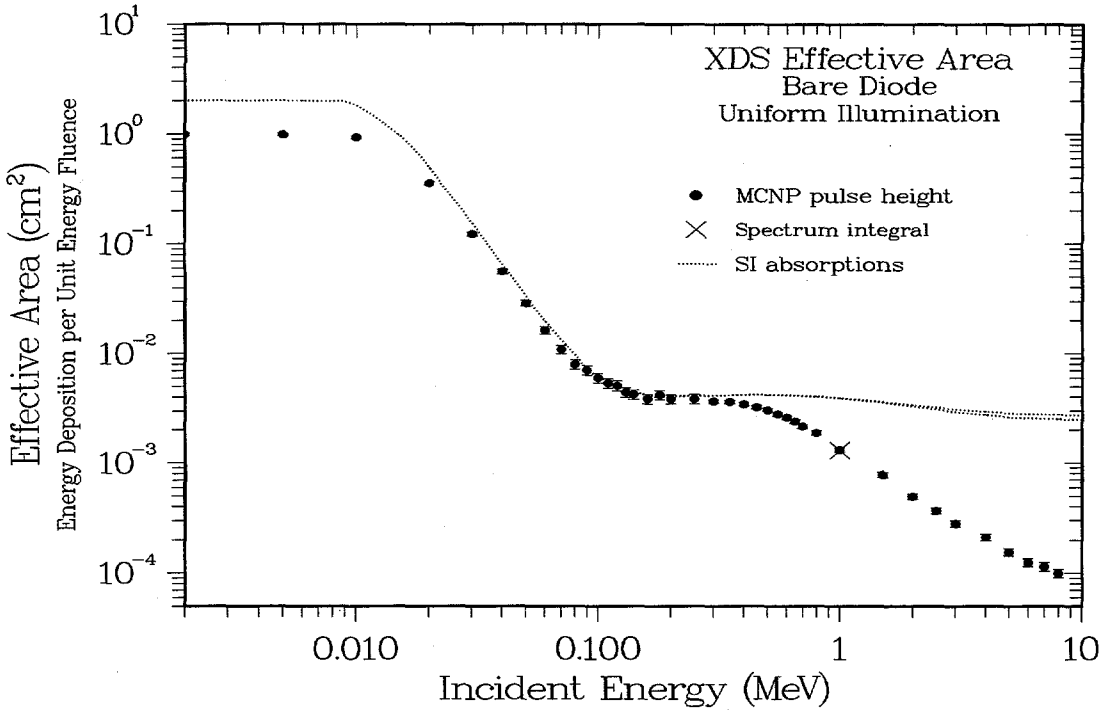

Figure 3.6. Heating vs. pulse-height effective areas for a bare Si photodiode uniformly illuminated from all incident directions. Note the onset of electron "punch-through" for gamma-ray energies above about 200 keV.

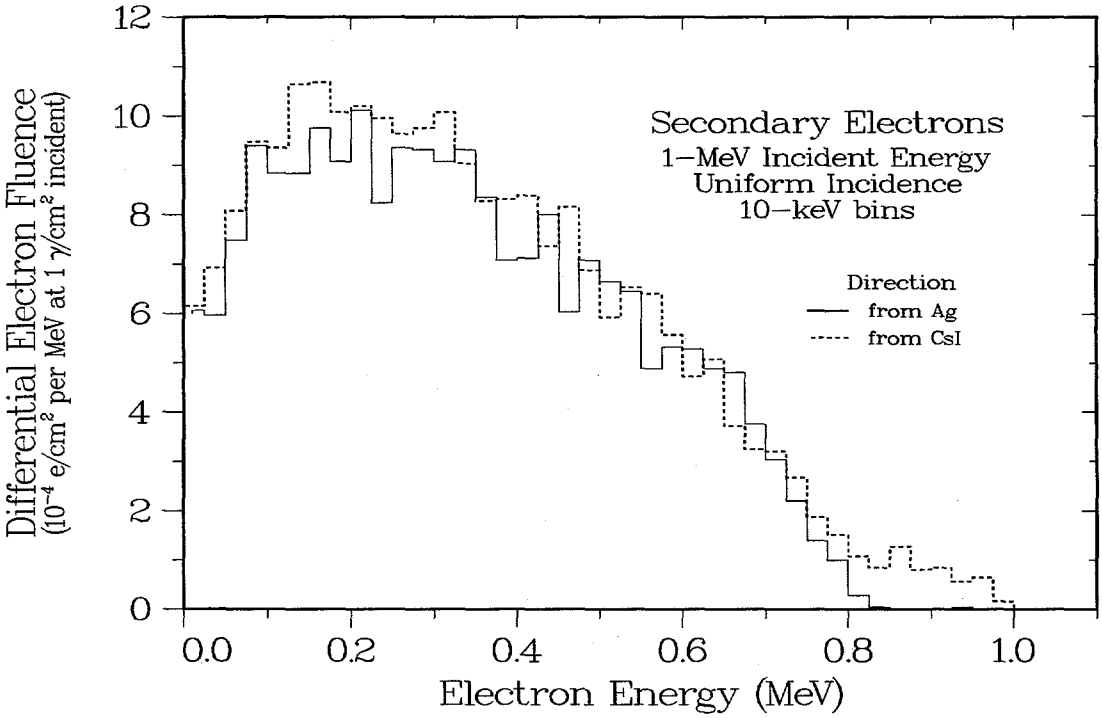

Figure 3.7. Electron fluences produced by uniform illumination of a Si diode used to view an Ag-shielded CsI scintillator.

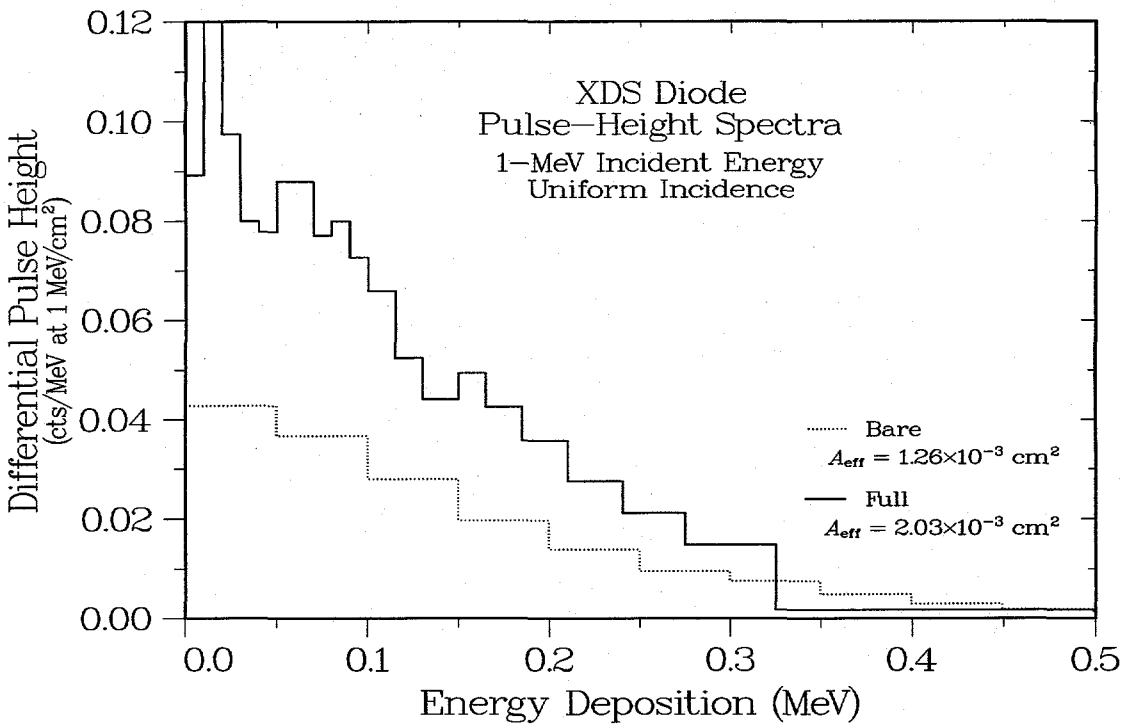

Figure 3.8. Diode pulse heights resulting from the electron fluences in Figure 3.7.

Energy Dependence. As with the APG detector, the XDS photodiode was intended to respond to gamma-ray interactions that create optical photons in a scintillation detector, not to be a direct detector of incident radiation itself. For the very poor light collection of the APG detector, measurements have shown that the direct radiation response is in fact about an order of magnitude greater than the optical signal.[12] As yet, no similar measurements have been made for the XDS detector; its use of air coupling between the CsI scintillator and the photodiode is similar to the APG design, but the CsI scintillation efficiency and the XDS light-collection efficiency may be large enough to compensate for the air-gap losses. As a first step in the evaluation, in **Figure 3.9** we show the calculated effective areas for the fully shielded CsI scintillator and the Si photodiode. Bare and shielded SI absorptions are also shown for comparison. For the SI absorptions, the thicknesses of the Ag and Al shielding were increased by a factor of 4.5 to match the low-energy cutoffs; the change has no effect on the response at higher energies. This adjustment was presumably needed to compensate for differences between the uniform and parallel illumination.

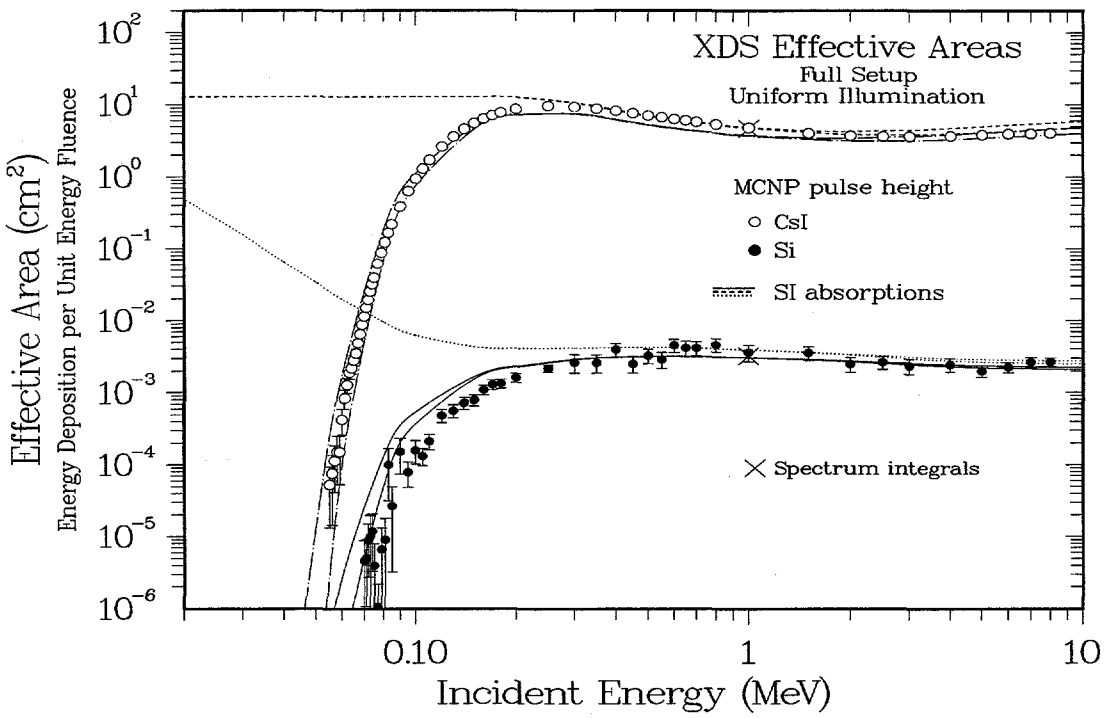

Figure 3.9. Energy dependence of the effective areas of a shielded Si photodiode and CsI scintillator uniformly illuminated by incident gamma rays.

Discussion. The effective-area calculations in Figure 3.9 lead to several important observations:

(1) Because the surrounding shielding is the same, the cutoff energies for both the CsI and Si responses are the same. This cutoff also matches that for the APG detector,[12] to which XDS is functionally related.

(2) The broad plateau value of the CsI effective area is within a factor of 2 of the APG value, which gives the two instruments similar sensitivities. When combined with the similarity in cutoff energies, this result indicates that the XDS and APG detectors have essentially the same operational response to incident gamma rays.

(3) There is a difference of almost 3 orders of magnitude between the CsI and Si effective areas. If the total optical efficiency (energy conversion, light collection, and quantum efficiency) of the CsI scintillator is at least 1% of the direct efficiency for the Si diode, a reasonable assumption, then the expected optical response should dominate by at least a factor of 10.

(4) The MCNP results for both the CsI and Si detectors are in almost perfect agreement with their SI absorption counterparts, which were originally used for the instrument design. This agreement for the shielded diode holds despite the clear disagreement in Figure 3.6 between the MCNP pulse heights and the SI absorptions for the bare diode.

The excellent agreement between the SI and MCNP results for the shielded diode, where the electron range is clearly much larger than the 300-μm Si thickness, illustrates the difficulty of predicting the contributions from secondary electrons. Our study of this issue continues in the following section.

3.3. Shielding Variations

Objective. The excellent agreement in Figure 3.9 between the Si absorptions and the MCNP pulse-height tallies for the Al+Ag shielding on the XDS detector begs the question: How does the effect of secondary electrons on diode response depend on the surrounding shielding material? This section attempts to address this question using calculations that vary both the material (Z = 1, 11, 21, 31, 41, 51, 61, 71, 81, and 91) and the thickness (1 versus 10 g/cm^2) of the shielding. Because shielding is usually designed to provide a certain cutoff energy, the lower thickness is most appropriate for the higher Z values, while the higher thickness might be used for lower-Z shielding. In all cases the detector is the 300-μm Si photodiode used in both the APG and XDS instruments.

Si Heating Calculations. We first look at a comparison between the SI absorptions and the MCNP heating calculations. The results for the 1-g/cm^2 thickness are shown in **Figure 3.10**, and **Figure 3.11** shows the corresponding results for the 10-g/cm^2 shield. Not surprisingly, both attenuation approaches give the same cutoff energies and plateau levels for almost every shielding configuration, the only exception being the Z = 1 case. Remarkably, however, at both thicknesses the heating values are independent of Z at all energies above the cutoff value, again with the exception of Z = 1. These results are similar to those in Figure 3.1.

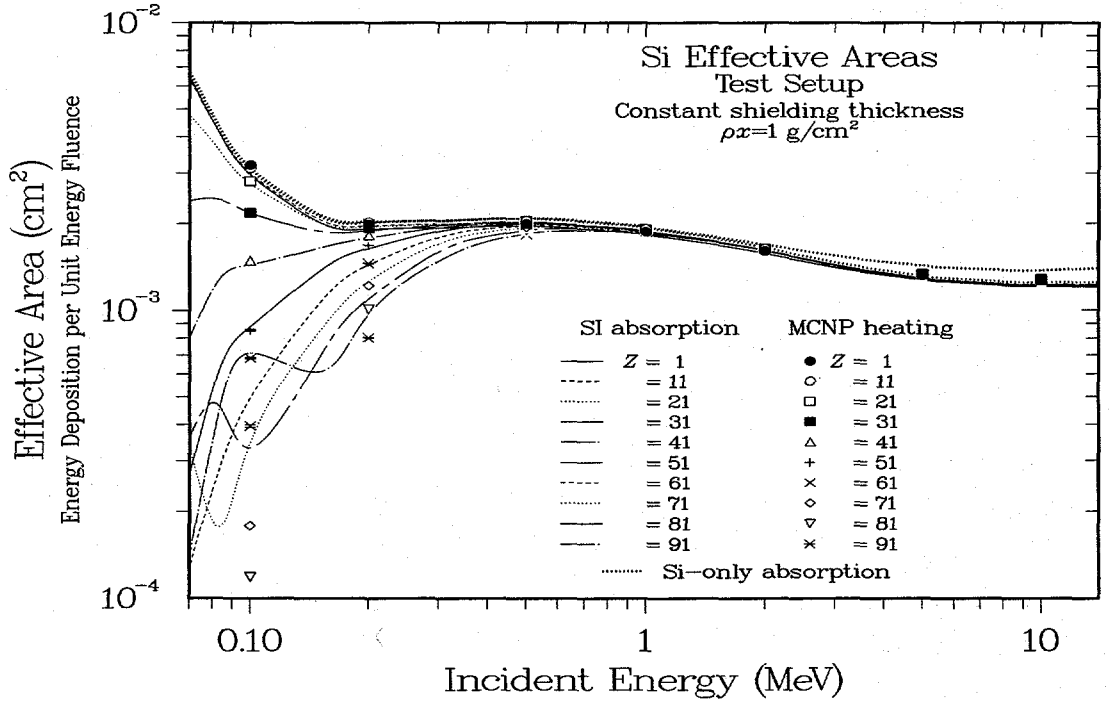

Figure 3.10. Heating calculations for a 300-μm diode shielded by 1-g/cm^2 thicknesses of materials with varying Z.

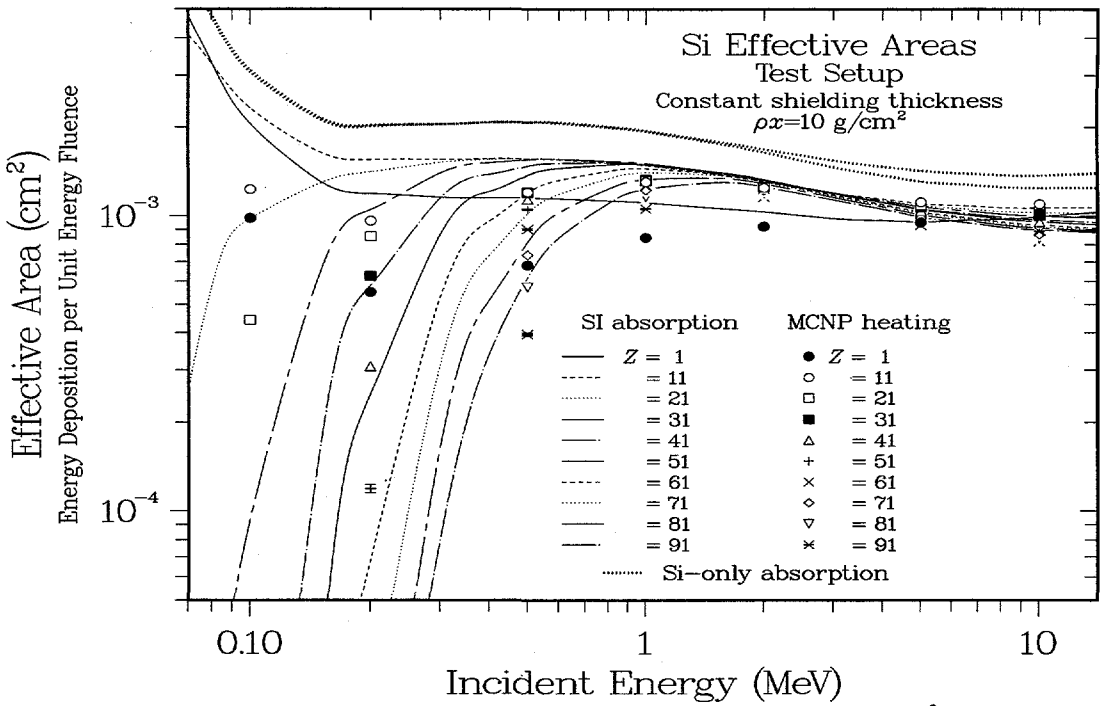

Figure 3.11. Heating calculations as in Figure 3.10, but for 10-g/cm^2 shielding thicknesses.

Si Pulse-Height Calculations. The more important issue is of course the behavior of the electron-transport results from the MCNP pulse-height tallies. These calculations for 1 g/cm^2 are shown in **Figure 3.12** (for high-Z shielding) and **Figure 3.13** (for low-Z shielding); the 10-g/cm^2 results are shown in **Figure 3.14**. In all cases, the conclusions almost mirror those of the heating calculations:

(1) For high-Z shielding at both thicknesses, changes in shielding material have almost no effect on the diode's effective area at energies above the cutoff value.

(2) For low-Z shielding ($Z < 20$), there are differences in the diode response, but the changes are still less than a factor of 2.

(3) Except for the case of thin, low-Z shielding, the diode's effective area is almost constant for energies above the cutoff.

These conclusions are entirely consistent with the few results available in the literature, the best example being the measurements and EGS4 calculations presented in Ref. 21. Finally, because our arbitrary choice of Z values does not represent the shielding on a practical detector, **Figure 3.15** shows additional calculations for the extreme low-Z and high-Z cases of Be and Pb shielding. For these cases we have adjusted the shielding thicknesses to provide cutoff energies near 100 keV. For Pb, the 0.05-cm thickness gives results similar to those for the high-Z, 1-g/cm^2 case in Figure 3.12. For Be, the 16-cm thickness is probably not practical, but the effective areas nevertheless agree at 1 MeV, although they diverge at both lower and higher energies.

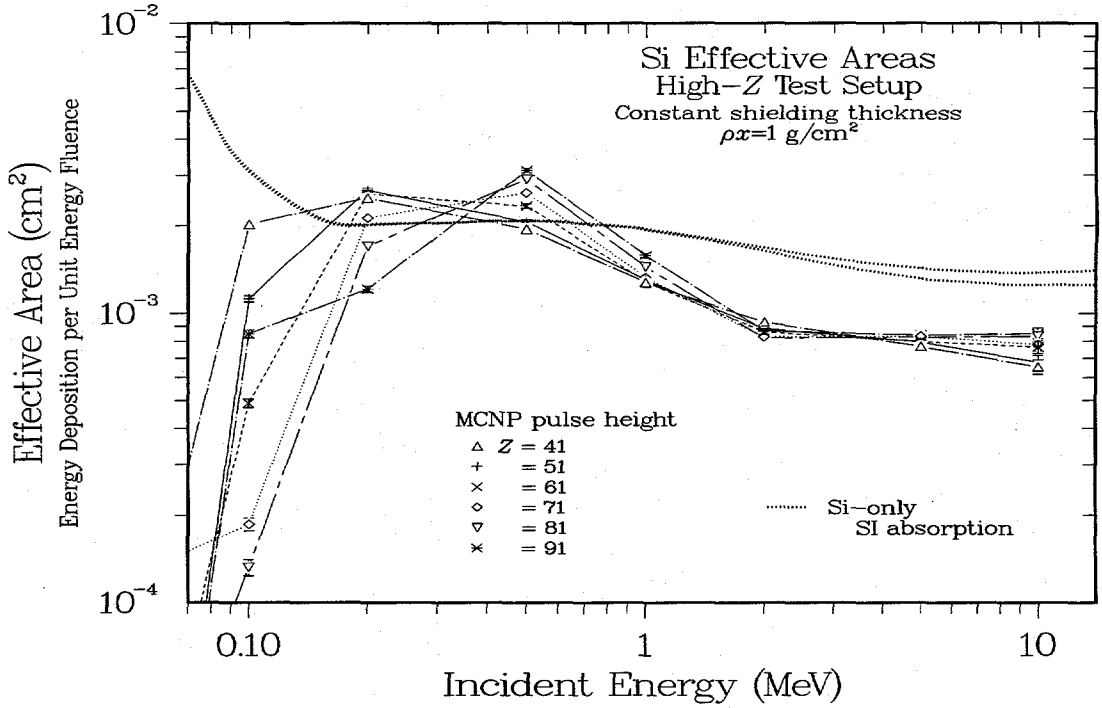

Figure 3.12. As in Figure 3.10, effective areas for different high-Z shields, but now using MCNP pulse-height instead of heating tallies.

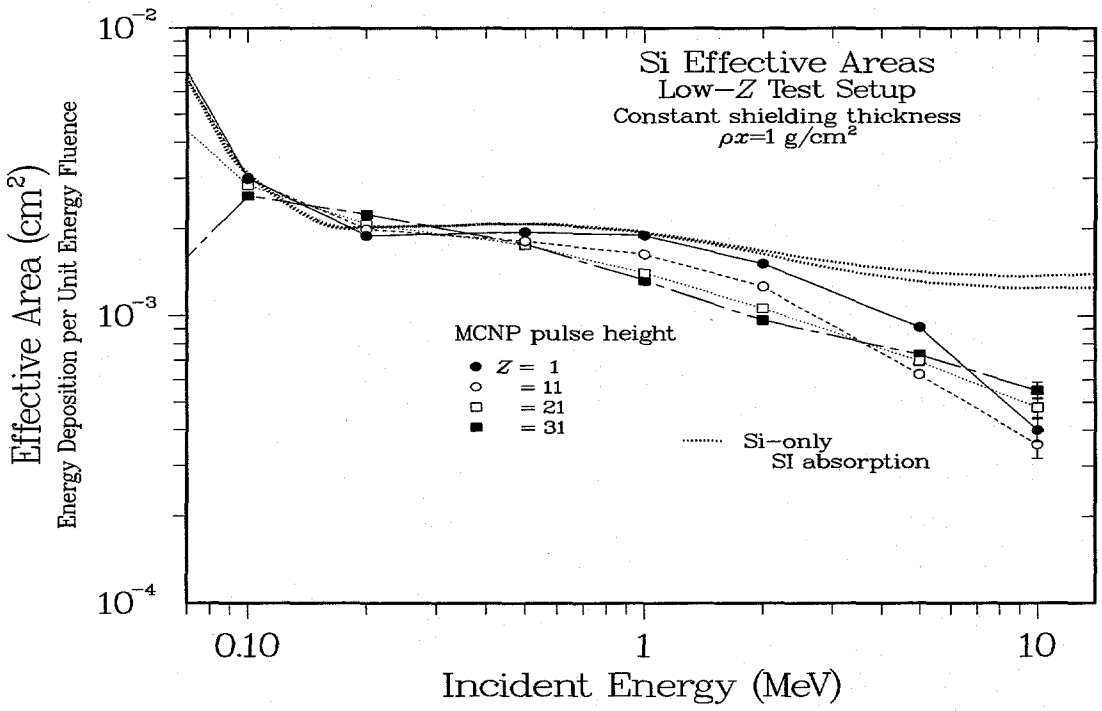

Figure 3.13. Pulse-height effective areas as in Figure 3.12, but for low-Z shielding materials.

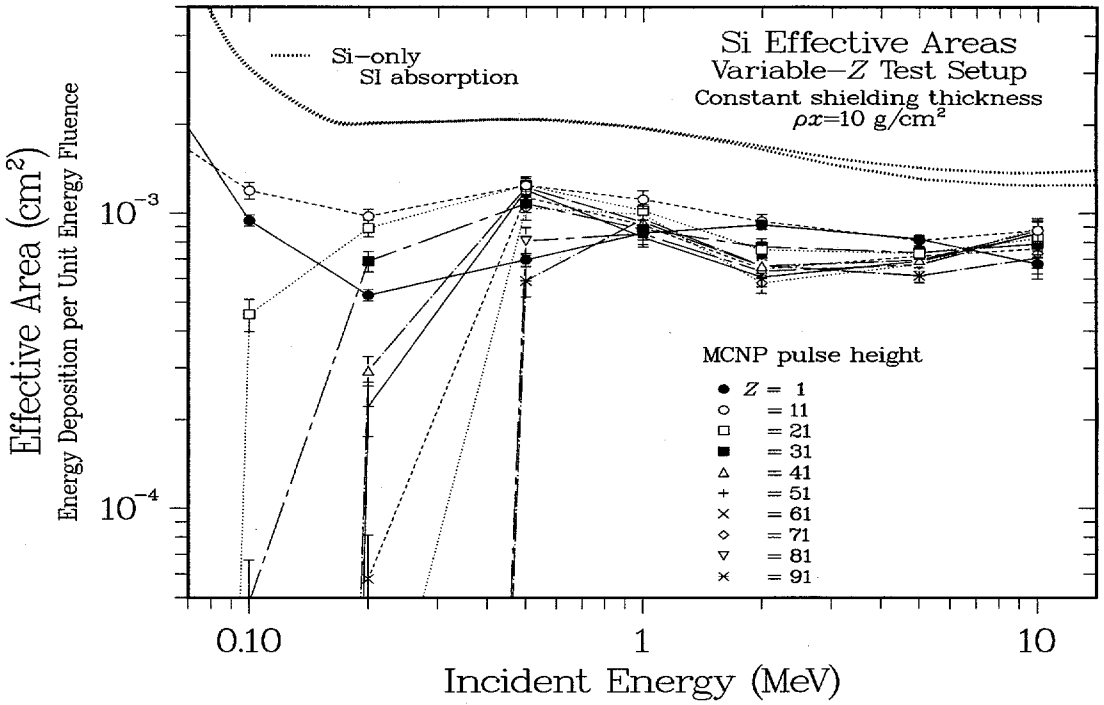

Figure 3.14. Pulse-height effective areas as in Figure 3.12 and Figure 3.13, but for 10-g/cm^2 shielding thicknesses.

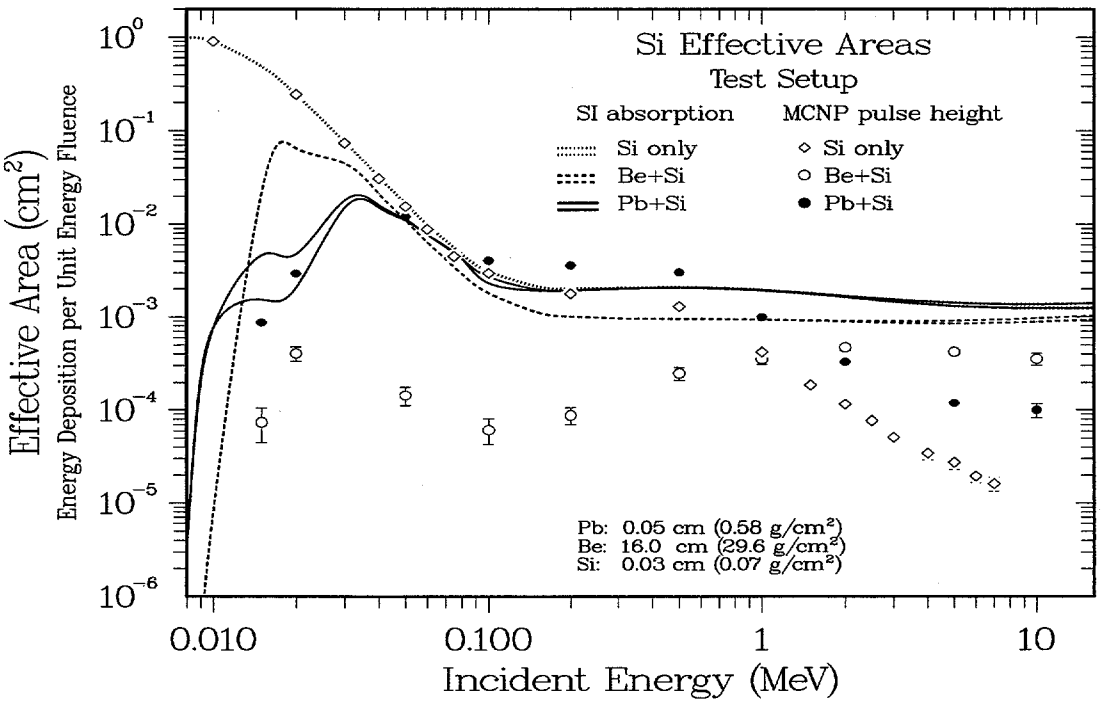

Figure 3.15. Evaluation of two extreme cases of low- and high-Z materials (Be and Pb) that use different wall thicknesses to achieve similar low-energy cutoffs.

Polyethylene-Shielded Diode Detectors. Our last calculation in this chapter concerns an alternative concept for the SPG detector. If secondary electrons are the source of the

response of a Si diode, couldn't we construct a simple gamma-ray detector by simply using a diode plus a large block of CH_2, adding only enough Ta shielding around the diode to provide the desired low-energy cutoff? This approach would eliminate the cumbersome scintillator-plus-photomultiplier combination used in the existing APG and proposed SPG detectors. The results of our calculations are shown in **Figure 3.16**. As before, adding the CH_2 attenuates the incident gamma-ray fluence at low energies and contributes secondary electrons that raise the effective area at high energies. Because the CH_2 cutoff energy is only about 10 keV, a layer of Ta is added to move the cutoff up to about 100 keV. The added Ta raises the effective area at some energies and lowers it at others, but in no case does the efficiency for the full setup significantly exceed the SI absorption values. Thus, the SI estimates remain an upper limit to the available effective area, and increasing either the diode area or thickness would only provide a corresponding linear increase in the effective area. Reproducing the BC400 effective area in Figure 2.18 would therefore require 50–100 separate photodiodes. As shown in the following chapter, reproducing the effective area of an actual SPG detector would require several thousand diodes, which is hardly feasible.

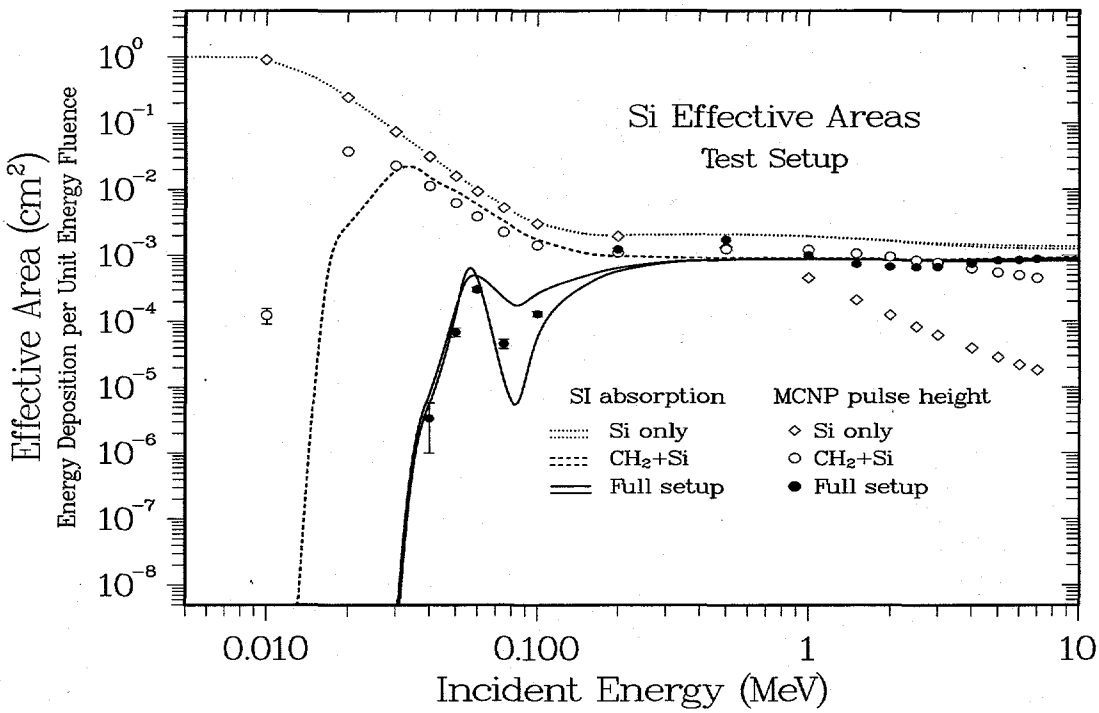

Figure 3.16. Results of an unsuccessful proposal to make a gamma-ray detector using a polyethylene-shielded Si diode.

3.4. Discussion

Evidence for Secondary-Electron Responses. Our goals at the beginning of this chapter were to determine whether the observed APG diode response can be explained as the generation of secondary electrons in the surrounding shielding, which would therefore provide some degree of experimental support for the present calculations. This objective was clearly satisfied by the results discussed in Sec. 3.1, which indicate that the electron response at MeV-range energies indeed approaches the level predicted by the SI absorptions. Next, in Sec. 3.2 we sought to determine whether similar direct radiation sensitivity might exist for the XDS

scintillator-plus-photodiode assembly. As before, the diode's electron response becomes increasingly important at energies above 1 MeV, but now the size and stopping power of the high-*Z* CsI scintillator are probably adequate to ensure that the intended optical signal dominates by at least an order of magnitude. Finally, in Sec. 3.3 we carried out a set of shielding studies that indicate that no changes in shielding material or thickness are likely to significantly reduce the diode's gamma-ray sensitivity at the MeV-range energies of interest. Conversely, because the diode's secondary response closely approaches that estimated using SI absorption coefficients, conclusions[12] based on these coefficients or MCNP heating tallies are probably reasonable in spite of their simplistic assumptions.

4. SPG EFFECTIVE AREAS

Introduction. This chapter seeks to extend the results for the test setup from Chaps. 2 and 3 to the case of the actual SPG detector design. The dimensions of the detector and the mechanics of the calculations are carried over from the corresponding neutron analyses in Ref. 1. To connect with the analyses in previous chapters, we begin by discussing the responses of different arrangements of the detector to gamma rays incident uniformly from all directions. Next, to obtain the detector's energy- and angle-dependent effective areas, individual MCNP calculations are carried out at some 30 different energies for incident plane-wave sources that are rotated about the detector in 10° steps for two different axes. The results are then plotted as functions of angle and energy to determine the important characteristics of the detector response. As in Chap. 2, different combinations of detector shielding are also investigated in order to analyze the effect of different construction options.

4.1. Calculation Geometry

MCNP Layout. The arrangement of the detector and MCNP calculations is shown in **Figure 4.1** and **Figure 4.2**. A listing of the full MCNP input deck is also included in Ref. 1. The central feature of the SPG/SAN assembly is an 8″ long by 6″ high by 5″ thick block of polyethylene. As in Figure 1.1, the four BC400 scintillators are located at the corners of this block to obtain maximum separation. The small indices identify each rod as top or bottom and front or rear. The scintillators themselves are BC400 rods that are 6″ long and 1″ in diameter. The rods are surrounded by 20 mils of Ta shielding and are inserted into cavities in the polyethylene that are 1.25″ in diameter. At the ends of each scintillator there are 0.165″ Pb-glass light guides, and the photomultipliers are represented by voids that extend out to the ends of the block. For the ^{3}He calculations, the two high-sensitivity tubes are placed one above the other and are offset by 0.2″ toward the front of the detector. A placeholder for a smaller low-sensitivity tube is included, but no analysis of the results is included because its specifications have not yet been established. The ^{3}He gas pressures are 4 atm, and the active regions of the tubes are 6″ long for the high-sensitivity tubes and 4″ long for the low-sensitivity tube. One-inch dead regions are included at the ends of each tube; these contain ^{3}He gas but they do not contribute to the MCNP energy tallies. The tube walls are made of 0.051-cm (20-mil) stainless steel (SS), and any spaces between the ends of the tubes and the boundaries of the detector block are filled with polyethylene plugs. The remainder of the geometry is either simple voids or the rotating source planes needed to provide the angular distributions.

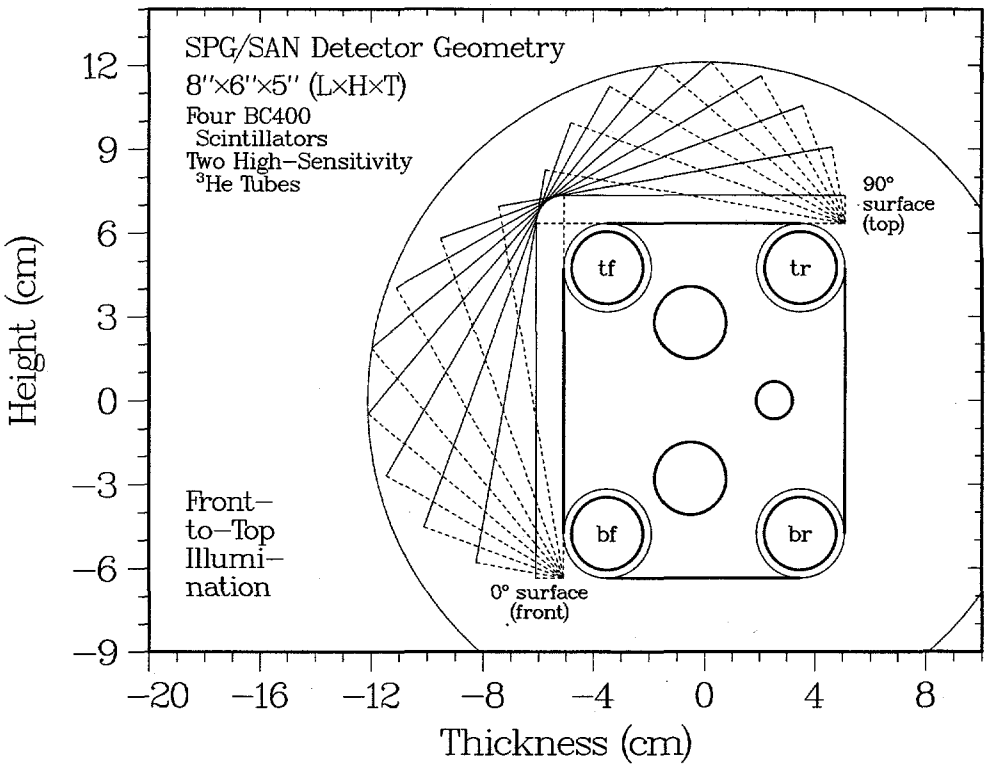

Figure 4.1. End view of the SPG/SAN detector geometry, showing the 10 illuminating planes for a front-to-top MCNP source rotation.

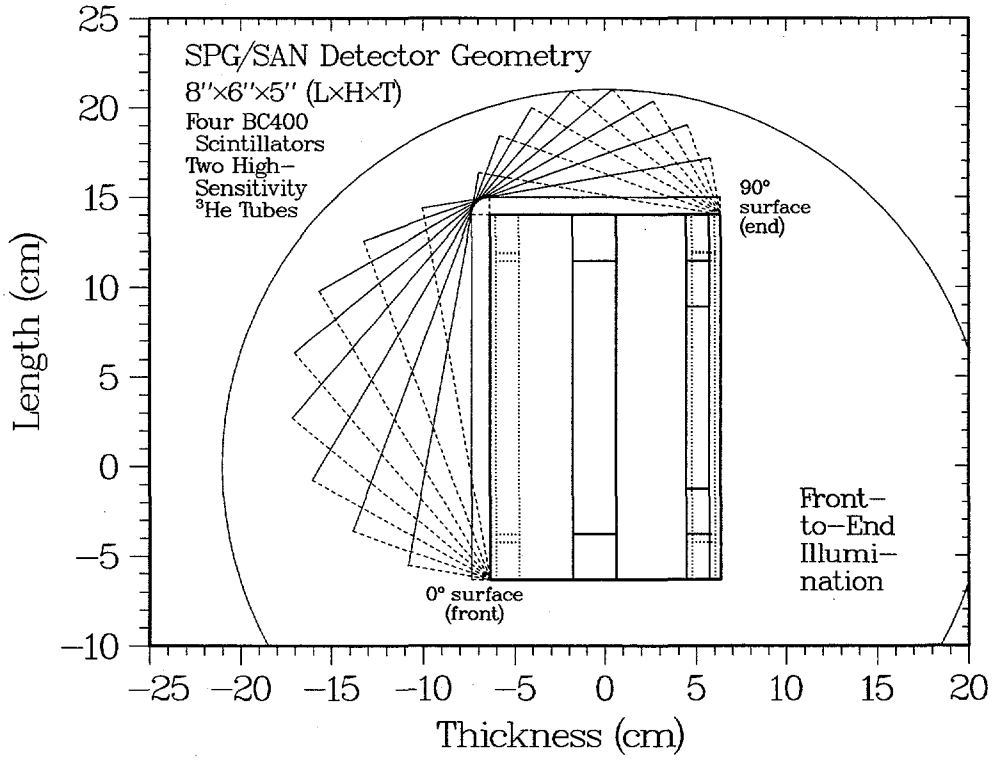

Figure 4.2. Top view of the SPG/SAN detector geometry as in Figure 4.1, but showing the 10 planes for the front-to-end source rotation.

4.2. Uniform Angular Incidence

Pulse-Height Spectra. Our first SPG calculations are intended mainly for comparison to the slab-geometry results in Sec. 2.3, but the response is averaged over all incident directions for simplicity. The pulse-height spectra produced by 1-MeV gamma rays for the bare, Ta-shielded, and CH_2+Ta-shielded BC400 rods are shown in **Figure 4.3**. These results are obtained by dividing the calculated spectra for the sum of all four rods by 4 to obtain the results that would be obtained for a single rod; most of the values in this chapter will be for the summed response. Comparison with the corresponding slab-geometry results in Figure 2.17 shows that multiple scattering in the larger detectors and from the surrounding CH_2 has contributed significantly to the observed pulse-height resolution. Because no detector prototypes have yet been assembled, no additional resolution factors have been included. Because we expect to have excellent light collection and large electronic signals, such factors should not significantly affect our conclusions. Comparison with the slab-geometry results also shows that there is relatively little difference between the bare and shielded spectra, except that scattering has shifted some counts from high to low pulse heights. In general, however, the full three-dimensional calculations indicate that there is a balance between losses to attenuation and inscattering from adjacent material. Similar behavior was reported in Ref. 3 for the case of polyethylene-moderated ^{3}He counters.

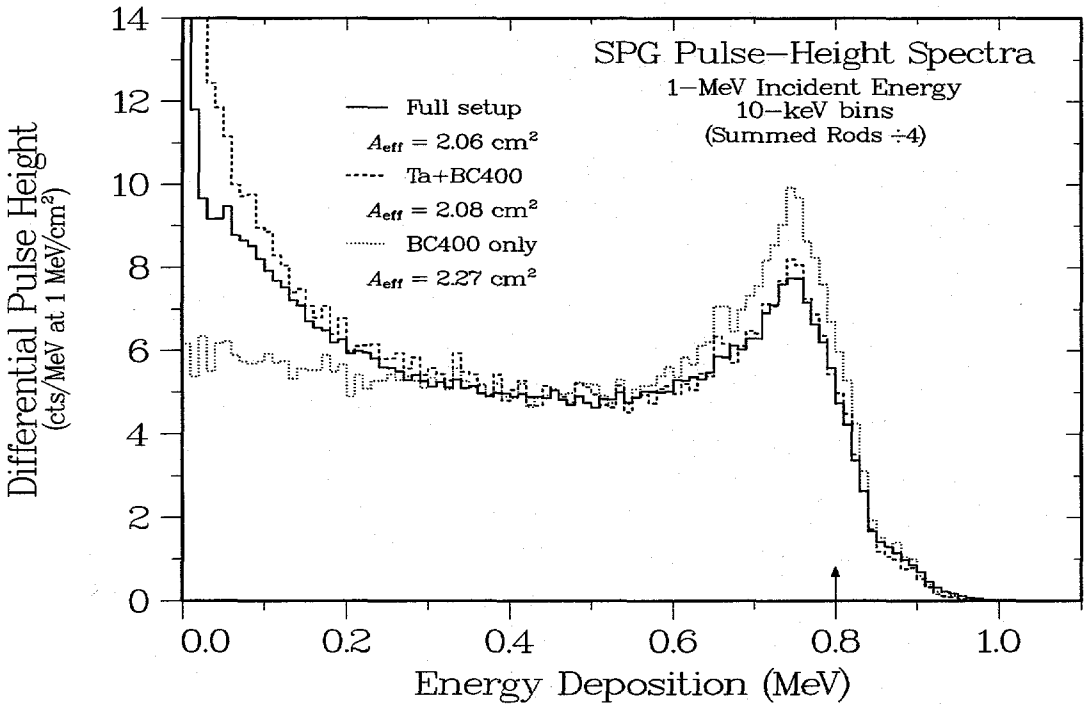

Figure 4.3. Pulse-height spectra for uniform illumination of bare and shielded BC400 scintillators by incident 1-MeV gamma rays. (Compare with results in Figure 2.17 for the test setup.)

Effective Areas. The extensive set of MCNP effective-area calculations for the four bare and shielded BC400 scintillators is shown in **Figure 4.4**; an enlarged view is shown in **Figure 4.5**. The curves are heating tallies; the symbols show pulse-height tallies. For reference, the numerical pulse-height values are listed in **Table 4.1**. At the lowest energies the angle-averaged projected area for the bare scintillators reaches 123 cm^2, which is about 30%

greater than that for the APG detector the SPG is intended to replace. By design, the low-energy cutoff provided by the Ta and Pb-glass shielding is also at the APG energy; note the two *K*-edge cutoffs that result from the angle averaging. The maximum value of about 8 cm^2 in the sum of the shielded effective areas occurs at 0.8 MeV; this sum is about 70% of the corresponding value for the APG detector, which occurs at a slightly higher energy. Above 2 MeV the shielded response is significantly higher than that for the bare scintillators, partly because of inscattering and partly because of secondary electrons. By 10 MeV the increase has reached a factor of about 6. As stated in Sec. 2.2, almost all calculations in this report use the 4A (1993) version of the MCNP code. For comparison, these two figures also show tests (×) that use the same photon and electron cross-section libraries with the newer 4B version of the MCNP code. It is seen that the two calculations are entirely equivalent for the current case.

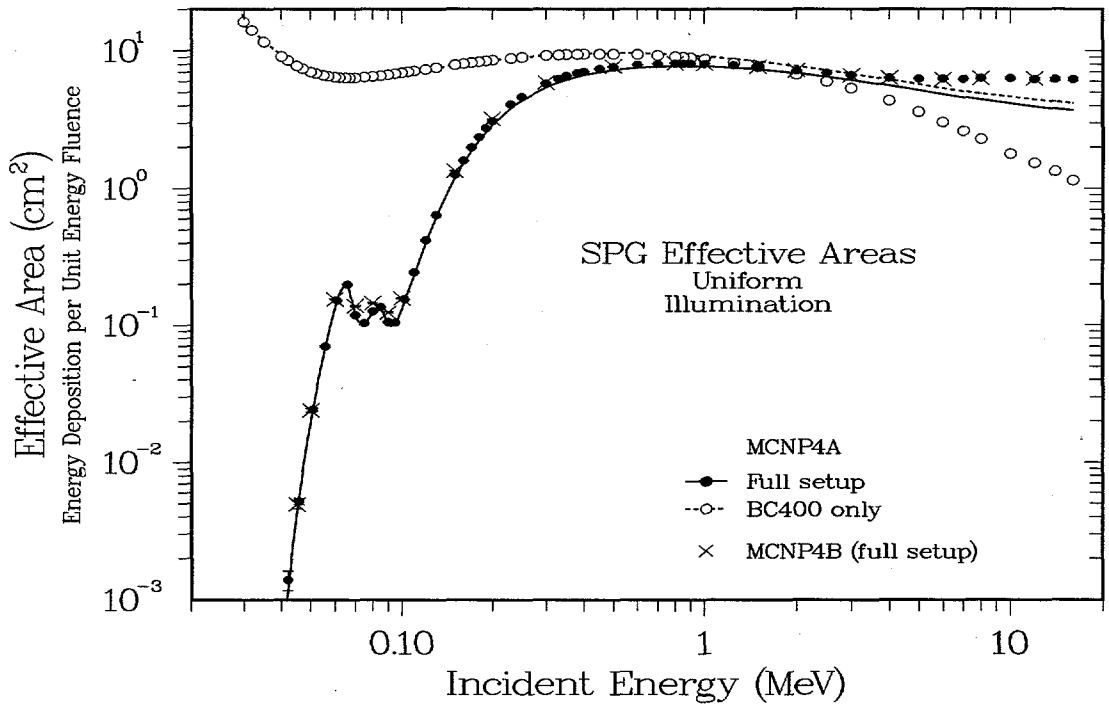

Figure 4.4. Effective areas for uniform illumination of the bare and fully shielded SPG detectors. (Compare with the results in Figure 2.18 for the test setup.)

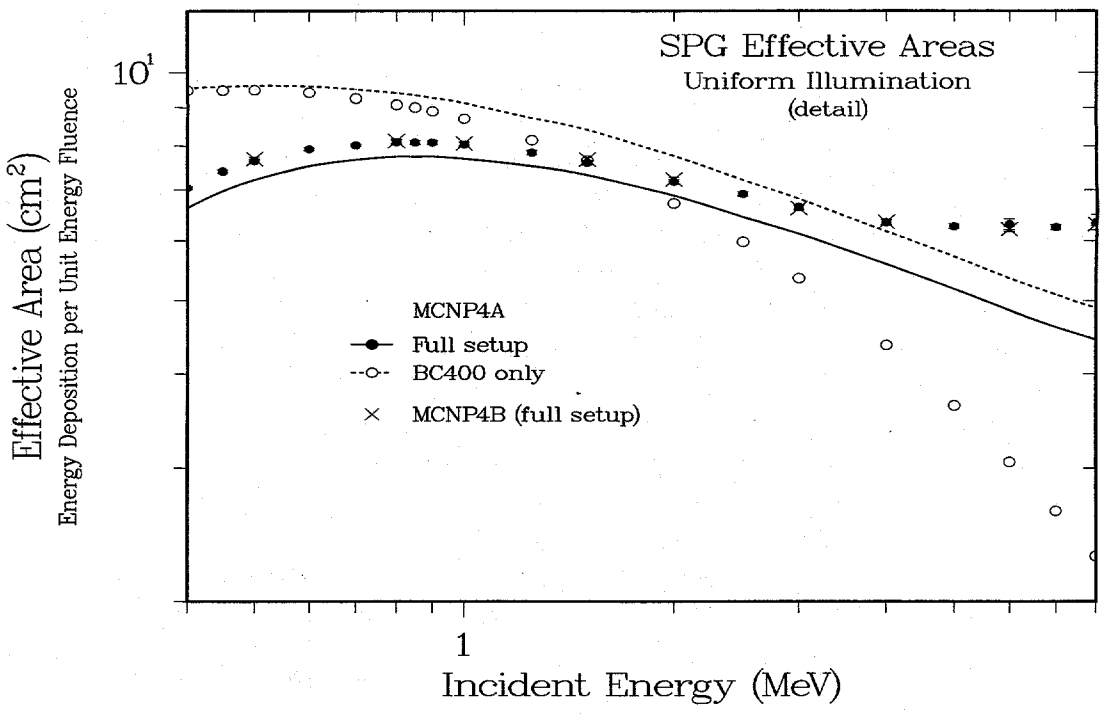

Figure 4.5. Detail of Figure 4.4, showing the calculated effective areas over the region of greatest interest. (Compare with Figure 2.19.)

Table 4.1. Angle-Averaged SPG Effective Areas

Energy (MeV)	Effective Area (cm^2)	Fractional Error	Energy (MeV)	Effective Area (cm^2)	Fractional Error
0.029	0.00000	0.0000	0.300	5.74590	0.0036
0.035	0.00002	0.9624	0.330	6.23080	0.0061
0.040	0.00013	0.3612	0.350	6.55600	0.0049
0.042	0.00139	0.1637	0.380	6.88520	0.0059
0.046	0.00517	0.0525	0.400	7.04660	0.0037
0.051	0.02439	0.0231	0.450	7.40970	0.0047
0.056	0.07000	0.0130	0.500	7.64230	0.0047
0.061	0.15245	0.0084	0.600	7.92240	0.0047
0.066	0.19933	0.0071	0.700	8.01730	0.0037
0.070	0.11878	0.0129	0.800	8.09390	0.0059
0.075	0.10360	0.0134	0.850	8.08730	0.0059
0.080	0.12618	0.0123	0.900	8.08640	0.0059
0.085	0.13596	0.0118	1.000	8.03960	0.0060
0.090	0.10564	0.0127	1.250	7.83970	0.0061
0.095	0.10474	0.0123	1.500	7.59810	0.0063
0.102	0.15530	0.0072	2.000	7.18260	0.0065
0.110	0.24474	0.0158	2.500	6.91430	0.0067
0.120	0.42222	0.0122	3.000	6.64760	0.0069
0.130	0.64216	0.0100	4.000	6.34820	0.0075
0.150	1.26650	0.0108	5.000	6.27100	0.0073
0.160	1.60340	0.0069	6.000	6.31020	0.0165
0.170	1.99740	0.0063	7.000	6.25570	0.0074
0.180	2.37070	0.0059	8.000	6.35210	0.0234
0.190	2.75240	0.0056	10.000	6.32410	0.0183
0.200	3.10230	0.0044	12.000	6.22640	0.0196
0.230	4.09690	0.0069	14.000	6.24180	0.0278
0.250	4.63600	0.0047	16.000	6.22670	0.0280

4.3. Front-to-Top Illumination

Bare Scintillators. Our presentation of the energy and angle dependence of the SPG effective area is divided into two major pieces, one for a source rotation from the front to the top of the detector (see Figure 4.1) and another for the less symmetric case of a front-to-end rotation (see Figure 4.2). Note that both rotations contain a frontal illumination for comparisons. The front-to-top results are given in this section; the next section covers the front-to-end results. **Figure 4.6** shows the energy dependence of the effective areas for the four BC400 rods as calculated using both heating and pulse-height tallies. Up to about 1 MeV the two approaches give essentially the same results; above this energy the loss in energy deposition from escaping electrons becomes increasingly obvious and exceeds a factor of 2 by 10 MeV. Because of the near symmetry of the four-rod arrangement, the 0° (front) and 90° (top) values should be almost the same; the results at intermediate angles are somewhat different but must be almost symmetric about 45°. This is exactly the behavior seen in the angular distributions shown in **Figure 4.7**. At the lowest energies, attenuation through one rod reduces the total response at 0° and 90°; at the highest energy the response is increased by the contribution from secondary electrons. In between, the response is almost flat from 0.5 to 4 MeV.

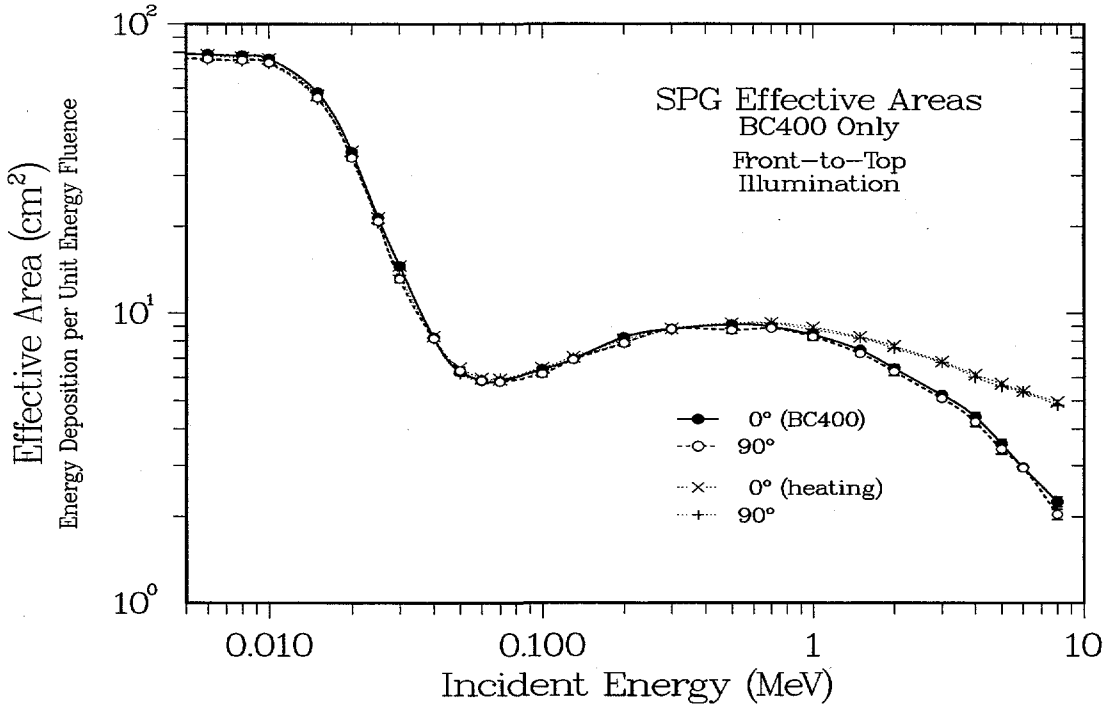

Figure 4.6. Energy dependence of the heating and pulse-height effective areas for front and top illumination of all four BC400 scintillator rods without any surrounding shielding.

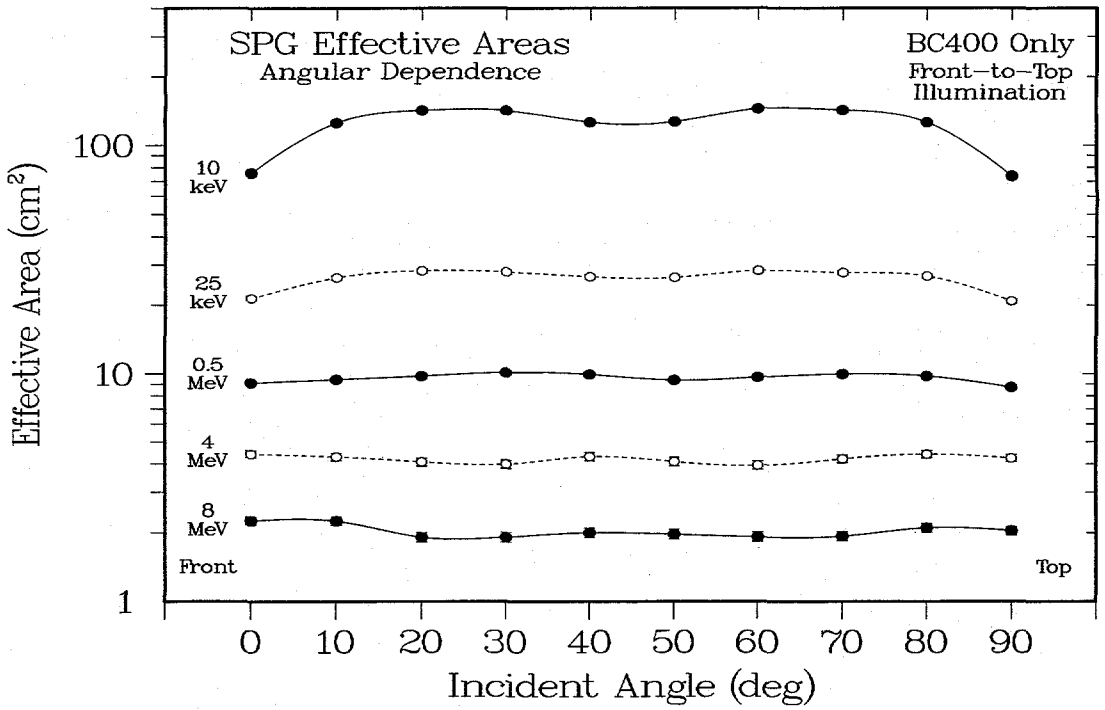

Figure 4.7. Angular dependence of the effective areas for the four bare BC400 rods at several representative energies.

Scintillator Shielding. As seen in **Figure 4.8** and **Figure 4.9**, adding Ta (and Pb-glass) shielding to the bare BC400 rods introduces the expected low-energy Ta cutoff; the Pb has no visible effect for rotations about this axis. At 1 MeV the pulse-height areas are slightly below the heating values, but by 8 MeV the pulse-height areas are slightly higher. As with the slab geometry and the results for uniform incidence, at the highest energies the added shielding serves as a strong source of secondary electrons and significantly increases the response. The slight difference between the shielded values at 0° and 90° is real; the front-to-back distance between detector pairs is slightly less than the top-to-bottom distance, so the effect of crosstalk between rods is slightly larger for 0° illumination.

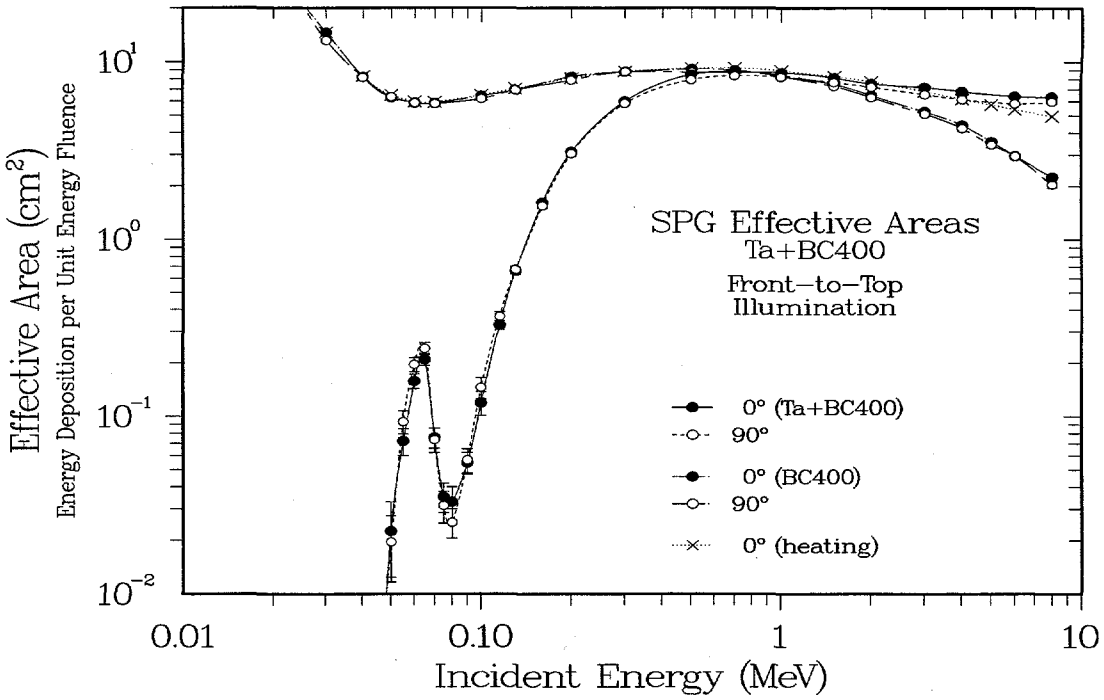

Figure 4.8. Energy dependence of the sum of the effective areas of the four BC400 rods, both bare and with the added Ta shielding.

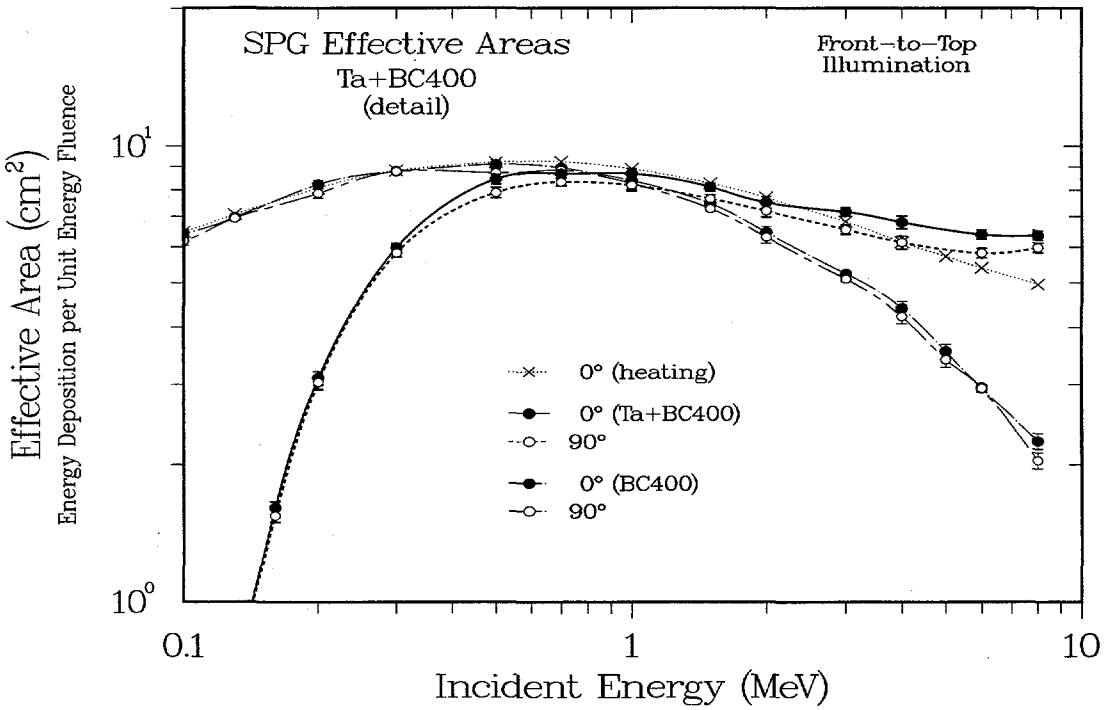

Figure 4.9. Detail of the energy-dependent effective areas in Figure 4.8, showing the behavior at the highest energies.

Full Shielding. The energy- and angle-dependent effective areas for the full complement of CH_2+Ta shielding are shown in **Figure 4.10**, **Figure 4.11**, and **Figure 4.12**. Except at the highest energy, adding CH_2 decreases the total response. Nevertheless, the final result re-

mains very close to the value obtained from SI absorption estimates. The angular responses are similar to those for the bare scintillators in Figure 4.7, although the effect of the CH_2+Ta shielding is somewhat larger than that of the Ta alone. At 1 MeV the largest differences in response have a maximum value of about 20%, although by 4 MeV the distributions are again almost angle-independent. Overall, therefore, the MCNP calculations for the full SPG detector show very similar behavior to the corresponding results for the slab geometry of the test setup in Sec. 2.3.

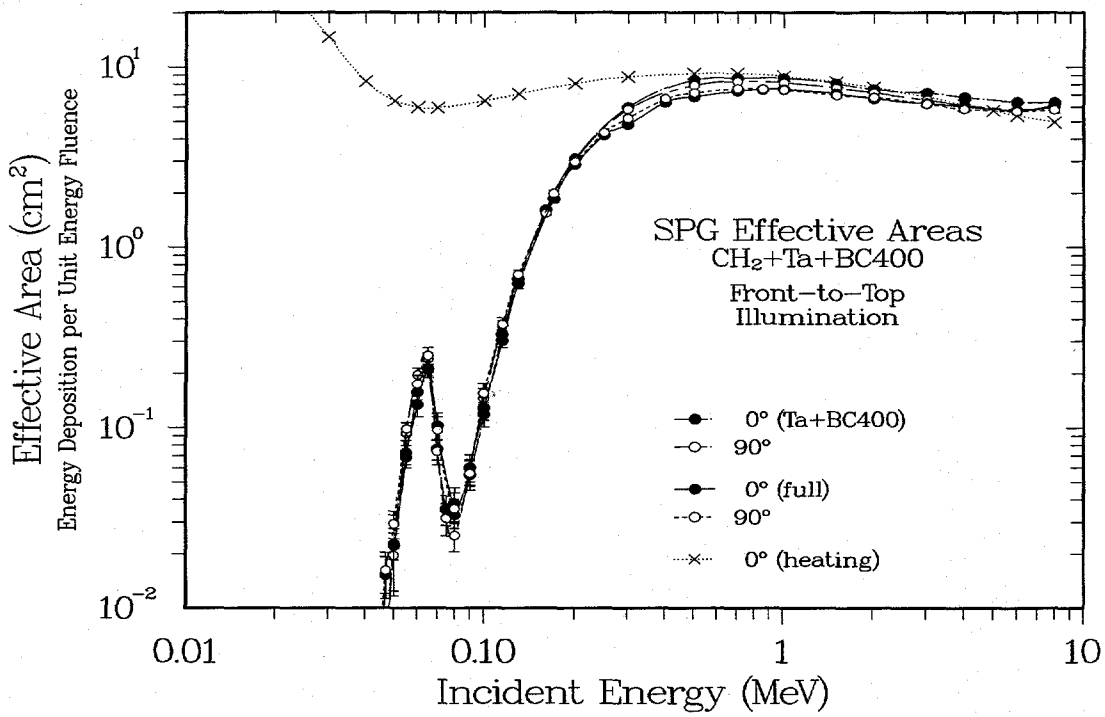

Figure 4.10. Energy dependence of the effective areas of the four BC400 rods, including both the polyethylene and Ta shielding.

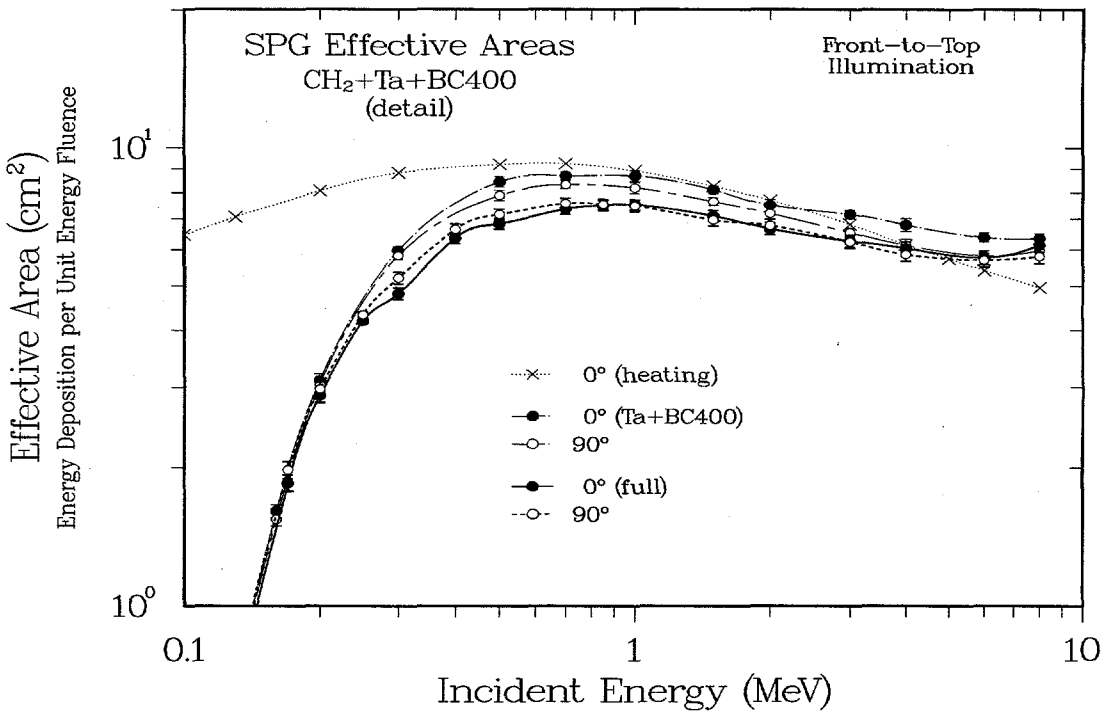

Figure 4.11. Detail of the energy-dependent effective areas in Figure 4.10.

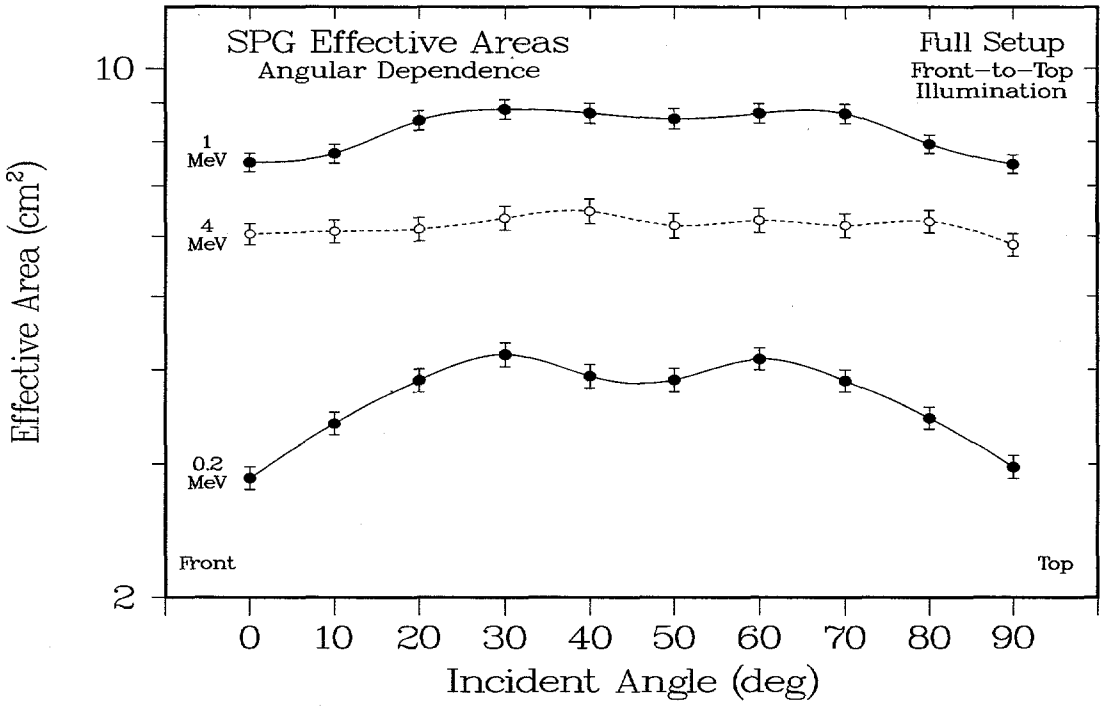

Figure 4.12. Angular dependence of the summed effective areas for the four fully shielded BC400 rods at three representative energies. (Compare with Figure 4.7.) All figures thus far have been for front-to-top source illumination.

4.4. Front-to-End Illumination

Bare Scintillators. Because of the strong front-to-end asymmetry in the detector geometry, the analysis of these calculations is somewhat more complex than for the front-to-top rotations in the previous section. The results for the bare detector are shown in **Figure 4.13** and **Figure 4.14**. As expected, at low energies the 0° (front) and 90° (end) effective areas follow the corresponding value for the projected areas; as the energy increases, the end-on effective areas gradually increase relative to the front-on values. At the highest energies the end-on areas are actually larger than the front-on results because of the high probability of crosstalk for the gamma rays and electrons from Compton scattering. This energy and angle dependence is seen very clearly in Figure 4.14, which also shows that the distributions are almost flat at the MeV-range energies of greatest interest. Note that the crossover behavior differs for the heating and pulse-height tallies. The heating tally reflects only the energy loss of the incident gamma rays, not the actual energy deposited by the secondary electrons.

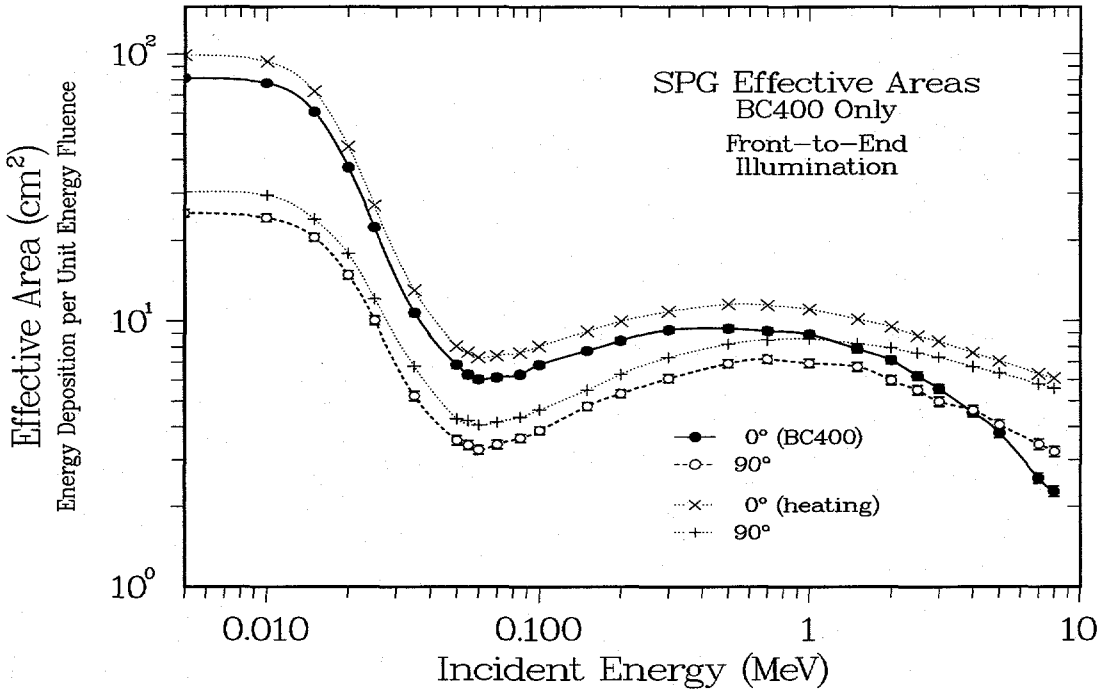

Figure 4.13. Energy dependence of the effective areas for front- and end-on illumination of the four bare BC400 scintillator rods.

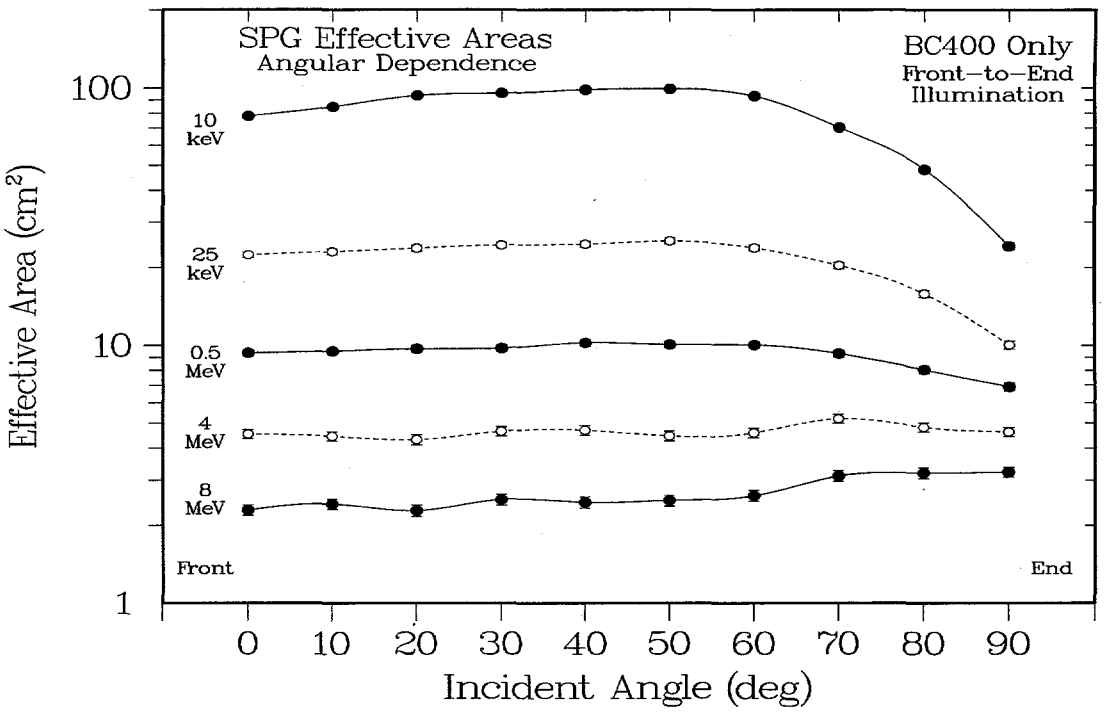

Figure 4.14. Angular dependence of the effective areas of the four bare BC400 rods for front-to-end illumination at several representative energies.

Full Shielding. The energy and angle dependence of the effective areas for the fully shielded detector are shown in **Figure 4.15**, **Figure 4.16**, and **Figure 4.17**. At low energies, the 0° and 90° results show the difference between the Ta (0°) and Pb (90°) *K*-edge energies. As the energy increases, the crosstalk advantage for the end-on geometry increases even more rapidly for the shielded than the unshielded case. Again, however, the angular distribution is almost flat at the energies of greatest interest.

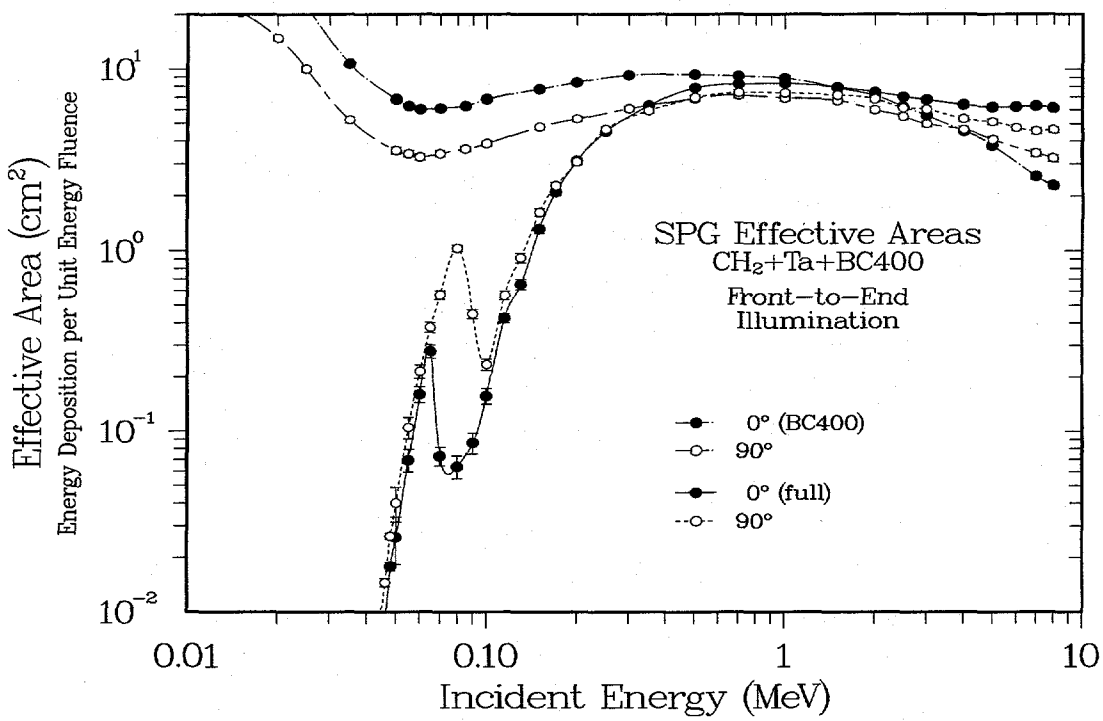

Figure 4.15. Effective areas as in Figure 4.13 for front-to-end illumination of the four BC400 rods, but with full polyethylene and Ta shielding.

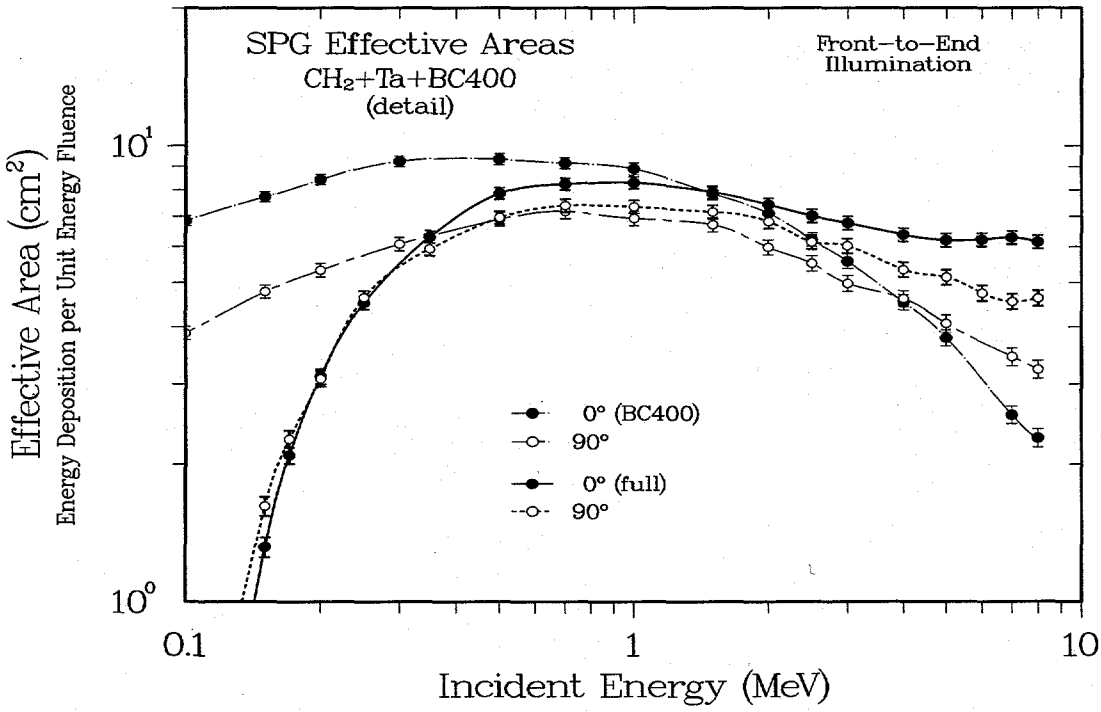

Figure 4.16. Detail of the fully shielded front-to-end effective areas in Figure 4.15.

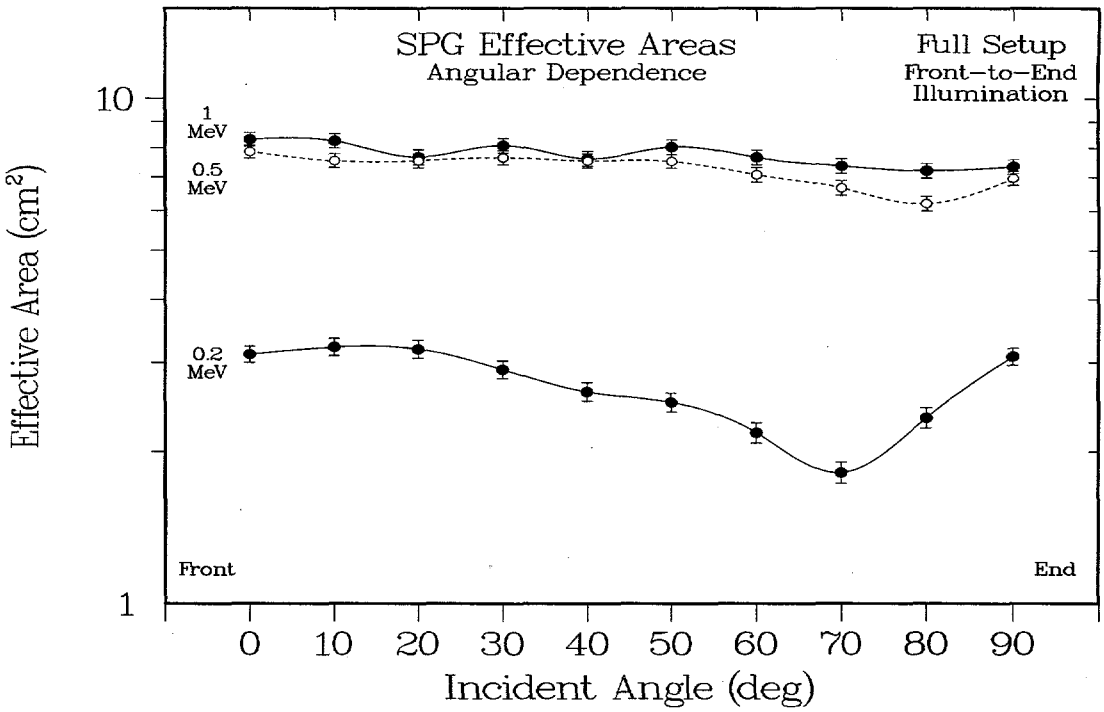

Figure 4.17. Angular dependence of the effective areas for front-to-end illumination of the fully shielded BC400 scintillator.

4.5. Discussion

Energy and Angle Dependence. The general agreement between the performance levels for the proposed SPG detector and those for the existing APG instrument provides a reassuring feeling of continuity in the design assumptions. This situation is at least partly a result of the continued similarity between the full MCNP calculations and the simple estimates from SI absorption, which were the basis of the original APG design. In turn, this similarity is largely associated with the important contribution of secondary electrons to the response of fully shielded detectors at our energies. The effect of these electrons is seen in the crosstalk between scintillator rods, which causes the end-on effective areas to exceed the front-on values at the highest energies, despite the opposing ratio of the projected areas. Finally, the lack of significant angular dependence at the energies of interest eliminates the need to carry an angular degree of freedom throughout our subsequent calculations. Accordingly, the angle-averaged effective areas in Figure 4.4 for a fully shielded SPG detector are one of the major results of the present work.

5. SPG ANGLE MEASUREMENTS

Overview. The angular dependences discussed in Chap. 4 indicate the degree of nonuniformity in the total detector response as a function of the angle of incidence of the gamma-ray signal. In contrast, for a multielement detector such the SPG instrument, differences between the magnitudes of the responses of the four individual rods can be used to estimate the direction of the incoming signal from entirely internal detector quantities. A variation of this directionality technique is discussed in Ref. 17, and thorough discussions are given in Refs. 22 and 23. Aside from providing possibly useful information about the source location, these interelement differences should provide a valuable background-rejection technique, because environmental effects may have a signature that is very different from the signals of interest.

5.1. Asymmetry Formalism

Response Differences. The basis of the directional approach is the differences between the responses of detectors elements at different locations, usually because of attenuation of the signal in transiting the detector. For our SPG case we can define an asymmetry factor R from the difference between the responses of pairs of opposite rods divided by the sum of those responses. We have two options, depending on whether the angle is measured in the front-to-top or the front-to-end plane of rotation (see Figure 4.1 and Figure 4.2). For the front-to-end rotation, there are only two independent measurements, one for each pair of front or back rods. For the front-to-top rotation, there are four different measurements, one for each rod. If we use combinations of the indices t, b, f, and r to identify the four rods as top or bottom and front or rear (see Figure 4.1), we can define two asymmetries for axes oriented along the detector diagonals:

$$R_x = (R_{tf} - R_{br})/(R_{tf} + R_{br}) \qquad R_y = (R_{bf} - R_{tr})/(R_{bf} + R_{tr}) ,$$

whose average $R_a = (R_x + R_y)/2$ defines an average asymmetry. For the front-to-top case, R_x and R_y are independent; for the degenerate front-to-end case, $R_a = R_x = R_y$. For the high attenuations across the detector at the lowest energies, R_a approaches its maximum value of 1.0. As the energy increases, the attenuation decreases, and R_a goes to 0.0. This behavior is seen in **Figure 5.1** and **Figure 5.2** for the maximum and minimum R_a values calculated from our front-to-top rotation. As in previous figures, the plotted points are calculated from the pulse-height tallies, and the lines use the results from the heating tallies. The maximum asymmetries are at 0° and 90°, which have approximately equal values because of detector symmetry. Similarly, the minimum values occur at 30° and 60°. For the front-to-end values shown in **Figure 5.3**, the R_a values continually decrease as the angle decreases, and by symmetry they go to zero for the exact end-on case. In general, these asymmetry values are useful as a simple measure of the difference between the signal amplitudes in the individual rods. For example, for energies around 1 MeV the difference between the individual-rod signals is at most 30%. In the present discussion, however, the R_a values also indicate the detector's ability to determine the direction of the incident fluence; for this reason their maximum values are often referred to as the detector's analyzing power.[23] If R_a is zero, there is no difference in signal level across the detector, so there is no information about the source direction.

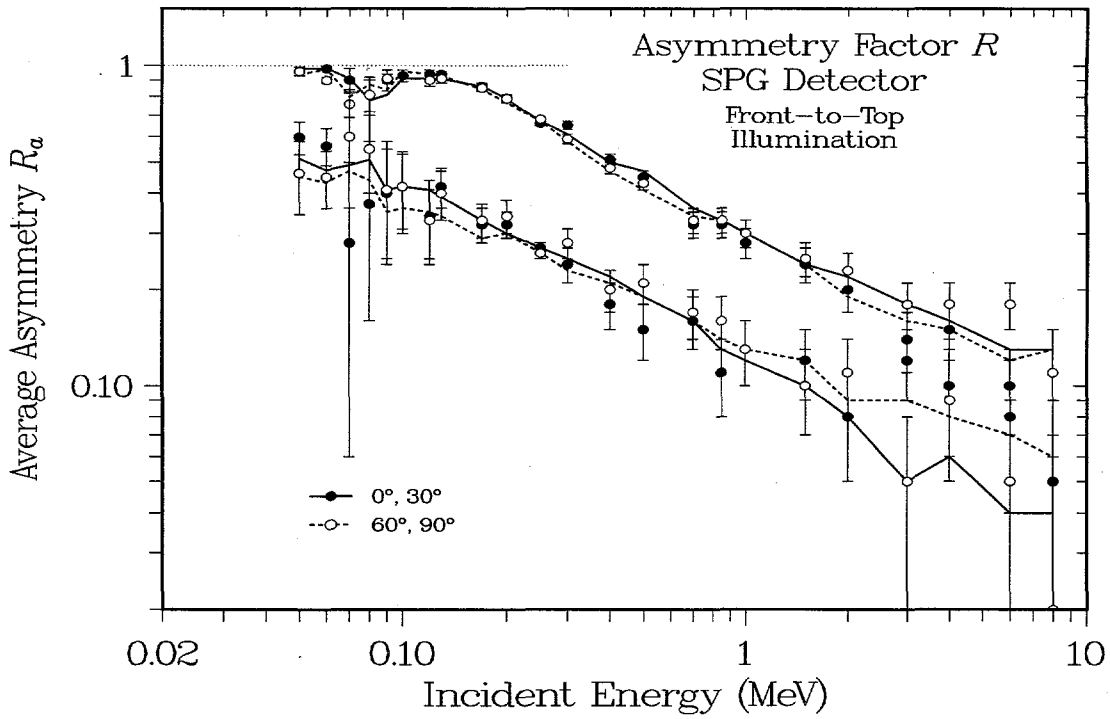

Figure 5.1. Energy dependence of the average diagonal asymmetry R_a for particular angles in the front-to-top illumination of the SPG scintillators.

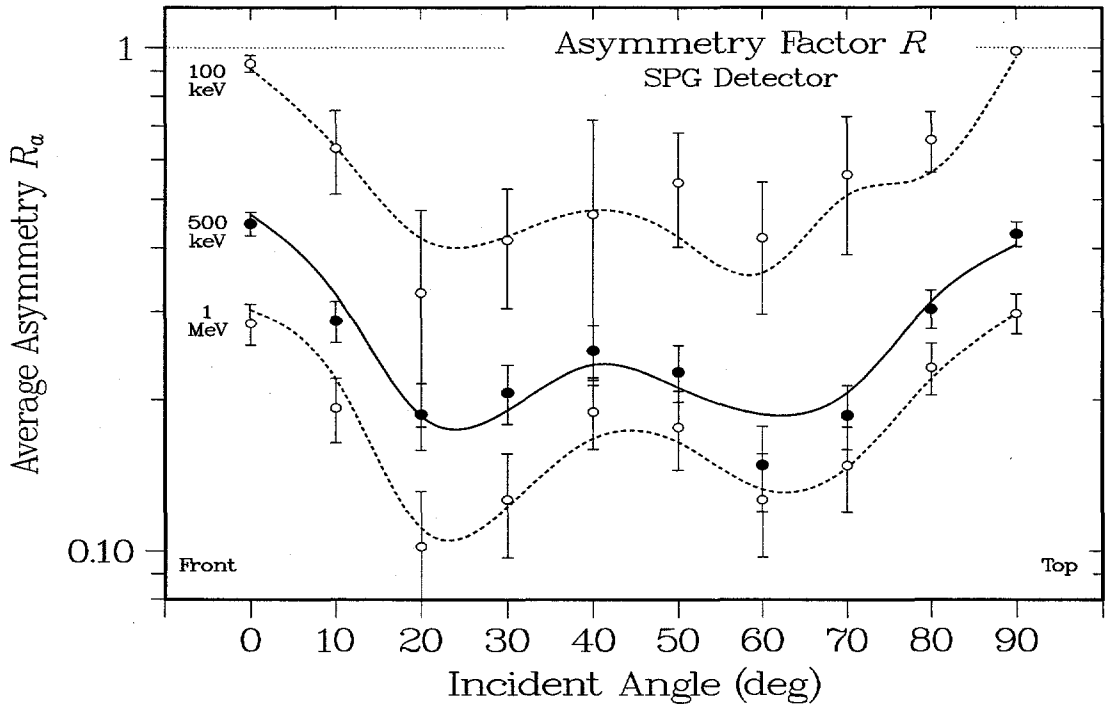

Figure 5.2. Angular dependence of the average diagonal asymmetry R_a for particular energies in the front-to-top illumination of the SPG detector.

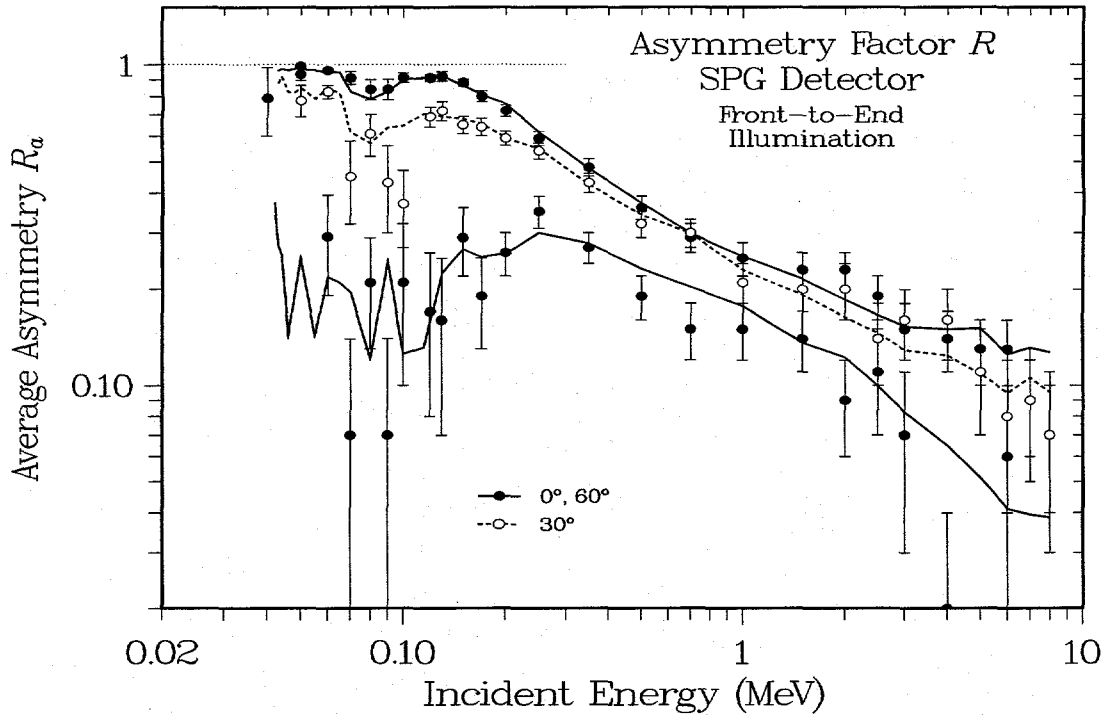

Figure 5.3. Average diagonal asymmetry R_a as in Figure 5.1, but for particular angles in the front-to-end illumination of the SPG scintillators.

5.2. Angle Determinations

Two-Rod vs. Four-Rod Approaches. There are two methods for computing the source angle from the signals for the four rods, depending on whether the angle of rotation is front-to-top or front-to-end. For the front-to-end rotation, the ratio between the observed and maximum R_a values gives the cosine of the source angle; that is, $\theta = \arccos(R_a/R_{max}) - \pi/4$, where the 45° shift aligns the diagonal axes with our detector coordinates. Unfortunately, because we do not know the average energy, we cannot obtain a maximum R_a value, so the source angle would be very poorly determined. (See Ref. 22 for some examples of this two-rod approach for incident neutrons.) This limitation can be avoided for the front-to-top case because there are four independent measurements. In the four-rod method, the calculation uses the two orthogonal asymmetry factors R_x and R_y defined above. For sources located along the detector diagonals, the corresponding R_i value goes through its maximum and the remaining R_j value goes through zero. The R_x and R_y values therefore behave like the two components of a vector, and their ratio gives the source direction relative to the two detector diagonals. Significantly, the ratio approach cancels out the magnitude of the energy-dependent R_a value, so we do not need to know the energy distribution of the incident signal in order determine its direction. **Figure 5.4** shows the resulting correlation between the actual and calculated angles at several different energies. Within statistics, the calculated value is accurate for 0°, 45°, and 90°, consistently high for 20–30°, and consistently low for 60–70°. This pattern is also seen in **Figure 5.5**, which shows the energy dependence of the calculated angles in a different format.

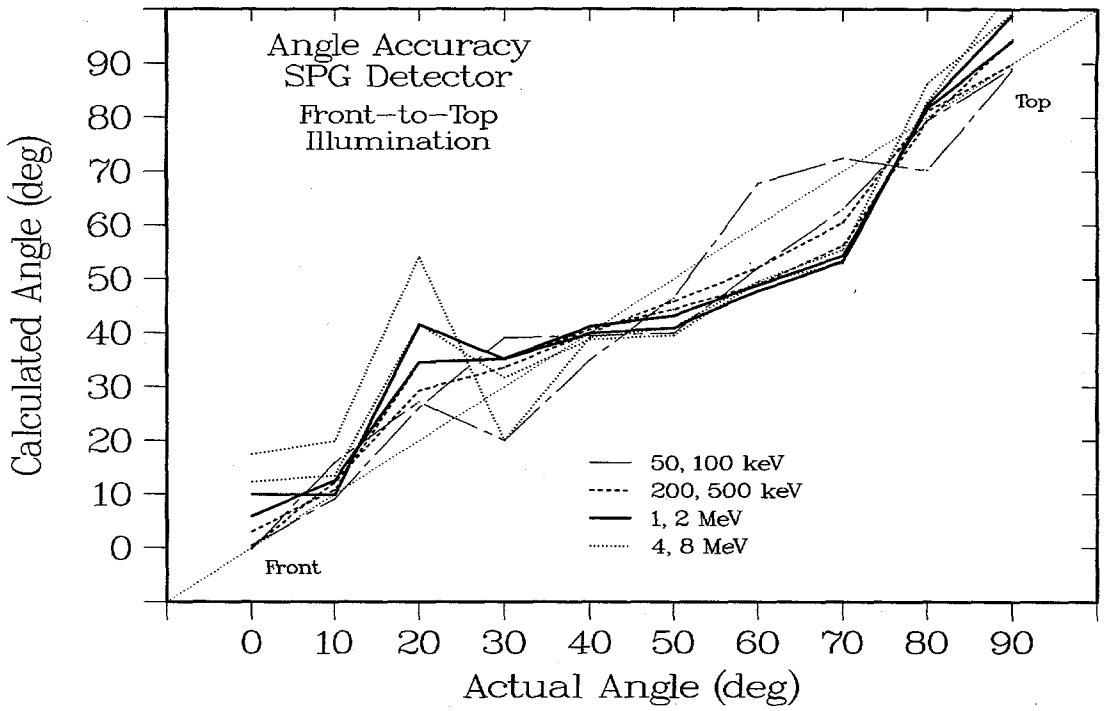

Figure 5.4. Correlation between the actual and calculated incident angles for front-to-top illumination of the SPG detector at several different energies.

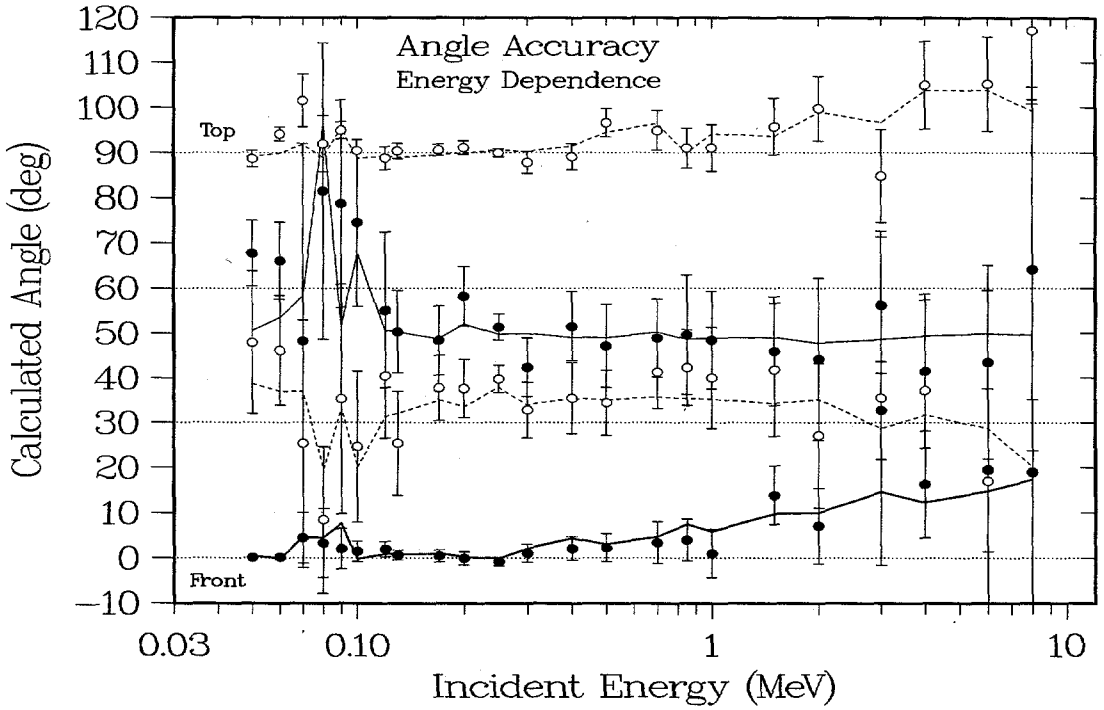

Figure 5.5. Energy dependence of the angle calculations as in Figure 5.4 for several representative angles.

5.3. Discussion

Directional Capabilities. Although angle determinations are not a central issue in the design of the SPG detector, the ready availability of four widely separated detector elements makes the technique possible without any change in the detector hardware. This situation differs from that for the SAN detector's neutron response, where an increase in the asymmetry factor needed for accurate angle measurement comes at the expense of a decrease in the detector's effective area.[1] In the present case, the major utility of the detector's directionality is probably not the rather imprecise determination of source angle; instead, a calculation of an average R_a value provides a useful technique for rejecting environment backgrounds. By far the largest number of charged-particle events will be one- and two-rod cosmic-ray transits, which cannot directly deposit energy in a third or fourth rod. Spallation events, however, could produce simultaneous signals in all four rods, but the magnitudes of the signals should be very different; in particular, it should be unlikely for more than one rod to have a very large signal. Thus, one of the important requirements for a potential signal is that the diagonal asymmetry components must be no larger than 50%. A subsequent requirement could then be that the measured asymmetries are consistent with those for the expected source location.

6. SPG PULSE RESPONSE

Problem Statement. The energy- and angle-dependent effective areas in Chap. 4 provide the energy depositions for gamma-ray fluences incident on the detector from any direction. However, such quantities are not sufficient to determine the actual detection threshold. In practice, the energy-deposition threshold for the individual rods should be high enough to reject most of the events caused by minimum-ionizing cosmic rays. For a typical energy loss of 1.6 MeV per g/cm^2, a scintillator density of 1.032 g/cm^3, and a rod diameter and length of 2.54 cm and 15.2 cm, the expected cosmic-ray spectrum should have a peak at around 6 MeV and a high-energy tail extending to about 25 MeV. If we set a threshold at 10 MeV and expect gamma-ray energies of a few MeV, the corresponding single-rod effective area of 2 cm^2 corresponds to an incident energy fluence of 5 (= 10/2) MeV/cm^2, which gives an average particle fluence of just over 3 γ/cm^2. Depending on the value assumed for the projected area of a single rod, this particle fluence corresponds to a number of incident photons between 15 and 100. Considering that only a fraction of this total will contribute to the signal in a given rod, it is clear that understanding the effect of different threshold settings requires an additional statistical analysis. The first steps in such an analysis are the subject of this chapter.

Overview. In principle, we could calculate the total energy deposition for multiple incident gamma rays by simply modifying the MCNP source to accumulate pulse heights over an entire run rather than for each incident photon. Because we would need a large number of such runs in order to provide good statistical precision, we have instead devised a method that builds a Monte Carlo analysis on top of the MCNP results from previous chapters. We begin by developing a technique for sampling N times from the single-rod pulse-height distribution produced by an incident gamma-ray energy fluence of 1 MeV/cm^2. This sampling procedure provides the total energy deposition that would be produced by an instantaneous incident fluence of N MeV/cm^2. Statistically, this particular deposition value is only one example out of many possible results, so the process must be repeated many times to sample the full range of total pulse heights. To provide diagnostics on each set of samples, we can calculate such population variables as the standard deviation and mean of the distribution, which would be located at the value NA_{eff} in the case of 1-MeV photons. To eliminate background events, in the proposed SPG operating mode a fourfold coincidence will be required between the signals in the four rods; that is, the pulse height in each rod must exceed a set threshold value. For this case, from each set of samples we can accumulate a histogram of the lowest value of the four pulse heights. The fraction of the histogram area above each pulse height then gives the probability of meeting the coincidence requirement at each threshold. As N increases, the summed pulse-height distribution should become narrower and eventually converge to the NA_{eff} value; the threshold setting should be just below this value. Repeating the entire process for many different values of N provides a relation between detection probability, incident energy fluence, and pulse-height threshold. This complete analysis is carried out in Sec. 6.1 for the artificial case of 1-MeV gamma rays illuminating the detector uniformly over angle. In Sec. 6.2 we repeat the analysis for incident gamma rays in six energy bins from 0.1 to 12 MeV, and in Sec. 6.3 we consider the effect of different incident angular distributions. Section 6.4 extends the analysis to include the effect of simple time dependences, and Sec. 6.5 estimates the overall uncertainties in the calculations. Sec. 6.6 summarizes the results.

6.1. Monte Carlo Technique

Pulse-Height Spectra. Our starting point is a pulse-height spectrum like that shown in Figure 4.3, which is normalized to give the distribution of energy depositions for an isotropic incident gamma-ray energy fluence 1 MeV/cm^2. For simplicity, we also begin with a source energy of 1 MeV, so the particle fluence is unity. With this normalization, incident gamma rays that deposit no energy in a particular rod are accumulated in a bin at zero energy. The four individual-rod spectra are shown by the light lines in **Figure 6.1**. The two effective areas are our usual energy-absorption area A^E_{eff} and the photon-counting area A^γ_{eff}. One (A^E_{eff}) corresponds to the energy-weighted spectrum integral, the other (A^γ_{eff}) to an unweighted spectrum area. We can improve the statistical precision by averaging over the spectra for all four rods, which gives the result shown by the open circles. To generate additional pulse-height spectra from this starting point, we first divide each of the individual pulse-height spectra by its area A_0 to renormalize the distribution to unit area. For each rod, we calculate an intermediate distribution $y(E_S)$ by numerically integrating this distribution from $-\infty$ to E_S. If we then use an interpolation routine to invert $y(E_S)$, we obtain a sampling distribution $E_S(y)$, where y is a random variable over the interval from 0 to 1. Repeatedly calling a random-number generator m times, dividing by m, and then multiplying by the original area A_0 provides a set of regenerated pulse-height distributions for the individual rods. In **Figure 6.2** these regenerated spectra (×) are compared with the original average spectrum (○). Note that we have preserved the original normalizations, with an average effective area for energy absorption of 2.05 cm^2 and a corresponding particle-counting area of 5.24 cm^2, or about 4%.

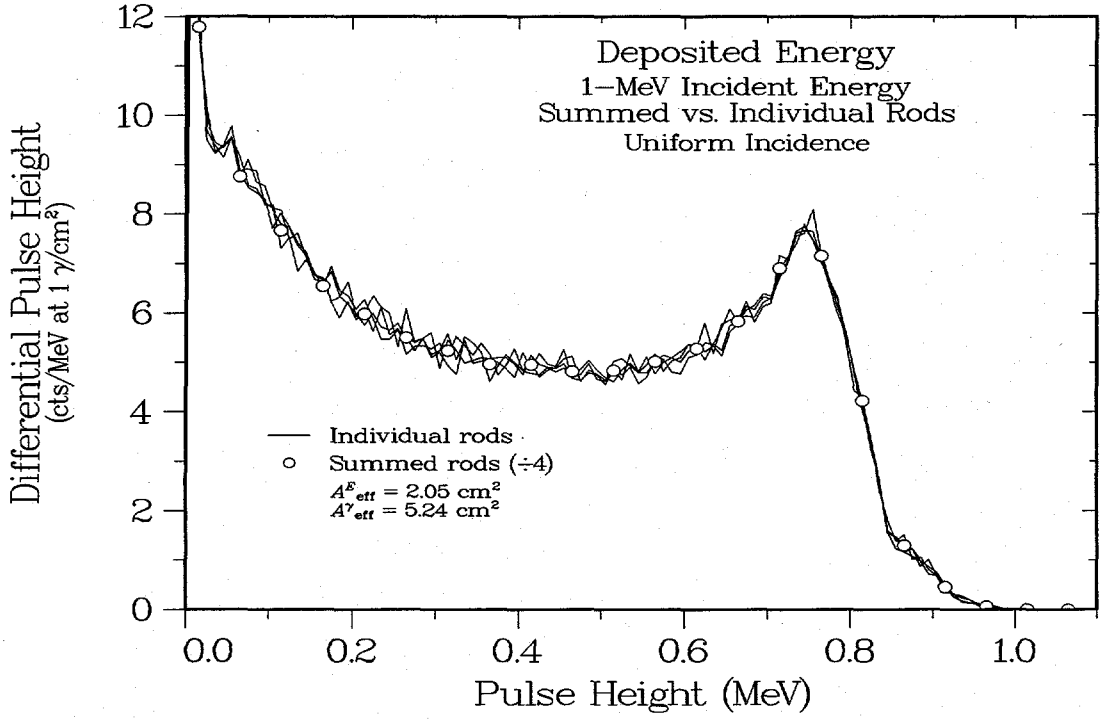

Figure 6.1. Individual-rod pulse-height spectra produced by 1-MeV gamma rays uniformly incident on the SPG detector.

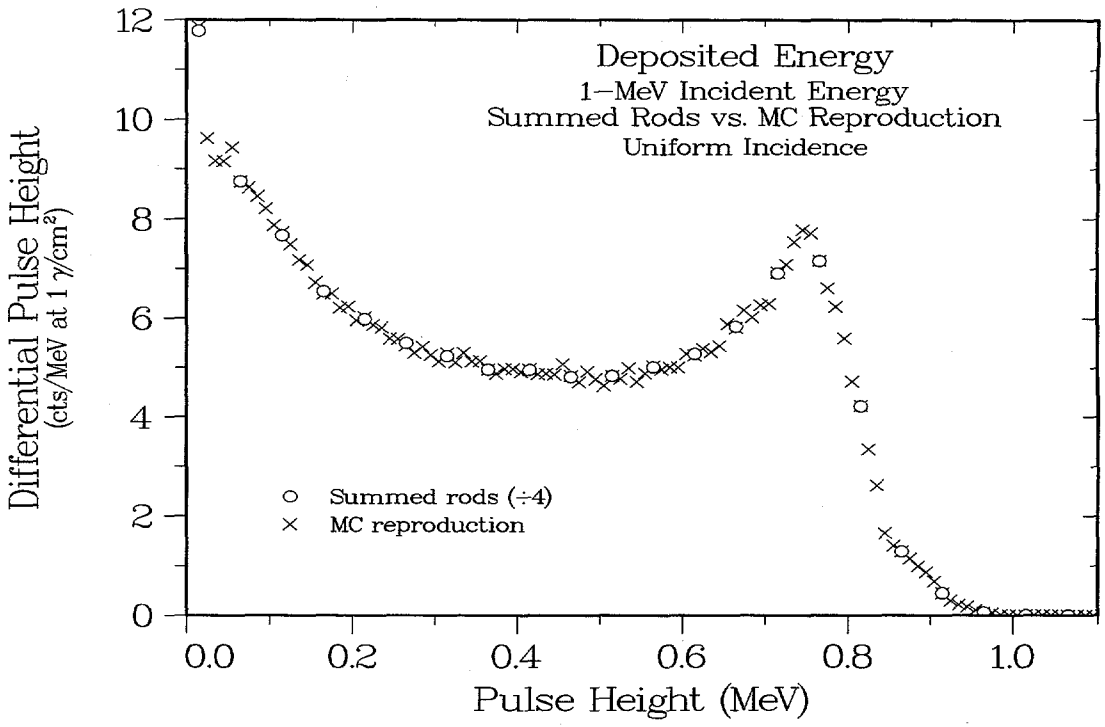

Figure 6.2. Comparison between the average spectrum from Figure 6.1 and the corresponding spectrum calculated as a Monte Carlo reproduction.

Pulse Pileup. Now that we can sample pulse heights from the original MCNP distribution, we can simply sum the results of N such samples to produce the result that would be produced by N simultaneous incident photons. Each sum represents a single incident gamma-ray flash; repeating the summation many times gives a distribution of such pulse-height sums. **Figure 6.3** shows the distributions obtained for sums at $N = 10^n$, with $n = 0, 1, \ldots, 6$. As n increases, the pulse-height sums converge to the average values $\Phi_E A_{\text{eff}} = 10^n A_{\text{eff}}$ (in MeV), just as expected for large gamma-ray fluences. As an example, consider the pulse-height threshold of 10 MeV that was suggested above as providing reasonable rejection of cosmic-ray singles events. According to Figure 6.3, incident pulses of multiple 1-MeV photons would never reach this threshold at a fluence of 1 MeV/cm^2, but at 10 MeV/cm^2 such pulses would almost always exceed the threshold. Because the proposed SPG operating mode will use a fourfold coincidence between the four individual-rod pulse heights to eliminate environmental backgrounds, instead of using the sums in Figure 6.3 we must accumulate the probabilities that all four rods exceed any given threshold. We must therefore rerun our sampling program, again summing up the pulse heights for N incident photons at a time. For each sum, however, we then know the lowest of the four summed pulse heights, which determines the minimum threshold that satisfies a fourfold coincidence for that particular sum. Repeating the summation many times for each value of N gives the set of probability distributions shown by the symbols in **Figure 6.4**. Summing each of these probability distributions downward in pulse height gives the integral probabilities shown by the curves, which give the probabilities that all four rods exceed the pulse-height thresholds listed on the x axis. As before, we see that incident pulses of

1-MeV photons will never exceed a fourfold 10-MeV threshold at a fluence of 1 MeV/cm^2, but they will almost always pass the test at a level of 10 MeV/cm^2.

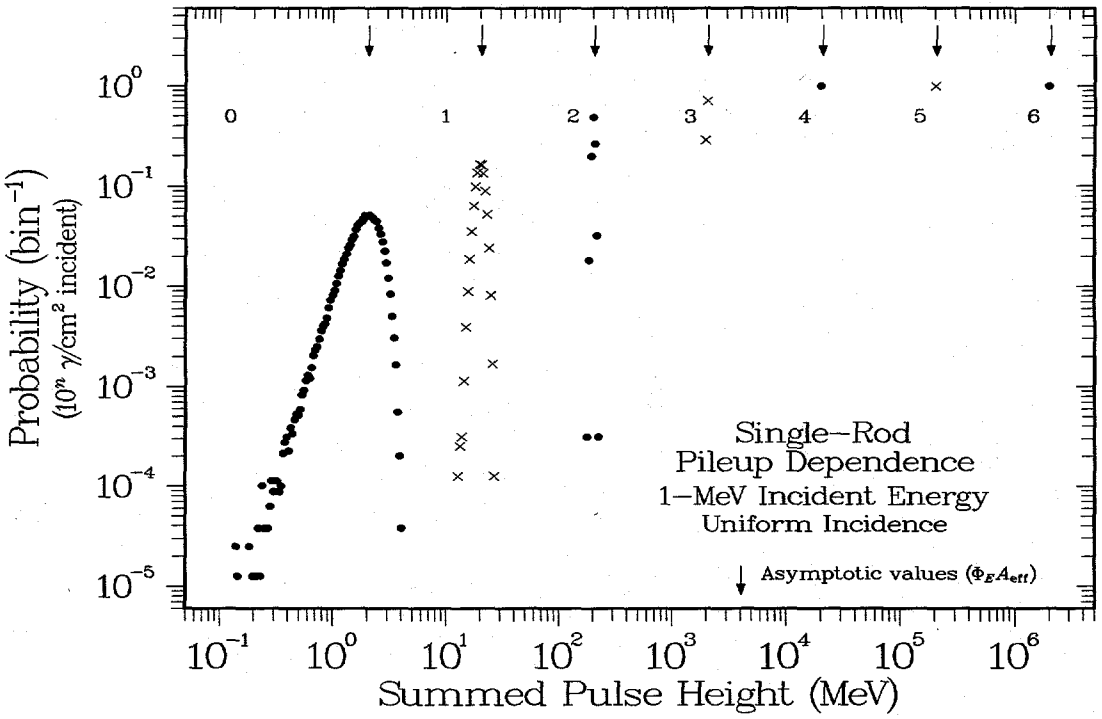

Figure 6.3. Pulse-pileup distributions for multiple simultaneous events in a single rod.

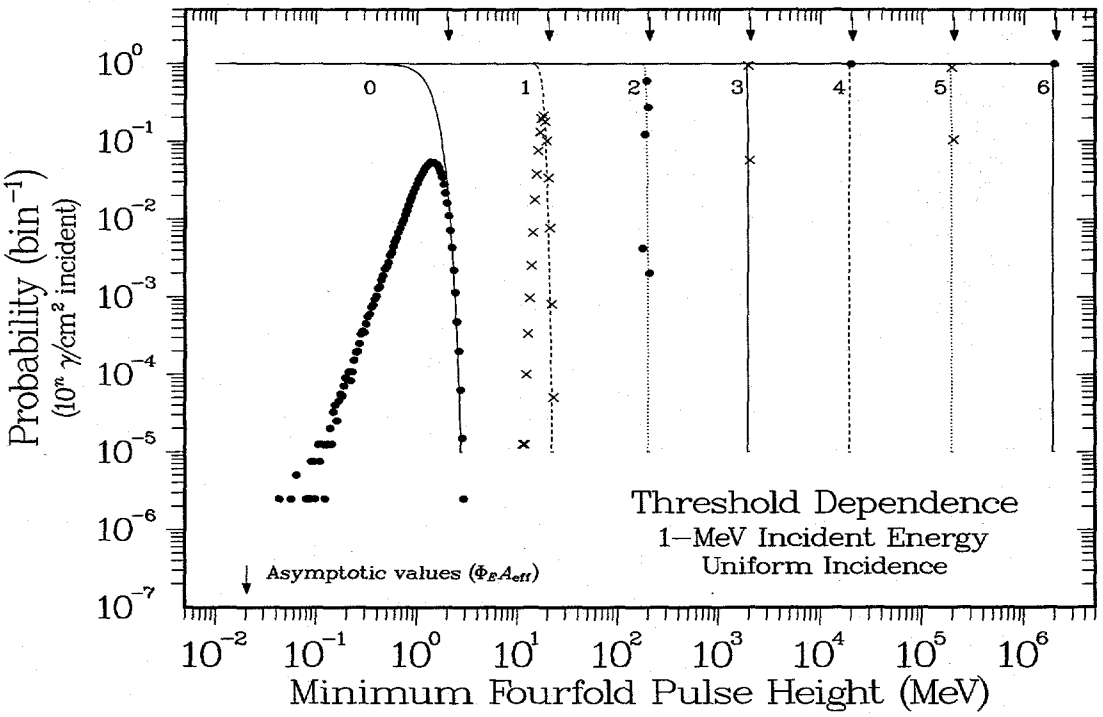

Figure 6.4. Distributions of the probability for exceeding the threshold energy in all four rods as calculated from the pulse-height distributions in Figure 6.3.

Threshold Dependence. The integral probability distributions in **Figure 6.4** can be interpolated to determine the pulse-height threshold needed to attain any specified level of detection probability. The pulse-height thresholds needed to attain a 99% detection probability are shown in **Figure 6.5** along with the mean and standard deviation of the single-rod pulse-height distributions in Figure 6.3. At high fluences there is little difference between the thresholds and the mean values, but at low fluences the thresholds must be set far below the mean values in order to reach the 99% level. For example, the plotted × symbol indicates 99% of the pulses at a fluence level of 7 MeV/cm^2 will exceed a pulse height of 10 MeV. Thus, at the recommended 10-MeV threshold the SPG detector can be expected to provide consistent detection only at energy fluences above 7 MeV/cm^2. Alternatively, if the required fluence threshold were at a higher value, for example, 16 MeV/cm^2, the pulse-height threshold could be raised to 25 MeV, which would eliminate essentially all cosmic-ray singles events. Next, because the threshold scales with incident fluence, **Figure 6.6** provides a useful alternative display obtained by dividing the threshold levels by the incident fluences, which gives a quantity with dimensions cm^2. As indicated in the figure, this form of presentation makes it clear that the threshold values asymptotically approach the single-rod effective areas as the energy fluence increases, just as expected. The presentation also provides an easily readable summary of the relation between pulse-height threshold and incident energy fluence.

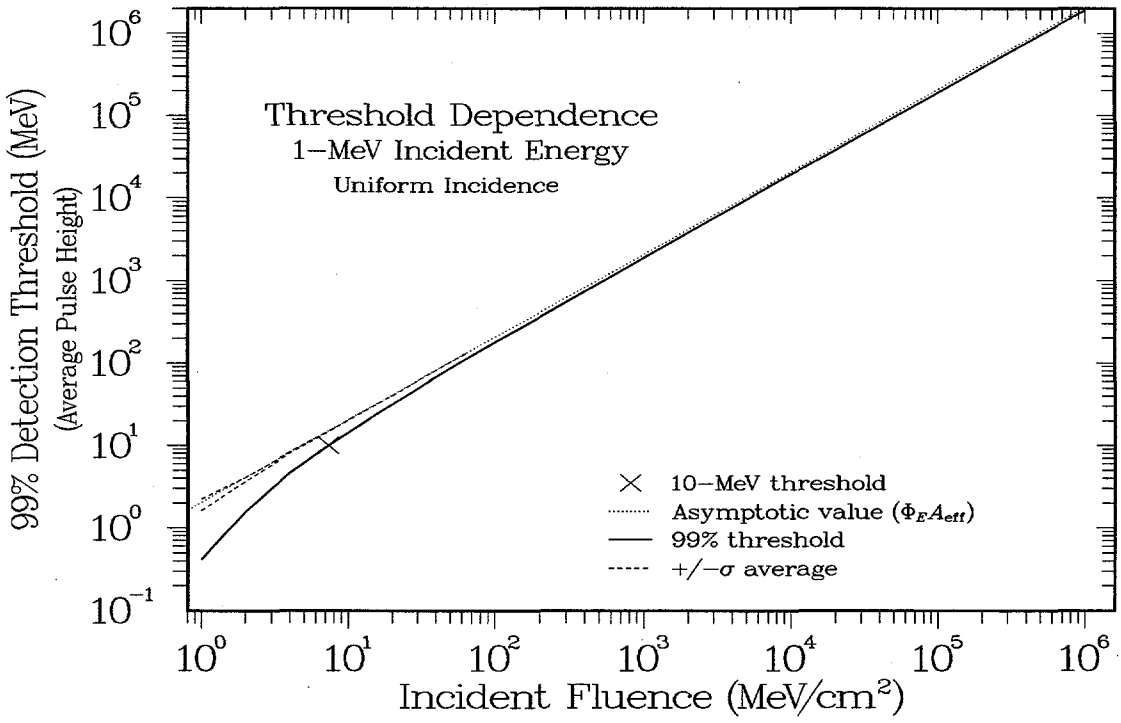

Figure 6.5. Dependence of the 99% threshold and average pulse heights from Figure 6.4 on increases in the instantaneous gamma-ray fluence.

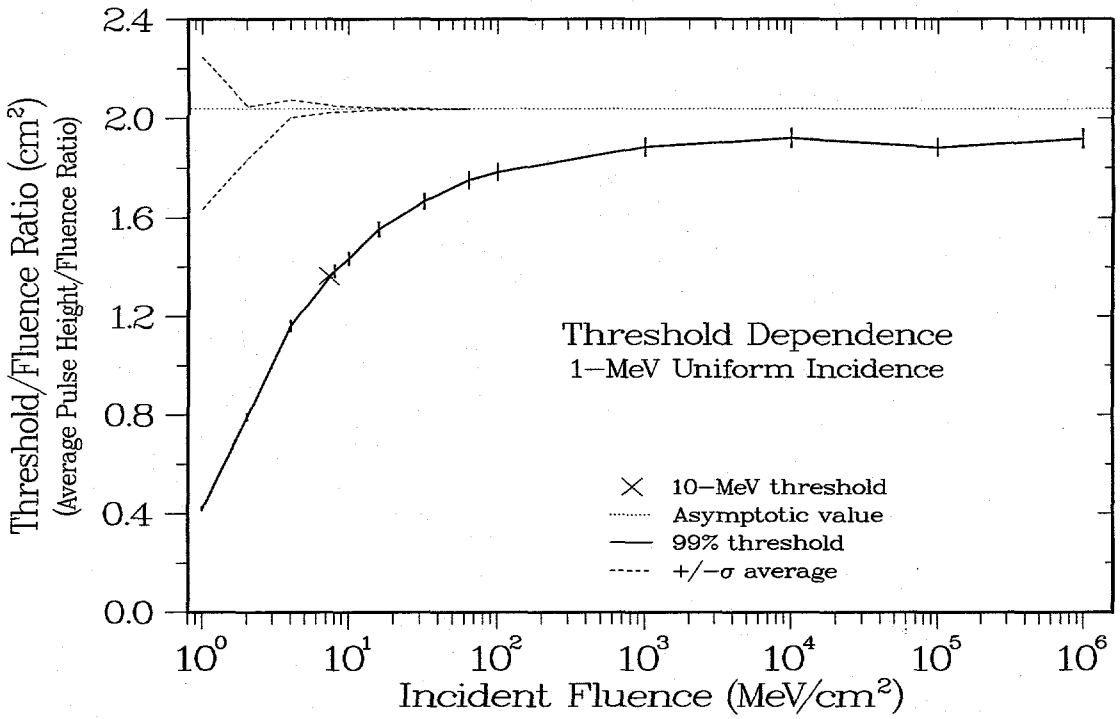

Figure 6.6. Ratio between the 99% threshold and the instantaneous fluences in Figure 6.5.

6.2. Energy Dependence

Pulse Heights and Thresholds. The analyses in Sec. 6.1 establish the technique for producing pulses composed of arbitrary numbers of incident gamma rays, but a monoenergetic pulse of isotropic photons is scarcely realistic. To investigate the effect of varying photon energies on the detector's threshold behavior, in this section we repeat the analysis for calculations with energy-bin boundaries at 0.1, 0.2, 0.5, 1, 2, 4, 8, and 12 MeV. The resulting pulse-height spectra are shown along with the corresponding Monte Carlo reproductions in **Figure 6.7**; each spectrum is simply an energy-broadened version of a Compton distribution. The threshold dependence for the collected set of energies is shown in **Figure 6.8** and in more detail in **Figure 6.9**. The divergence between the different curves at the lowest pulse heights varies with energy bin. The results for the highest incident energies correspond to the lowest number of photons and have the most curvature, while the curves for the lowest incident energies are almost straight lines. Depending on the energy bin chosen, the energy fluence that corresponds to a 10-MeV threshold level varies significantly, from 8 MeV/cm^2 for the 0.5–1.0-MeV bin to 17 and 30 MeV/cm^2 for the 0.2–0.5- and 0.1–0.2-MeV cases, respectively. As discussed for the previous 1.0-MeV results, these combinations of threshold and fluence values define the reliable operating range for the detector. Accordingly, in order to certify that the detector meets the requirement for a particular fluence threshold (in MeV/cm^2), we must know the energy distribution of the incident signal. This energy dependence enters partly through the statistical effect on the number of photons per unit energy and partly through changes in the detector's energy-dependent effective area. These two effects are seen separately in the ratios between the threshold and fluence values plotted in **Figure 6.10**. The statistical effect appears as the

reduction in the required threshold at low fluences, while the effective-area differences create the spread in the asymptotic values at high fluences. If we discount the very low values for the 0.1–0.2-MeV case, the asymptotic effective areas range from 1.4 to 2.0 cm^2, a result consistent with the four-rod effective areas of 6–8 cm^2 shown in Figure 4.5. Finally, we point out the additional values in Figure 6.10, one for 1.0 MeV (from Figure 6.6) and the other an evaporation energy spectrum. The latter values are used to represent the detector's "energy-averaged" response, just as the present use of uniform angle incidence represents an angle-averaged response. This assumption provides the basis for the calculations in the following section.

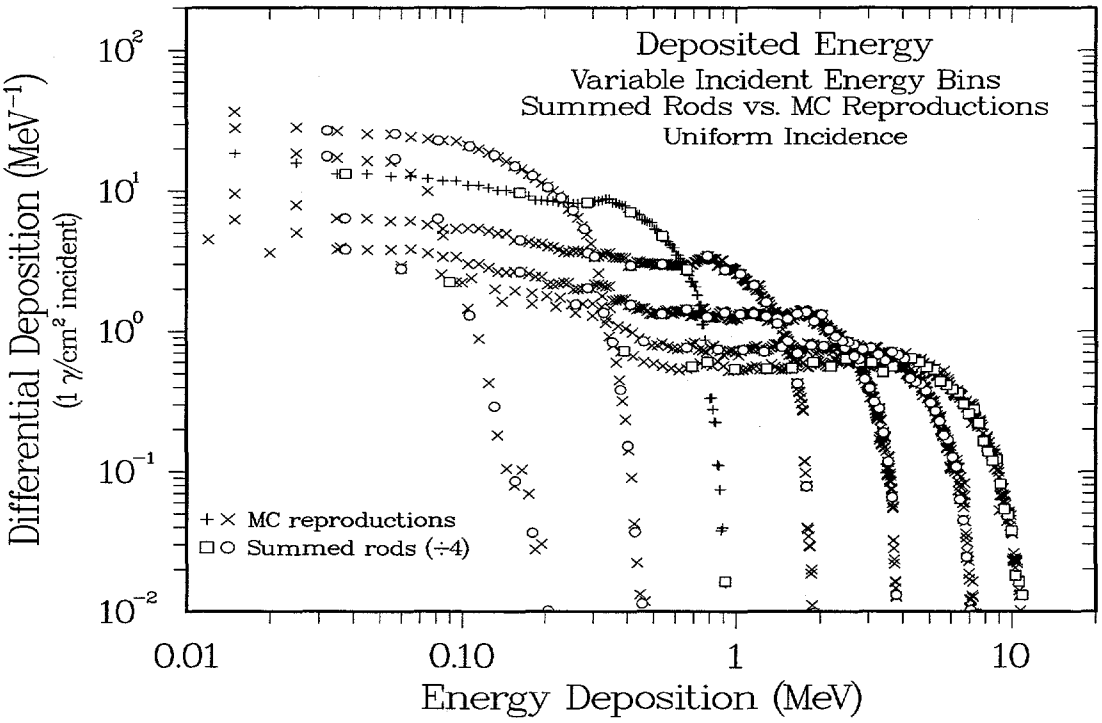

Figure 6.7. Generalization of the pulse-height distributions for 1-MeV gamma rays (Figure 6.2) to a set of distributions that covers the complete gamma-ray energy range from 0.1 to 12 MeV.

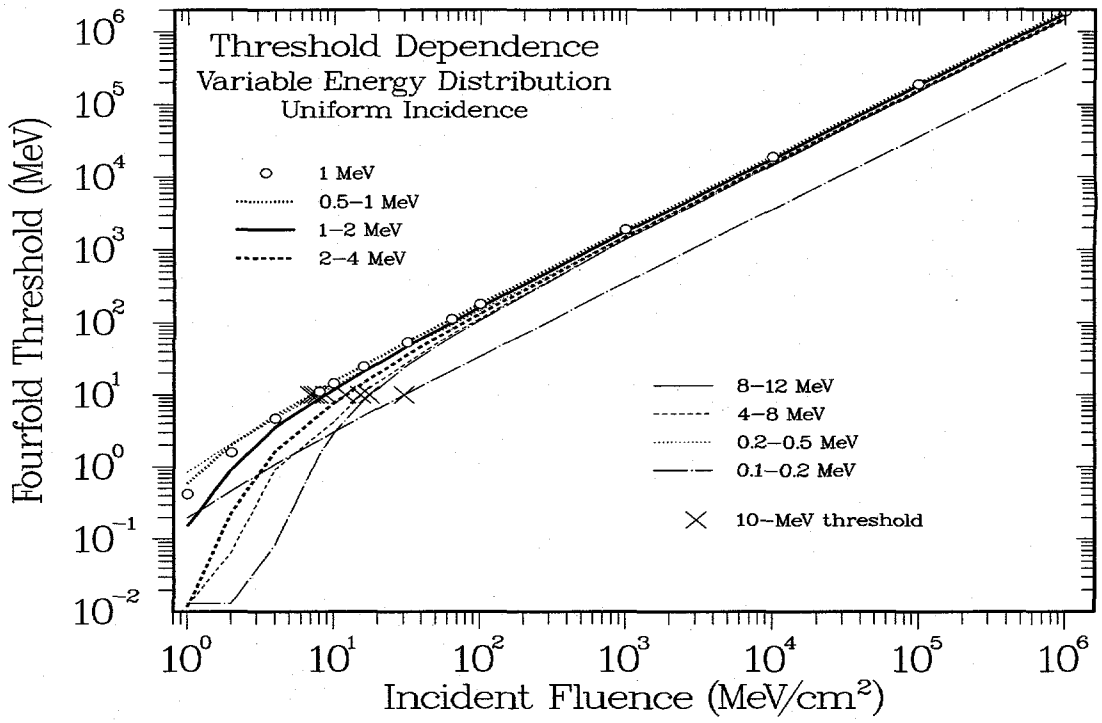

Figure 6.8. Threshold dependence as in Figure 6.5 for each of the energy distributions shown in Figure 6.7.

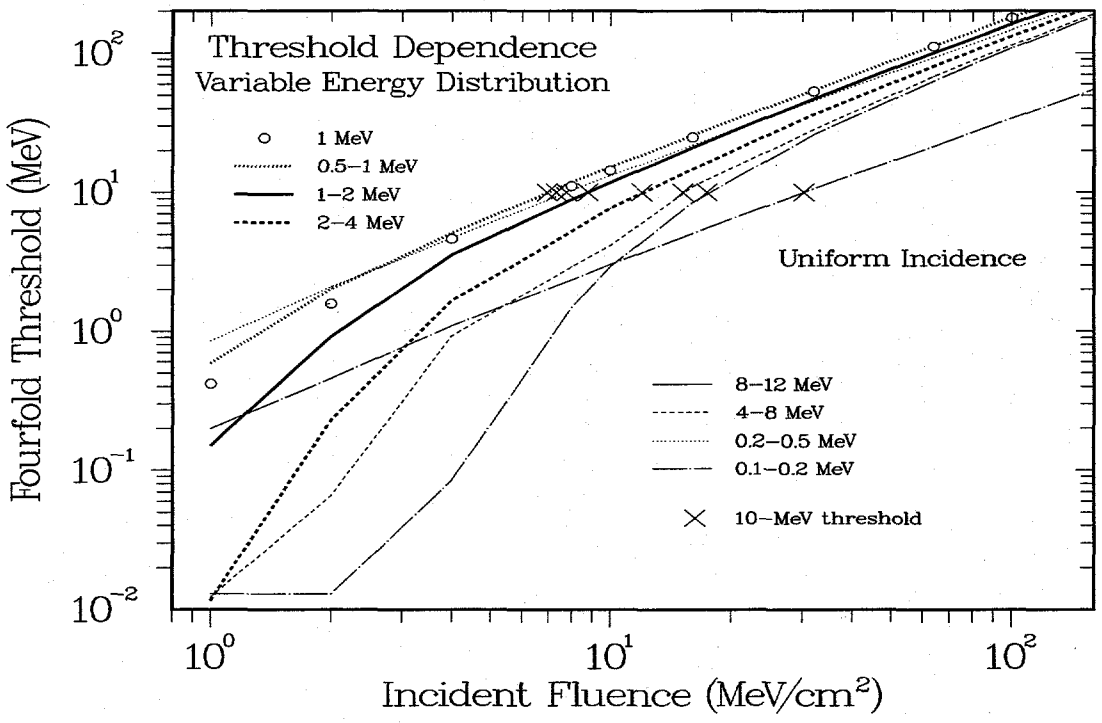

Figure 6.9. Enlargement of the low-fluence region of Figure 6.8.

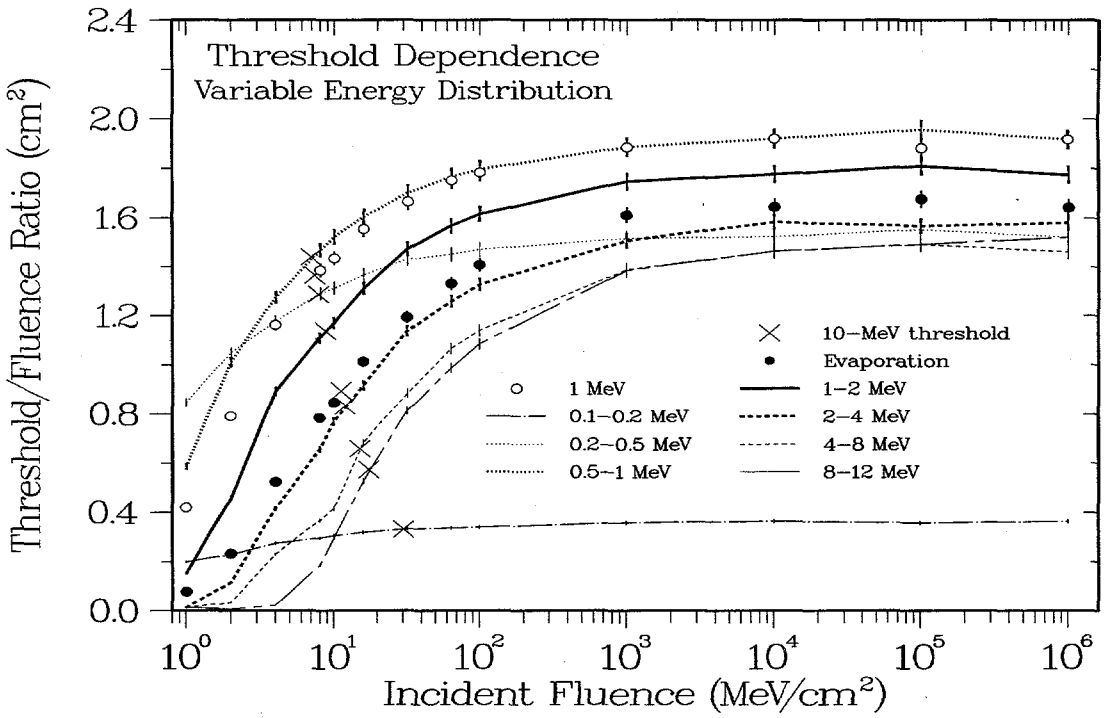

Figure 6.10. Ratios between the 99% thresholds and the instantaneous fluences in Figure 6.8.

6.3. Angle Dependence

Pulse-Height Spectra. Our studies of angular dependence require that we break the symmetry between the responses of the four separate scintillator rods. As in Figure 6.1, **Figure 6.11** shows the equality between the responses of the four-rod average and the individual-rod spectra for uniform incidence of the energy-averaged evaporation energy spectrum. In contrast, **Figure 6.12** shows the corresponding individual-rod spectra for the case of front-on incidence, that is, the 0° case from either the front-to-top or front-to-end rotations in Sec. 4.3 and 4.4. As shown by the computed effective areas, the overall detector responses for the angle-averaged and front-on cases agree within 5%, but the responses of the front and rear pairs of rods differ significantly, which can be expected to have some effect on the fourfold threshold levels. Finally, **Figure 6.13** compares the average and regenerated pulse-height spectra for front-on and end-on incidence. Although the front-on values are clearly larger at low pulse heights, it appears that the situation reverses at high pulse heights, with the end-on probabilities being slightly higher, as might be expected for the scintillator's orientation either normal or parallel to the source direction.

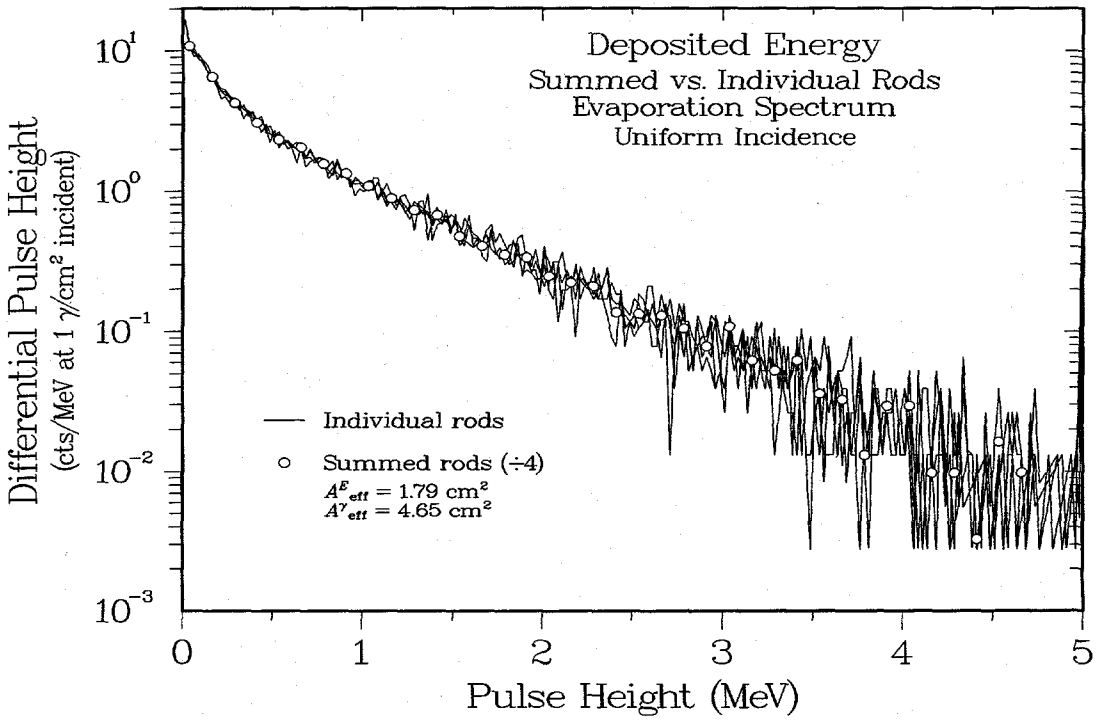

Figure 6.11. Individual-rod pulse-height distributions as in Figure 6.1, but for gamma rays with a continuous energy distribution incident uniformly from all directions.

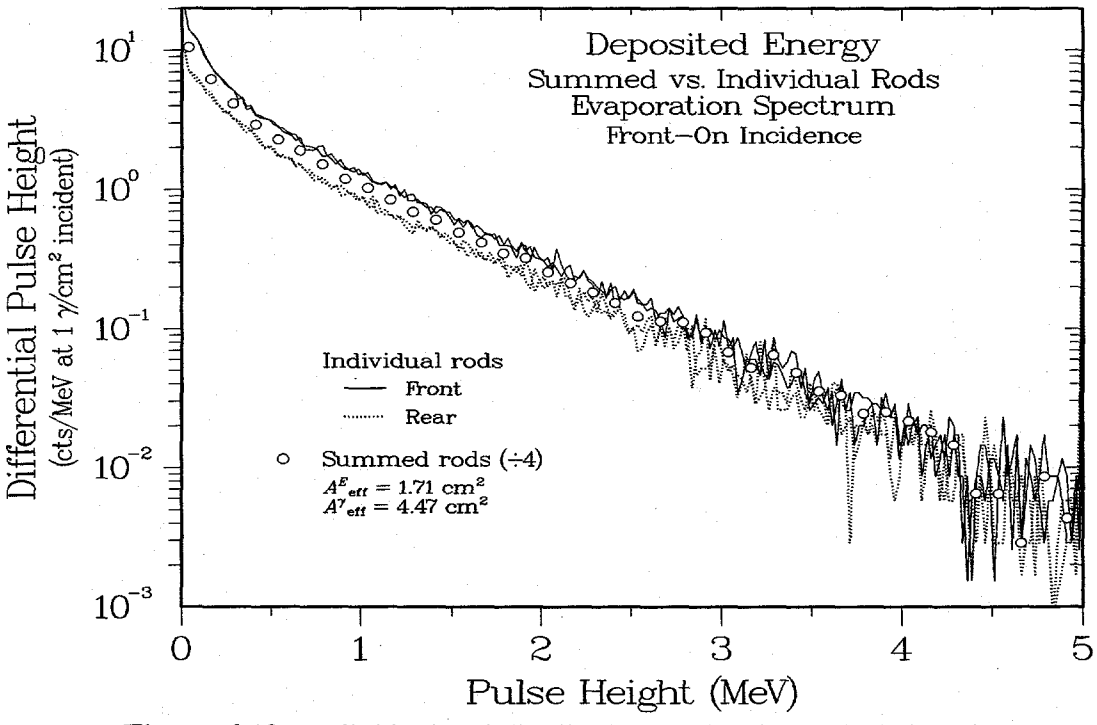

Figure 6.12. Individual-rod distributions as in Figure 6.11, but showing the difference between the front and rear pairs of rods for front-on incidence.

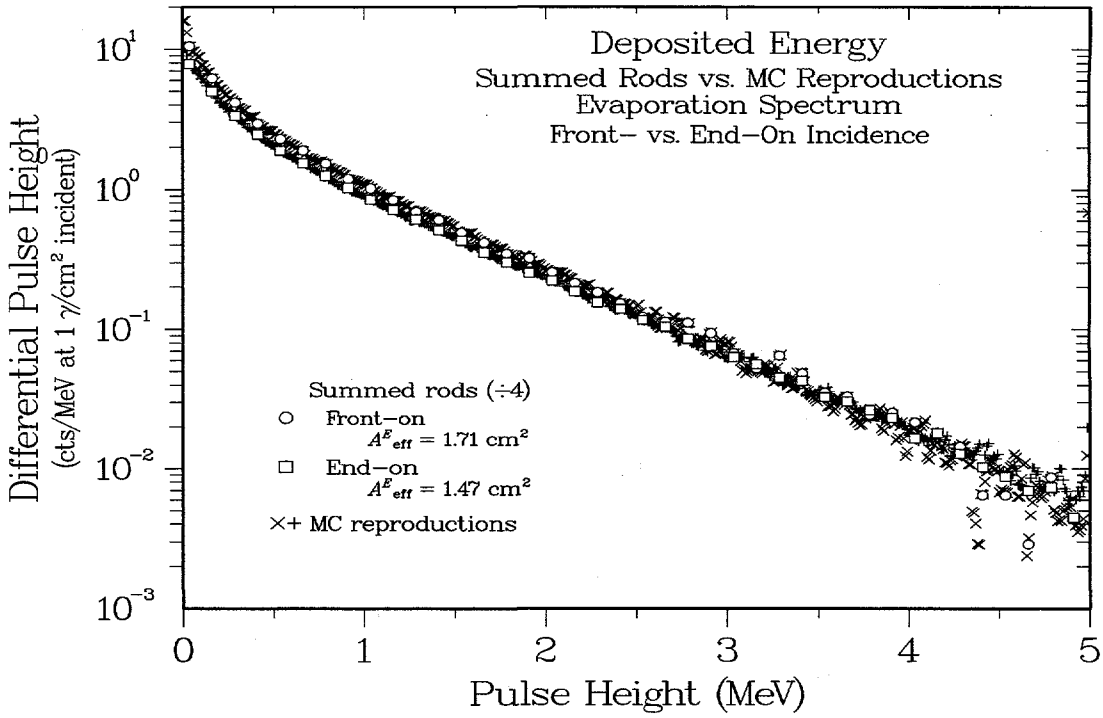

Figure 6.13. Pulse-height distributions as in Figure 6.11, but for gamma rays incident from either the front-on or end-on directions.

Threshold Values. The fourfold probabilities calculated from the summed pulse-height spectra are shown in **Figure 6.14**. There are slight differences in the shapes of the distributions at the lowest fluence values, but for higher values the results settle into a predictable pattern. The collected threshold values are shown in **Figure 6.15** and **Figure 6.16**. Because the 1.0-MeV effective areas are close to the maximum value, while the evaporation spectrum extends through a much higher energy range, the thresholds for uniform incidence are lower than those for the 1-MeV spectrum. Similarly, the lower effective areas of the front-on and end-on orientations also require lower threshold values. Note, however, that the differences between the responses of the four rods causes a deviation from the expected scaling of the asymptotic thresholds with average effective area. The lower pulse height for the rear rods in the front-on case carry through in the fourfold coincidence and drive the front-on thresholds to consistently lower values. Note also that the resulting 10-MeV operating points for difficult angular incidences range from 11 to 15 MeV/cm^2.

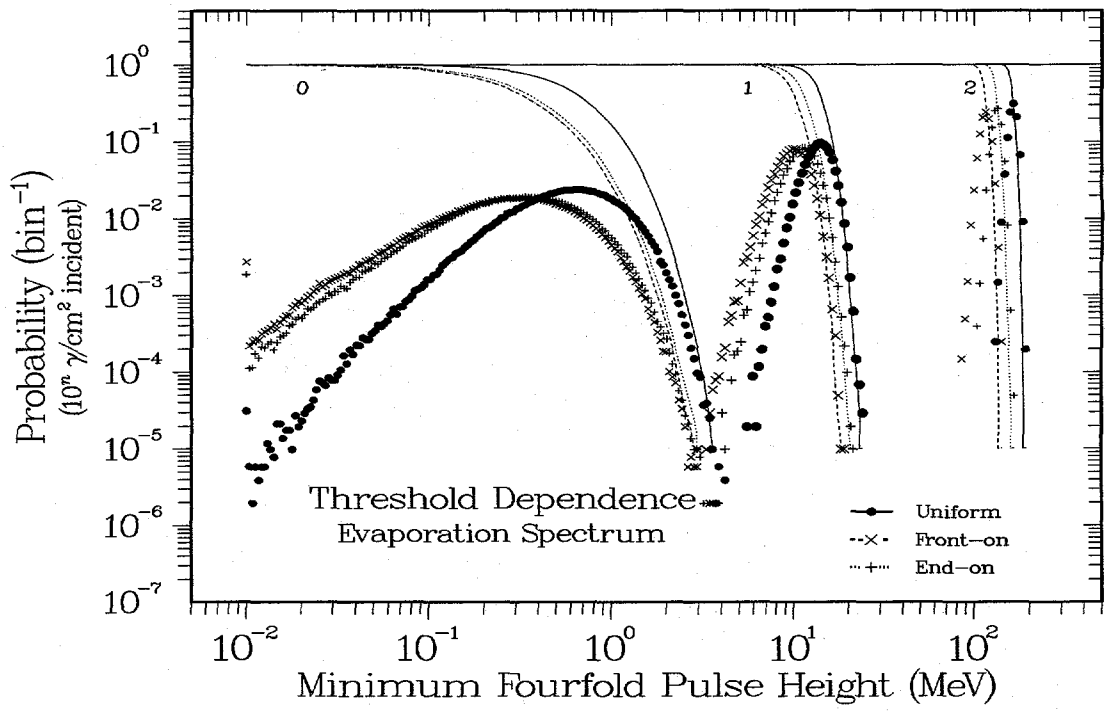

Figure 6.14. Threshold dependence for gamma rays with an evaporation energy spectrum and three different angular distributions.

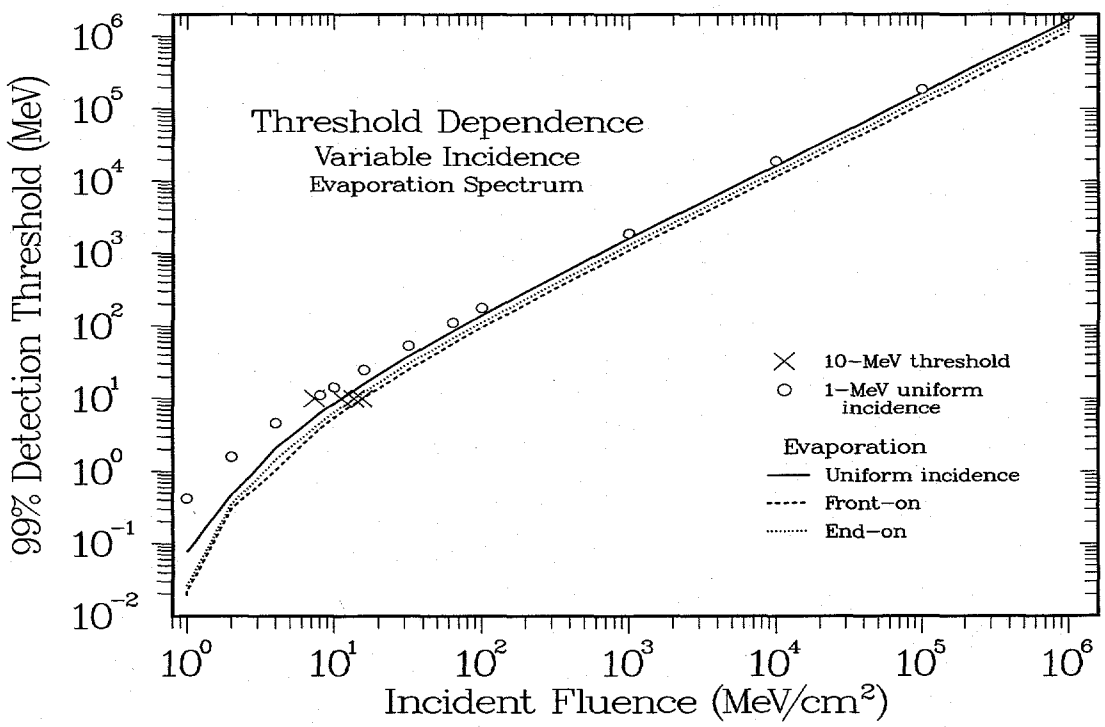

Figure 6.15. Comparison of threshold dependence for different angular incidences of the same evaporation energy spectrum.

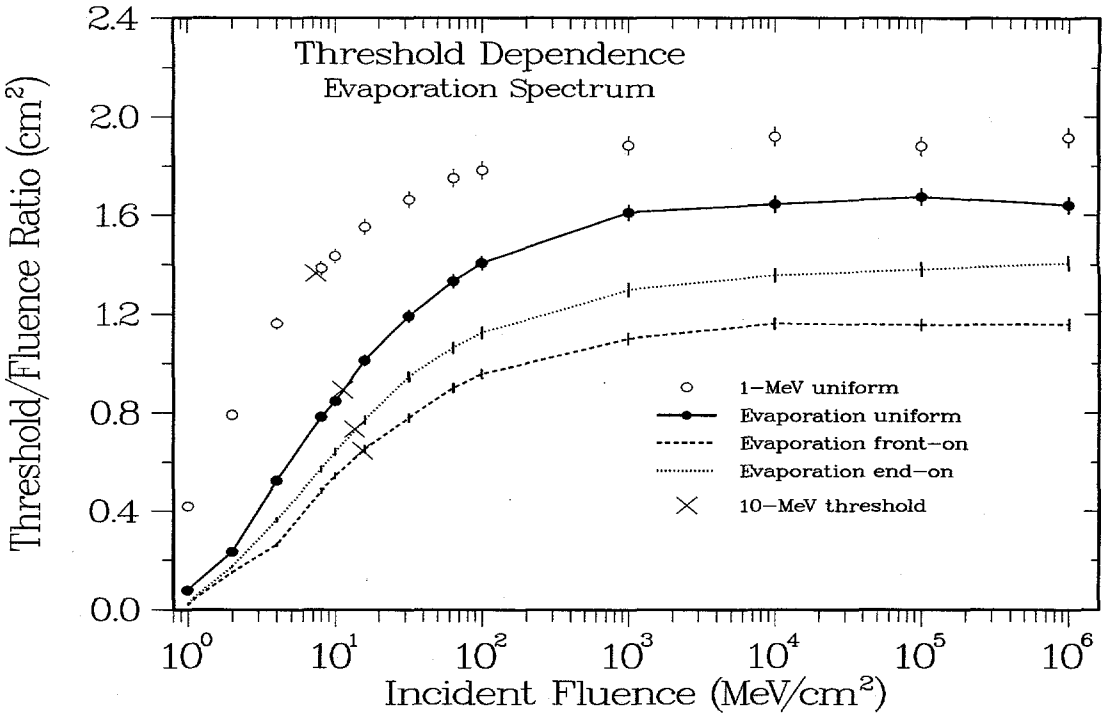

Figure 6.16. Ratio between the threshold and fluence values for different angular incidences.

6.4. Time Dependence

Approach. Just as statistical variations at low incident fluences determine the minimum pulse-height threshold, similar variations result in time jitter in the threshold crossings used to form the fourfold detector coincidence. The result is a minimum resolving time necessary to ensure that all four rods have crossed the threshold level. The approach for this time-width calculation is an extension of the pulse-height calculations used above. After sampling a pulse-height value from the calculated MCNP distribution, we use the result to increment a time histogram assuming a random distribution specified only by a generic FWHM (full width at half maximum) parameter. After accumulating such a histogram for each rod and then integrating over time (as expected in the electronics), we can determine both the earliest and latest crossing times for any particular threshold value. The difference between these two times then gives a time-jitter value expressed in FWHM units, and the accumulation of many such jitter values for repeated runs then gives a time-jitter distribution. For the case of an evaporation energy spectrum with uniform angular incidence, **Figure 6.17** shows integrals over a set of these distributions for our standard 10-MeV pulse-height threshold as a function of different incident gamma-ray energy fluences. At the lowest fluence of 8 MeV/cm^2, less than 70% of the incident pulses ever cross all four thresholds, but at 16 MeV/cm^2 more than 90% cross the threshold within a time window whose width is less than 50% of a FWHM unit. As the fluence increases, the required resolving time becomes gradually shorter. Above fluences of 256 MeV/cm^2, a detection probability of almost 99% can be reached with a window width of only 0.2 FWHM.

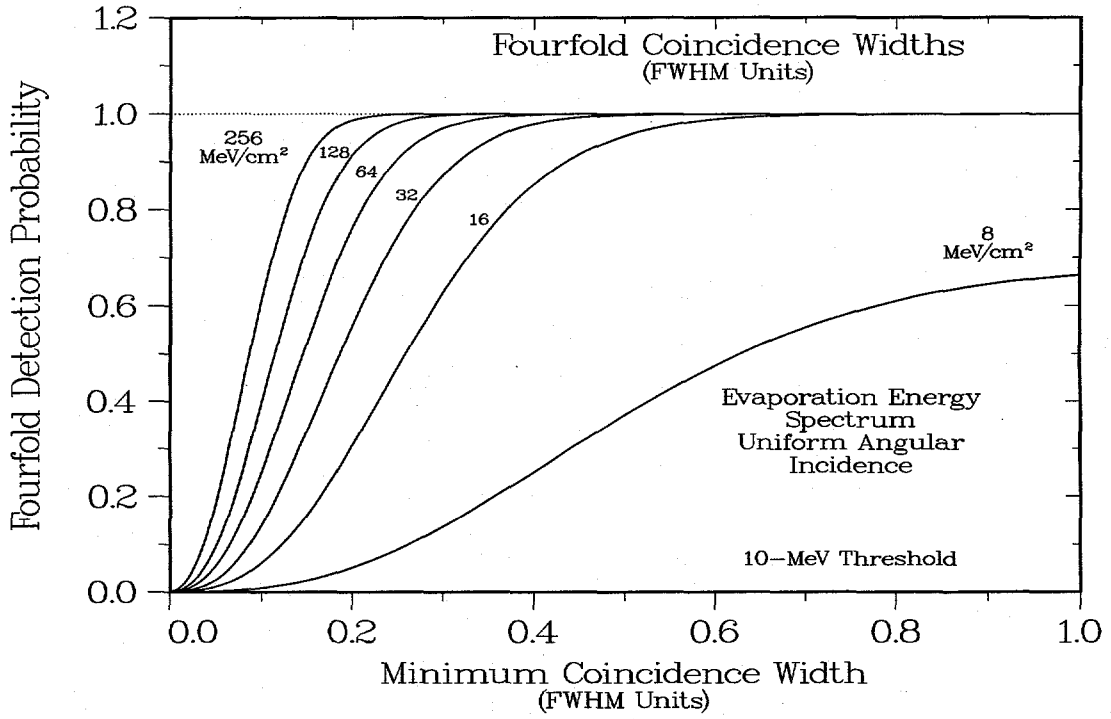

Figure 6.17. Statistical probabilities of meeting a fourfold coincidence requirement at different values of resolving time and incident energy fluence.

Timing Results. The timing calculations can be repeated at different values of incident fluence and pulse-height threshold to map out the range of coincidence widths needed to guarantee a 99% probability of event detection. **Figure 6.18** shows that the resulting threshold dependences behave differently at low and high incident energy fluences. At low fluences, the threshold crossing is relatively far up on the integrated signal. In this case the timing jitter is dominated by the relative error in the number of pulses required to reach the specified pulse-height level, which decreases as the threshold is raised. Thus, at fluences below 20 MeV/cm^2 the timing jitter increases as the threshold is decreased because fewer incident gamma rays contribute to the pulse-height sum. As the fluence increases, we might therefore expect that the timing jitter would gradually decrease to zero, but this result is not seen in the calculations. Instead, at larger fluences the threshold is reached at earlier times, that is, further out on the tail of the rising signal, so the statistical uncertainty remains high. Accordingly, at high fluences lowering the threshold increases the jitter by rapidly moving the crossing point to earlier times. In short, at low fluences the timing resolution is dominated by pulse-to-pulse statistical variations, but at high fluences the limit is the intrinsic width of the incident signal. The time jitter determines the minimum coincidence resolving time, which affects the measurement dead time and the random coincidence rate, so the optimum selection of operating parameters requires careful consideration of the relationship between pulse-height threshold and fluence level. Depending on the exact details of the signal time dependence, our recommended pulse-height threshold of 10 MeV suggests a minimum operating point at fluence levels of 15–20 MeV/cm^2.

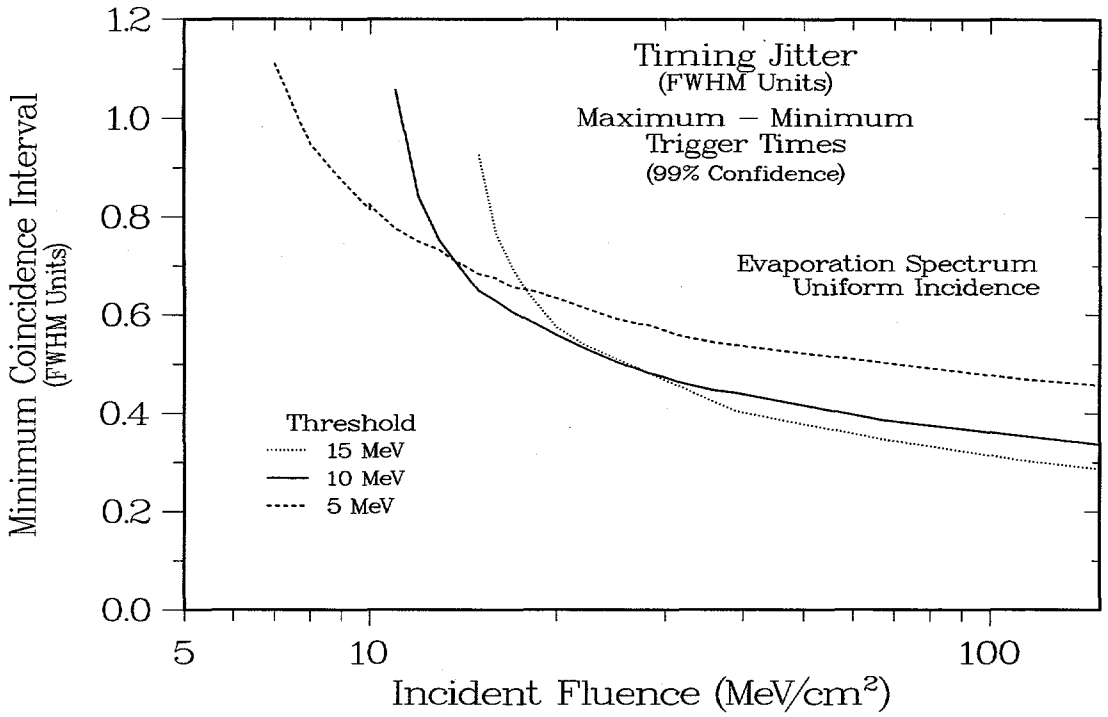

Figure 6.18. Timing jitter as a function of pulse-height threshold and incident energy fluence.

6.5. Uncertainties

Energy and Angle Variations. The discussion in the previous section focused on the effect of variations in energy and angle of the relation between incident fluence and summed pulse-height threshold. Of course, these variations have similar effects across the detector's entire dynamic range, not just at threshold. These effects are best illustrated by showing the variation in the widths (standard deviations) of the summed pulse-height distributions like those for the 1-MeV case shown in Figure 6.3. **Figure 6.19** shows the uncertainties for different incident directions, and **Figure 6.20** shows the uncertainties for several of the different energy distributions. As in our discussion of Figure 6.10, we point out that systematic uncertainties dominate at high incident fluences, while statistical uncertainties become increasingly important at low fluences, with values over 20% at energy fluences below 2 MeV/cm^2. Similar effects are seen for the energy variations in Figure 6.20. Thus, because of these fundamental variations in effective area, at even the highest fluences the SPG measurements will carry uncertainties of at least 20% unless the source directions or energy distributions can be determined, and these systematic uncertainties can be increased by an additional 20% from the low-fluence statistical variations. That is, the measured amplitude for any single pulse at these fluence levels can easily differ by 40% from the true value because of fundamental signal and detector issues. Note, however, that the proposed background-rejection threshold at 10 MeV suggests a minimum energy-fluence threshold of about 10–20 MeV/cm^2, a point at which the statistical uncertainties are negligible compared with the systematic ones. Thus, depending on the eventual choice of operating parameters, the ultimate performance of the system may be better or worse than the limits given here. If, for example, the incident direction or energy spectrum of the signal is measured elsewhere, the uncertainties are reduced. Similarly, if additional sources of error are discovered, the uncertainties may increase.

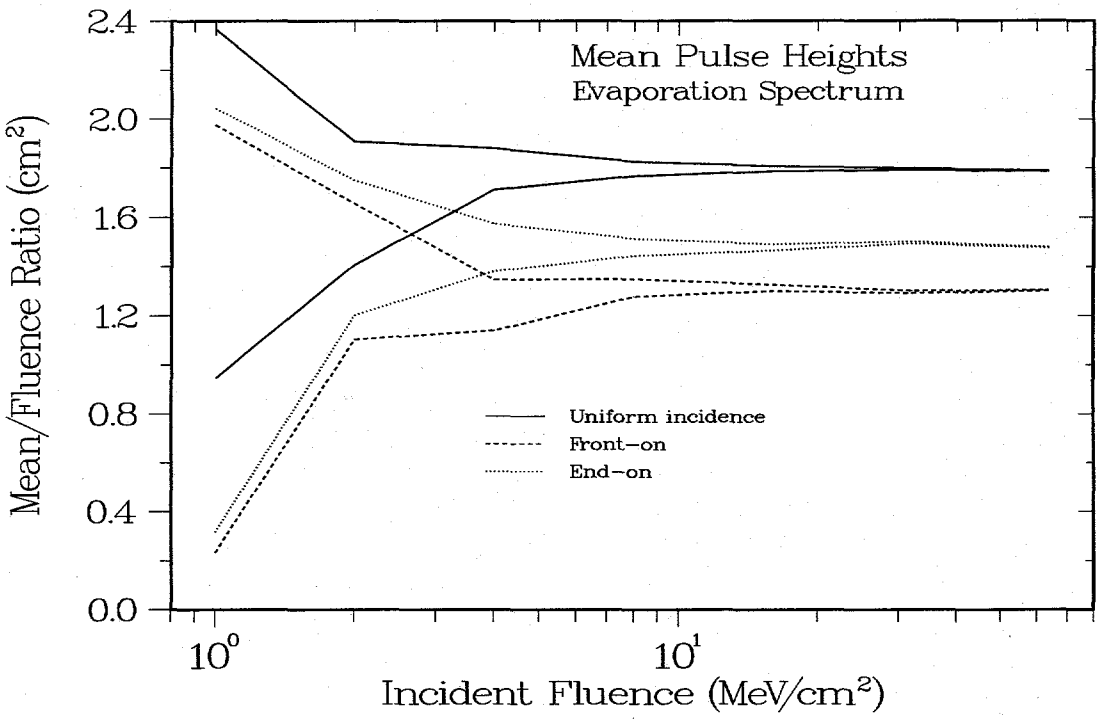

Figure 6.19. Uncertainty in the pulse-height determination for different directions of the incident fluence.

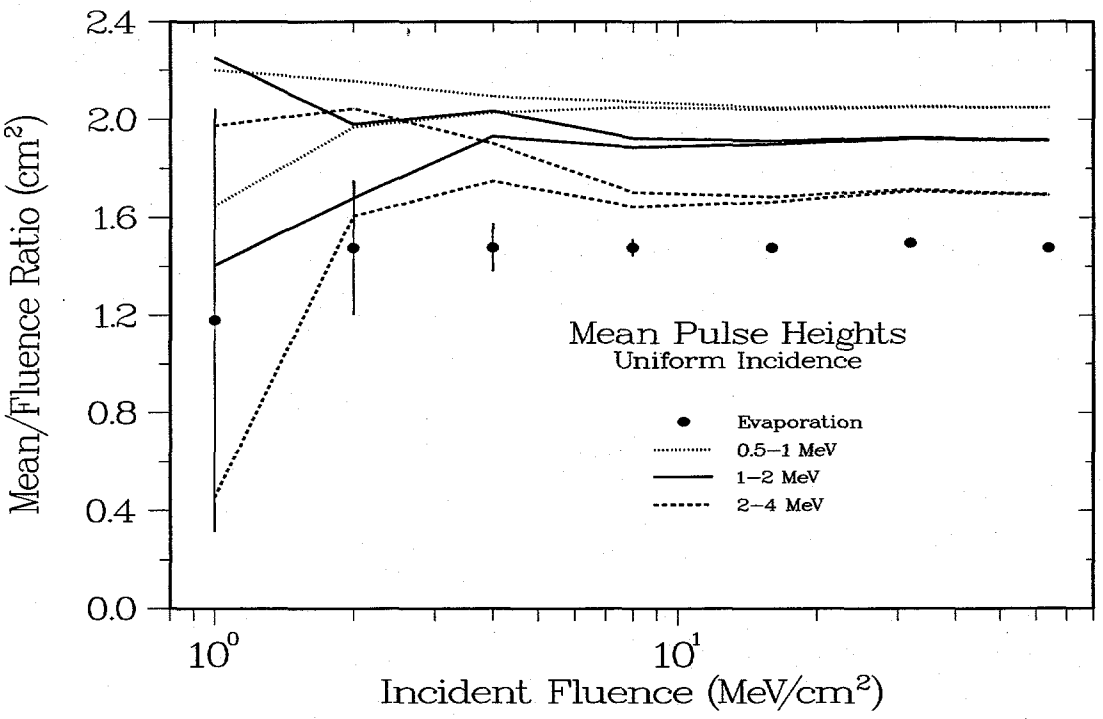

Figure 6.20. As in Figure 6.19, but for the uncertainty contribution from differences in incident energy distributions.

Geometry Variations. Our final calculations in this chapter concern changes in detector geometry rather than source characteristics. In particular, how might changes in system

size or weight limitations affect our performance estimates for the BC400 scintillators? **Figure 6.21** compares effective-area calculations for the standard 1″ diameter by 6″ long scintillators (see Figure 4.4) with those for shorter rods with the same volume or lengthwise area. In the standard calculations, the voids in the polyethylene at the ends of the photomultiplier tubes were left empty; in the added calculations, as the rods decrease in length these voids are filled with polyethylene plugs to increase the neutron moderation. If such plugs had been used for the standard case, the results would probably be closer to those for the two 1.25″ cases. The observed energy dependences for the modified geometries are much the same as for the standard case, and a 25% change in the aspect ratio does not cause a large change in the effective area. Comparing the constant-area and constant-volume results indicates that increasing the detector area (and hence volume) always increases the effective area, but increasing the detector volume tends to decrease the effective area. The detailed dependences for an evaporation spectrum are summarized in **Figure 6.22**, which shows the effective areas for different rod diameters in both the constant-area and constant-volume cases. As before, the plotted points are pulse-height tallies, and the curves are heating tallies. These results indicate that effective area scales essentially with rod volume, although shorter rods have slightly lower efficiencies because of attenuation in the surrounding polyethylene. Finally, **Figure 6.23** shows the effect of geometry on the fluence dependence of the fourfold pulse-height threshold. The values for the standard case are from Figure 6.15; the other curves show the corresponding calculations for the alternative geometries. To maintain the same fluence sensitivity, decreasing the rod length requires increasing the diameter, which in turn requires increasing the pulse-height threshold by a corresponding amount to provide equivalent comicray rejection. Within the uncertainties in the calculations, all parameter combinations within the small ellipse should have slowly varying performance characteristics.

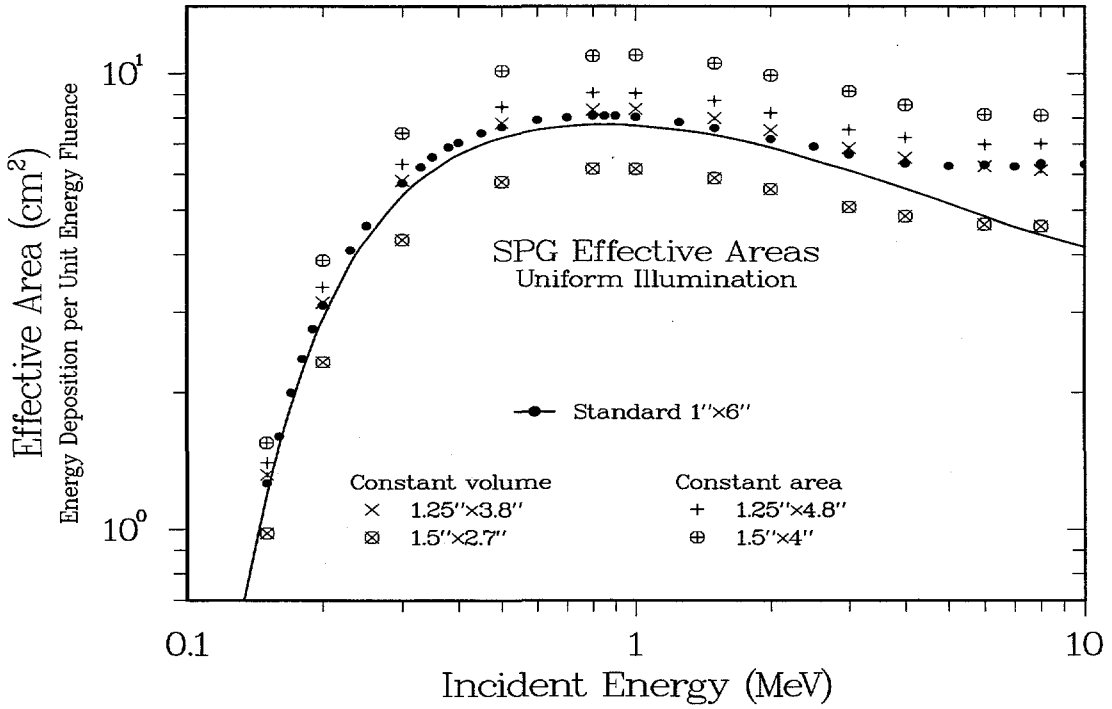

Figure 6.21. Energy-dependent effective areas for scintillator rods with different combinations of lengths and diameters.

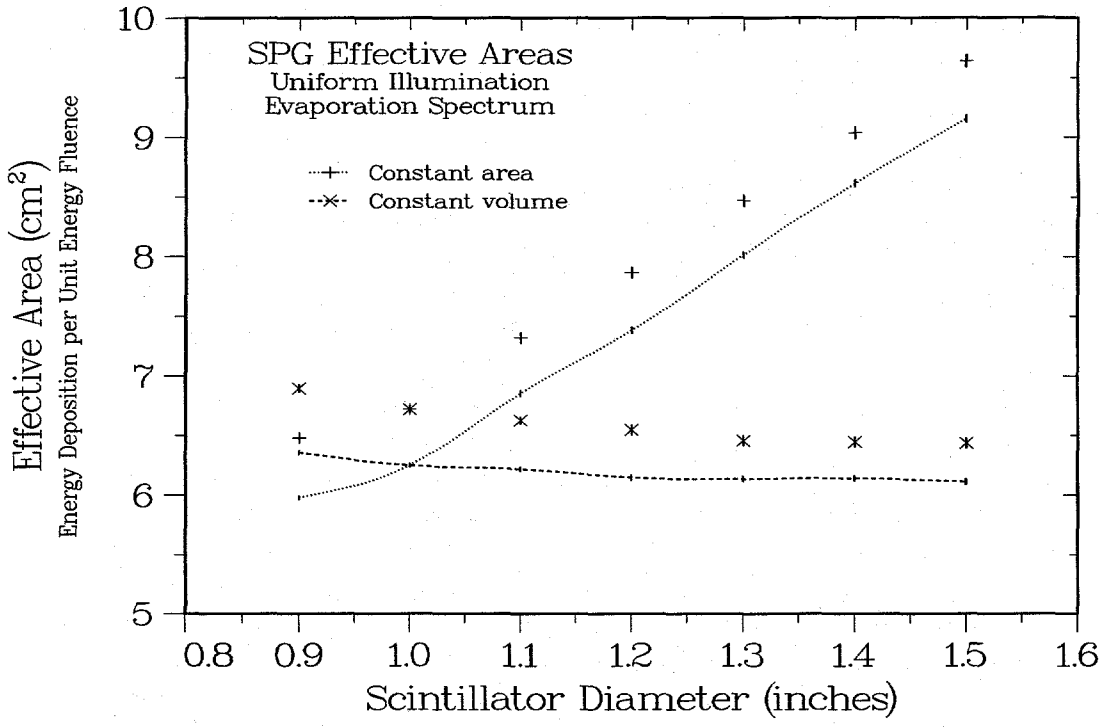

Figure 6.22. Variation of effective area versus rod diameter for uniform illumination with an incident evaporation energy spectrum.

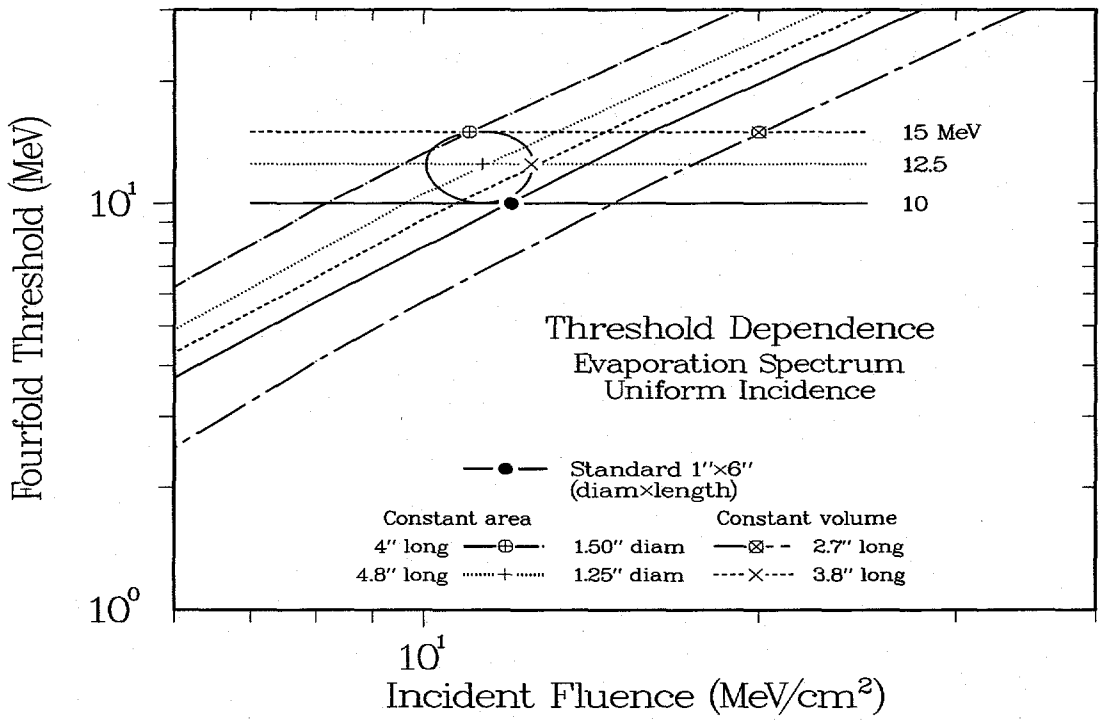

Figure 6.23. Dependence of pulse-height threshold on incident fluence for different combinations of scintillator rod diameter and length.

6.6. Discussion

Results. The important issues in this chapter fall into three categories:

(1) *Monte Carlo Technique.* The problem of statistical granularity in threshold response is common to all detectors for energetic photons at gamma-ray energies, because the energy deposition produced by a few incident photons can be large enough to trigger an electronic pulse-height threshold. Thus, the calculational approach developed in this chapter for the SPG detector can be similarly applied to other instruments such the APG and XDS instruments. Of particular significance is the technique's starting point, a pulse-height spectrum, which can be easily measured or calculated for many different systems.

(2) *Operating Thresholds.* In the present case, the major outcome of the analysis has been the connections between incident fluences, pulse-height thresholds, and timing resolutions for a variety of different source and detector assumptions. Raising the pulse-height threshold lowers the background rate at the expense of decreasing the incident fluence sensitivity, although the effect of threshold on resolving time is more complex. If we combine all the effects of timing resolution and cosmic-ray backgrounds, the results suggest energy-fluence thresholds in the range of 10–20 MeV/cm^2.

(3) *Statistical versus Systematic Uncertainties.* The variations in source and detector assumptions also lead to a set of constraints on the instrument's overall accuracy. If the instrument is operated at pulse-height thresholds well below the 10-MeV value suggested for cosmic-ray rejection, the statistical uncertainty caused by the granularity in the detected fluence becomes a significant issue. Even at the highest fluences, however, variations in the detector's effective area as functions of angle and energy may inevitably cause 20% uncertainties in the measured fluence values. Similar behavior is seen in the dependence of timing resolution on pulse-height threshold.

7. SAN DETECTOR RESPONSE

Overview. The SPG effective areas, angular determinations, and pulse responses in Chaps. 4, 5, and 6 have their equivalents in the corresponding analyses for the SAN detector. However, because gamma-ray measurements are not the central mission of the SAN instrument, we will review these analyses only briefly in this report. In Sec. 7.1 we present the calculated effective areas as functions of energy and angle, and we compare the results with those for the ^{3}He test setup from Chap. 2. These effective areas provide the basis for evaluating the gamma-ray charge sensitivity of the counters, which can be used to evaluate the feasibility of using current measurements to extend the detector's neutron pulse-counting range. We do not attempt to develop any SAN angle-determination capabilities, because the analyzing powers are strongly energy-dependent and very low at the energies of interest. It is, however, important to evaluate the effect of gamma-ray pulse pileup in order to determine the energy-fluence threshold, so in Sec. 7.2 we repeat the Monte Carlo analysis developed above for the SPG detector.

7.1. SAN Effective Areas

Uniform Incidence. We begin by presenting in **Figure 7.1** the effective areas for the sum of the energy depositions in the two high-sensitivity ^{3}He tubes. These results should be compared with those for the test setup shown in Figure 2.8. The MCNP heating calculations for the bare and fully shielded detectors are shown by the two curves, and the corresponding MCNP4A pulse-height calculations are shown by the open and solid circles. As before, at low energies the MCNP values for the bare ^{3}He gas closely follow the photoelectric absorption, but near 10 keV the effect of secondary electrons causes a slight increase in the energy deposition. At 100 keV these electrons begin to punch out of the gas volume, and the fraction of the incident energy deposited in the detector begins to decrease gradually. By 10 MeV the pulse-height effective area is an order of magnitude lower than the heating value. Adding the SS and CH_2 shielding, however, has the same effect as in the ^{3}He test setup: the low-energy effective areas are cut off at about 30 keV by the SS attenuation, and the high-energy areas rise to approximately match the heating prediction. The calculations for the full SAN instrument follow the setup results by showing an increase in the effective area around incident energies of 100 keV. Also shown in the figure are the corresponding calculations made with the more recent MCNP4B code and the same cross-section libraries. For the corresponding SPG test in Figure 4.4, there were no apparent differences between the 4A and 4B results. For the SAN detector, however, the differences are as large as a factor of 5. Although the MCNP4B documentation[9] alludes to changes that include "enhanced photon physics," we do not have enough information to determine the origin of the observed difference. (Note: Subsequent discussions with the authors of the MCNP codes indicate that changes were made in the photoelectron energy distributions.) As shown below, however, even the large differences in Figure 7.1 do not significantly affect the conclusions from the present analysis.

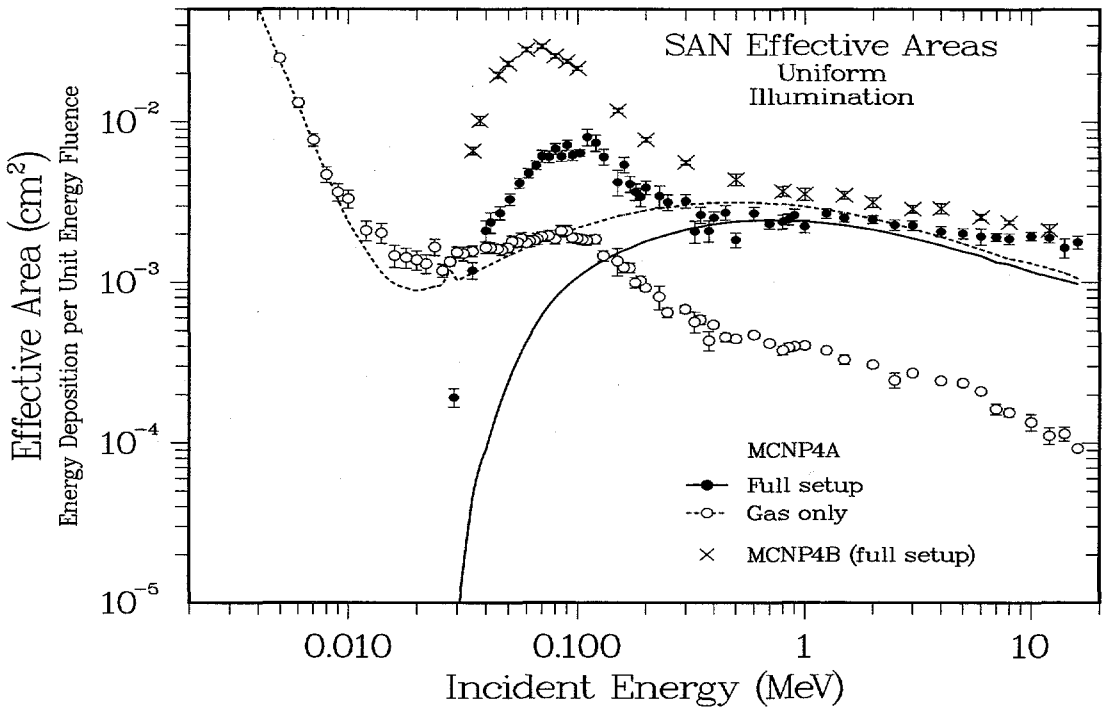

Figure 7.1. Energy dependence of the effective areas of the bare and fully shielded SAN ^{3}He tubes calculated for uniform illumination using two different versions of the MCNP code. The curves show heating tallies; the symbols show pulse-height values.

Angle-Dependent Effective Areas for Bare and Shielded ^{3}He Counters. In the process of carrying out the SPG calculations in Chap. 4, additional tallies were used to accumulate energy depositions for the two ^{3}He tubes. **Figure 7.2** shows pulse-height and heating calculations for both the 0° (front) and 90° (top) illuminations of the bare ^{3}He tube. As expected, the MCNP values are essentially the same at both angles, and their departure from the heating predictions follows the corresponding angle-averaged results in Figure 7.1. **Figure 7.3** shows the effect of including the SS walls in the front-to-top calculations. As before, the shielding introduces a low-energy cutoff, and at high energies the attendant electron production greatly increases the energy deposited in the gas, resulting in effective areas that match the heating predictions almost exactly. The enhanced response around 100 keV is particularly obvious. **Figure 7.4** and **Figure 7.5** present the front-to-top and front-to-end calculations for the fully shielded detector. As expected, adding the CH_2 layer has little effect on the response, except perhaps in the 100-keV region. Finally, in Figure 7.5 there appears to be a consistent difference between the front (0°) and end (90°) responses at high energies. Examining the angular dependence in more detail in **Figure 7.6**, however, suggests that any difference is far from statistically significant.

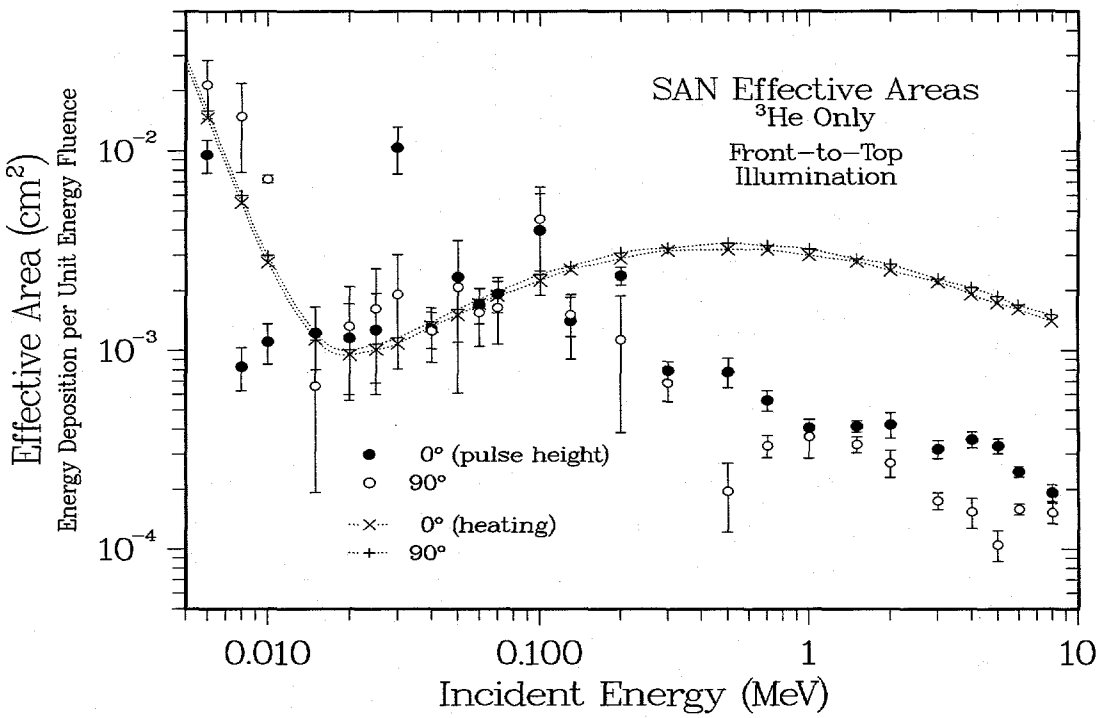

Figure 7.2. Effective areas for two extreme cases of front-to-top illumination of the two bare high-sensitivity SAN ^{3}He tubes. (Compare with the results for the bare ^{3}He case using the test setup in Figure 2.8.)

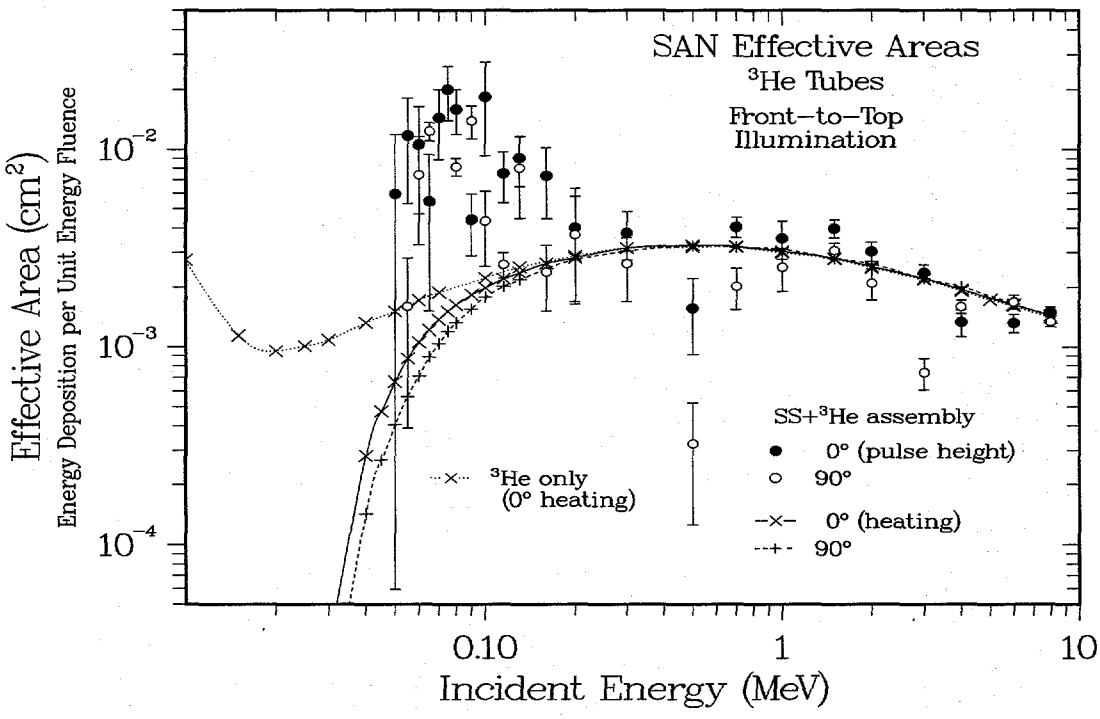

Figure 7.3. Effect of adding SS tube walls to the calculations in Figure 7.2 for bare ^{3}He tubes.

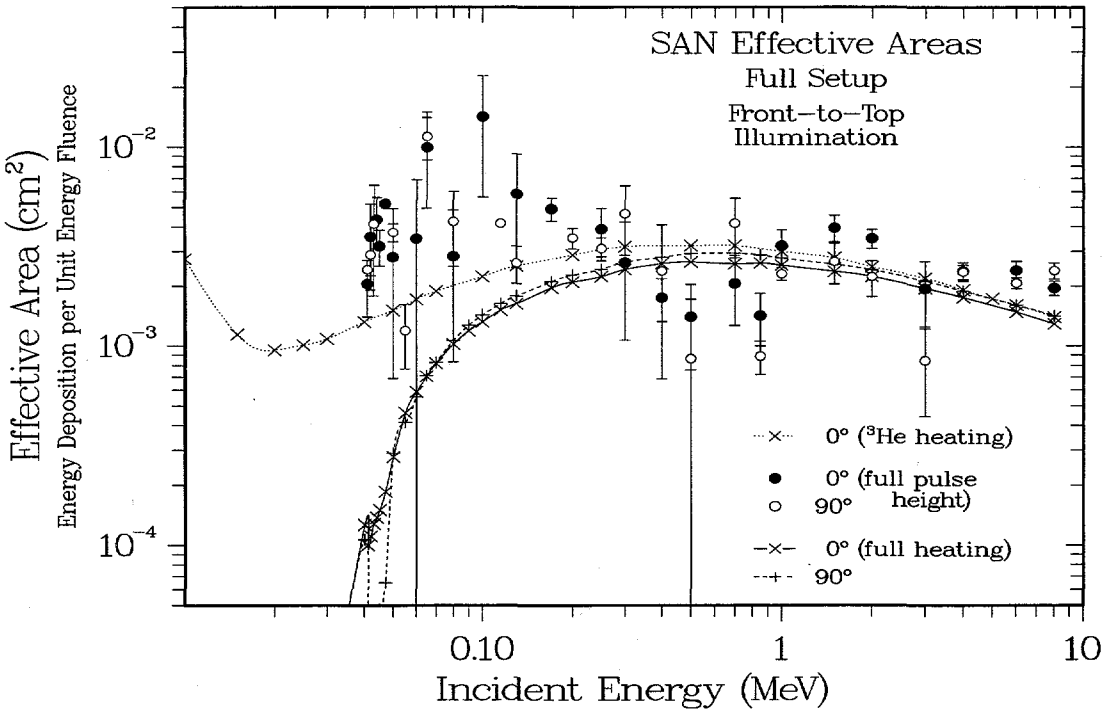

Figure 7.4. Effective areas for front-to-top illumination as in Figure 7.2, but the fully shielded SAN detector.

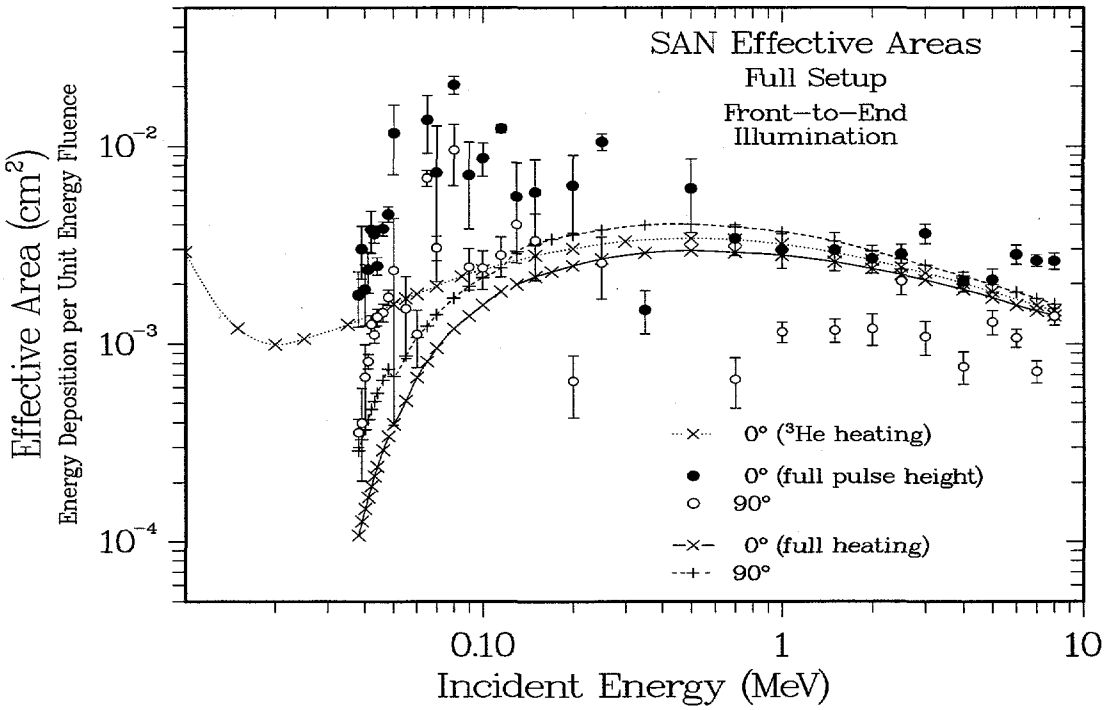

Figure 7.5. Fully shielded effective areas as in Figure 7.4, but for particular angles from the front-to-end calculations.

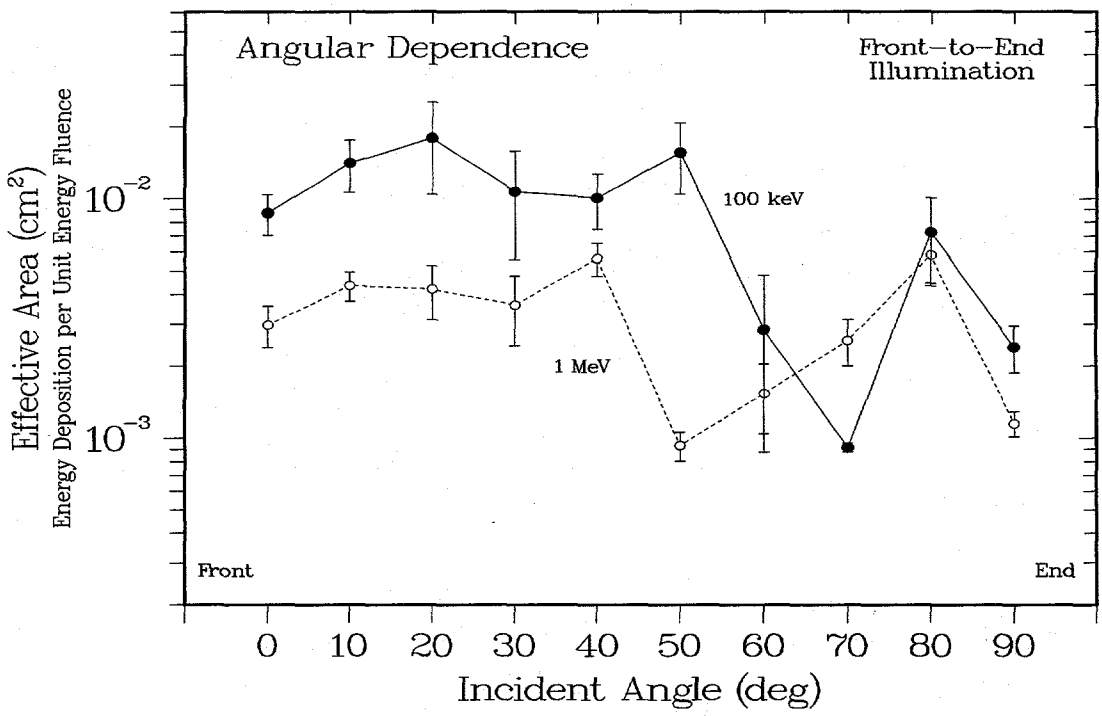

Figure 7.6. Lack of significant angular dependence in the effective areas for the fully shielded SAN detector at two different energies.

7.2. Pulse Response

Pulse-Height Spectra. The energy- and angle-averaged pulse-height distributions calculated by MCNP4A and MCNP4B for the summed and individual ^{3}He tubes in the SAN detector are shown in **Figure 7.7**. In both cases most of the pulses are only a few keV, although the codes differ slightly in their predictions for the long tail that extends upward to energies above 50 keV. This difference results in a systematic offset between the accumulated pulse-height spectra at different incident fluence levels, which are shown in **Figure 7.8**. Note here that no coincidence requirement is imposed, so the distributions shown are for single tubes. Also note that our interest is in ensuring rejection, not detection, of the incident gamma-ray pulse, so the probability integrals shown in the figure increase instead of decrease as the pulse-height threshold is raised. For reference, the pulse-height threshold for the ^{3}He counters is not determined by the cosmic-ray background, but by the minimum energy for a recoil triton from the $^3\text{He} + \text{n} \rightarrow {}^3\text{H} + \text{p}$ capture reaction. The dotted lines in Figure 7.8 indicate that this minimum pulse height of 191 keV corresponds to an incident fluence of about 60 MeV/cm^2. Thus, a plateau setting of about 150 keV would be sufficient to reject all of the gamma pulses at a fluence level of 10 MeV/cm^2, but it would probably be exceeded by every pulse at the level of 10^2 MeV/cm^2. These results are shown in more detail in the full fluence-threshold plot in **Figure 7.9**. According to this figure, the probability of leakage across a 191-keV pulse-height threshold reaches 1% at an incident gamma-ray fluence of about 55 MeV/cm^2.

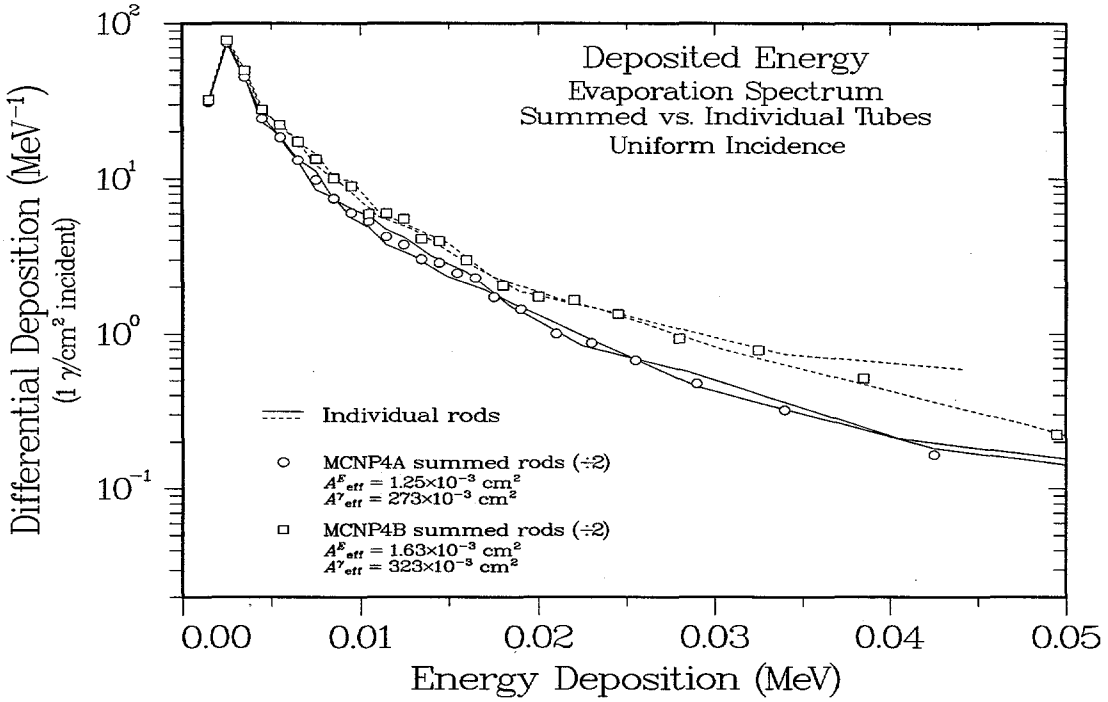

Figure 7.7. Calculated pulse-height response of a fully shielded ^{3}He counter to a continuous spectrum of gamma rays incident uniformly from all directions.

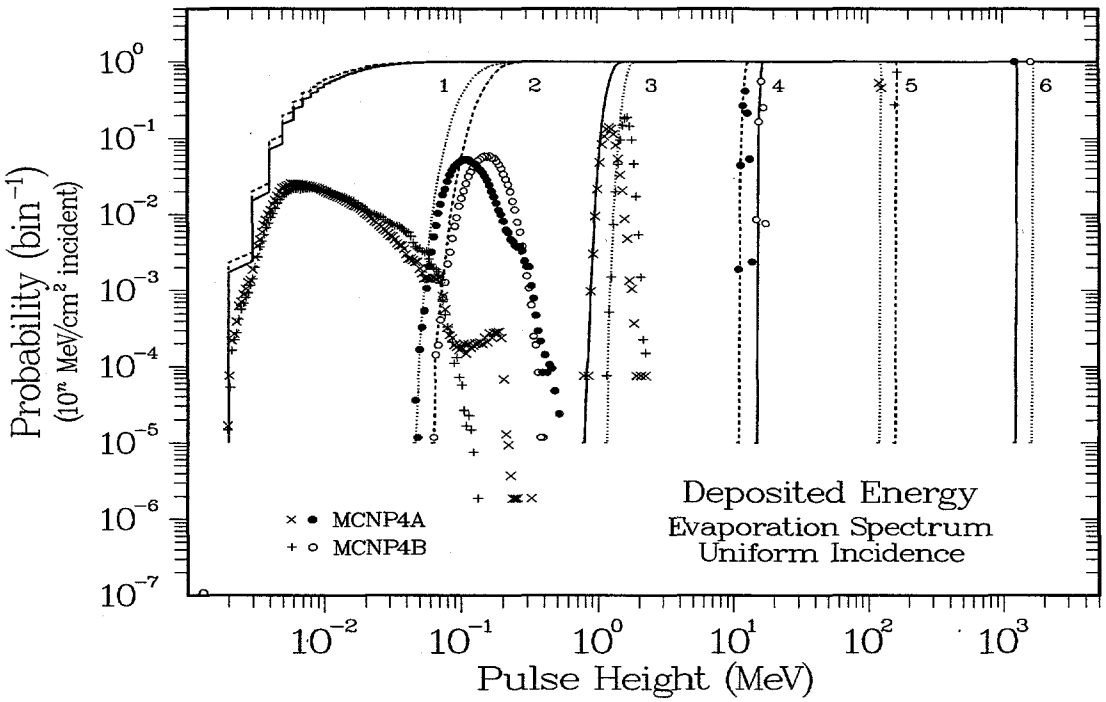

Figure 7.8. Single-tube threshold probabilities calculated from the pulse-height spectrum in Figure 7.7 at instantaneous gamma-ray fluences ranging from 1 to 10^{6} MeV/cm^{2} per pulse.

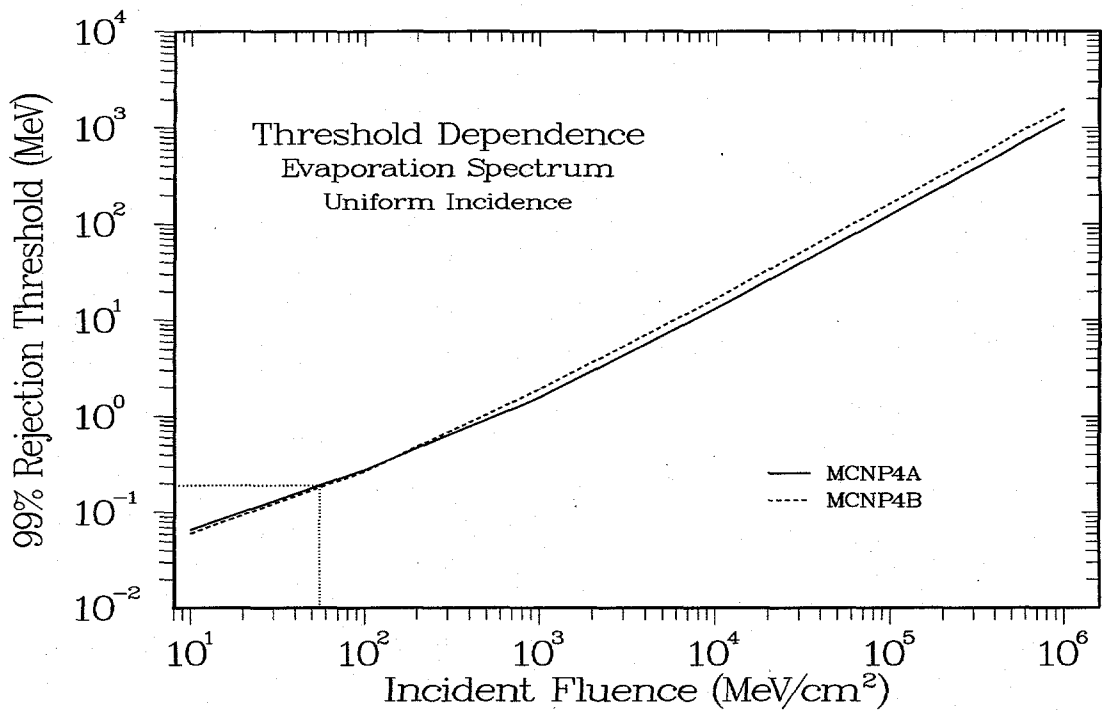

Figure 7.9. Pulse-height thresholds required to obtain 99% rejection probabilities for the incident fluences shown in Figure 7.8.

7.3. Discussion

Results. As discussed in Sec. 2.1, the major issue for the gamma-ray response of ^{3}He counters is the distinction between (1) the effect of pileup in exceeding the threshold for neutron pulse heights in the pulse-counting mode, versus (2) the proposed use of current measurements to replace pulse-counting at high neutron fluxes. Pileup effects are primarily an issue for the initial gamma-ray flash, which occurs before any source neutrons have arrived. If the threshold were exceeded, only a single count would occur in each tube; one count would be insignificant compared with the background rate, but then two-tube coincidence could still be identified in the subsequent analysis. The current measurements, however, may become important at high neutron rates, when it is necessary to estimate the slowly varying contribution from delayed gamma rays. Determining the relative sizes of the neutron and gamma-ray currents must consider both the source normalization factors and the mechanisms for energy-to-charge conversion for charged particles and electrons. Such topics are well beyond the scope of the present work. Only when the uncertainties in these unknown factors are established can we determine the significance of the present issues such as large statistical uncertainties or differences between the MCNP4A and MCNP4B codes.

8. SUMMARY AND CONCLUSIONS

Literature Survey. This report begins in Chap. 2 with a search for previous discussions of the response of nuclear instruments to gamma rays in the 0.1–10-MeV energy range of interest for our application. Surprisingly, there appears to be no general recognition of the importance of secondary electrons in determining the response of detectors whose active elements are relatively thin compared with the ranges of energetic electrons. In particular, there is little discussion of the relationship of electron transport to differences between SI energy absorptions and the MCNP heating or pulse-height tallies. In contrast, there is good appreciation of the importance of such interface effects in the field of medical physics, especially in regard to the calibration of ionization chambers or the use of Si diodes for radiation dosimetry. Thus, our central result in the area is the issuance of a stern warning to developers of gamma-ray instruments about the importance of secondary-electron responses, especially in the use of Si photodiodes as readout devices for scintillation detectors. Unless the optical signal is large enough to overwhelm any direct response of the diode to incident radiation, interpreting the response of such detectors may be very difficult indeed.

Slab-Geometry Calculations. Our own attempts to understand the physics connections between secondary-electron transport and detector response are contained in our test-setup calculations for the SAN and SPG detectors in Chap. 2 and for other detectors in Chap. 3. Clearly, the role of electron contributions must be considered carefully whenever the electron range becomes comparable to the thickness of the detector's active elements. Accordingly, for energies below 100 keV the photoelectric absorptions obtained from SI coefficients or MCNP heating tallies are generally reliable, but at energies above 1 MeV it is rarely reasonable to ignore electron effects. Nevertheless, even at these energies the effective areas that are obtained from macroscopic calculations such as SI absorptions and heating tallies are generally accurate for fully shielded detectors, even though the underlying microscopic results such as pulse-height distributions are completely erroneous. In particular, it is important to develop a general understanding of the relative effectiveness of different shielding materials for other applications involving similar detectors.

SPG Energy- and Angle-Dependent Effective Areas. Although the SPG effective-area calculations in Chap. 4 form the core of this report, their interpretation is relatively straightforward because of the extensive discussion of slab-geometry calculations. In particular, the observed energy dependence corresponds closely to that for the test setup, is almost flat across the entire range of greatest interest, and varies little as a function of incident angle. As shown in Chap. 5, attenuation across the detector produces a small difference between the responses of the individual rods, which provides the basis for an important technique for rejecting environmentally induced background events.

SPG Pulse Response. Knowing the average response of the detector to individual incident photons, however, does not provide the information needed to evaluate the detector's performance for pulsed sources. We have therefore developed a technique to build up the detector's pulse response starting from a properly normalized pulse-height spectrum, which can be easily measured or calculated. Our results clearly illustrate the behavior of the accumulated pulse-height spectra that result from arbitrary numbers of simultaneous incident photons. In particular, the broad pulse-to-pulse variations observed at low incident fluences are seen to gradually decrease in width as the intensity increases, with the average values eventually con-

verging to the results expected for nonstatistical operation. Further analysis of these pulse-height distributions provides clear connections between incident fluence, pulse-height threshold, and timing resolution. When constrained by the need to eliminate events caused by single minimum-ionizing particles and maintain reasonable timing resolution, these relationships provide good constraints on the detector's expected performance characteristics. These constraints allow an evaluation of the relative importance of the statistical uncertainties at low fluence values versus the systematic uncertainties caused by the unavoidable variations in detector response for different source energies and angles.

SAN Detector Response. The SPG effective-area and pulse-response calculations are repeated in Chap. 7 for the case of the SAN detector. Although it is difficult to accumulate meaningful statistics, the effective areas correspond well to the behavior expected from the slab-geometry calculations. In particular, the production of secondary electrons in the tube walls leads to a strongly enhanced response near 100 keV, and the efficiencies above 1 MeV are associated almost entirely with electron production in the walls and the surrounding polyethylene. An important difference from the SPG analyses emerges in the case of the detector's pulse response. Whereas pulse-pileup effects are important mainly for the possibility of exceeding the neutron pulse-counting threshold, the effective areas may be important throughout the entire neutron-detection regime if current measurements are proposed as a means for extending the detector's pulse-counting range.

Further Work. This report necessarily leaves some work unfinished. First, realization of the importance of electron transport requires that at least some of the APG calculations in Refs. 12 and 15 be redone to check the limitations of MCNP heating tallies, and similar calculations may be needed for other detectors that use Si photodiodes. Second, this report includes almost no comparisons with measurements because no prototype SPG and SAN instruments exist. Once such hardware is available, pulse-height comparisons for monoenergetic gamma-ray sources should be used to check the reliability of the calculations and determine the effect of the actual resolution functions. If possible, techniques should be devised to check the SPG and SAN pulse-response predictions and to compare the magnitudes of the SAN neutron and gamma-ray currents with those expected in practice. (Note: At the time of printing, measurements and calculations of pulse-height spectra were being made to validate the present conclusions.) Finally, some effort should be devoted to developing a simple analytical model of the effect of secondary electrons on detector response and shielding effectiveness. A starting point for such a model might be pre–Monte Carlo discussions of electron production and transport such as those found in Ref. 24. Such references include, for example, information about the derivation of the SI attenuation coefficients, including the Z dependence of average Compton cross sections and the thickness dependence of electron ranges. Much of the behavior observed in our calculations can be explained by the statements such as

(1) Compton scattering is by far the dominant mechanism for energy deposition in the energy range from 0.1 to 10 MeV;
(2) the resulting attenuation coefficients vary as Z/A, which is almost constant for different materials; and
(3) the range in g/cm^2 of the secondary electrons varies smoothly with energy and is independent of material.

Taken together, such statements could provide the basis for a non–Monte Carlo analytical model of shielding and energy-loss effects over the energy range of interest.

ACKNOWLEDGEMENTS

This report draws heavily on collaborations with members of the LANL Energetic-Particle Team in NIS-2. In particular, Tom Cayton not only provided guidance on electron-transport calculations, he also provided the up-to-date RSICC versions of the MCNP4B code and its electron and photon libraries. Jim Distel contributed to challenging discussions of the effect of secondary electrons on the response of related instruments such as XDS. David Lawrence of NIS-1 discovered the differences between the predictions of MCNP4A and MCNP4B for the case of ^{3}He counters, and he carried out the literature search on gamma-ray rejection techniques in such detectors. Finally, Ray Klebesadel, now long retired, pointed out the need for converting the calculations for single-photon pulse heights to the accumulated spectra for pulsed sources.

REFERENCES

1. R. C. Byrd, "Computer-Optimized Design of Polyethylene-Moderated ^{3}He Counters for Fast Neutrons," Los Alamos National Laboratory report LA-13695-MS (May 2000).
2. E. Storm and H. I. Israel, "Photon Cross Sections from 0.001 to 100 MeV for Elements 1 through 100," Los Alamos Scientific Laboratory report LA-3753 (November 1967).
3. R. C. Byrd, B. A. Barraclough, W. C. Feldman, and S. J. Bame, "Measurements and Calculations of the Characteristics of a Space-Based Neutron Sensor," Los Alamos National Laboratory report LA-12340-MS (October 1992).
4. R. W. Campbell and G. H. Anno, "The Response of Miniature G-M Tubes to Monoenergetic Gamma Radiation," Transactions of the American Nuclear Society **13** (1970) 533–534.
5. M. N. Agu and H. Petitcolas, "γ-Compensated Self-Powered Detectors for Reactor Instrumentation and Control," Measurement Science and Technology **1** (1990) 1047–1051.
6. T. Gozani and R. O. Ginaven, "Gamma Cancellation Technique—A New Approach to the Gamma-Flash Problem," Nuclear Instruments and Methods **76** (1969) 333–336.
7. R. A. DuBridge, "Campbell Theorem–System Concepts and Results," IEEE Transactions in Nuclear Science **NS-14** (1967) 241–246.
8. D. H. Beddingfield, H. O. Menlove, and N. H. Johnson, "Neutron proportional counter design for high gamma-ray environments," Nuclear Instruments and Methods in Physics Research **A442** (1999) 35–40.
9. "MCNP–A General N-Particle Monte Carlo Transport Code, Version 4B," Judith F. Briesmeister, Editor, Los Alamos National Laboratory report LA-12625-M, Version 4B (March 1997).
10. M. Slapa and M. Traczyk, "A New Concept of Dosimeter with Silicon Diodes," IEEE Transactions on Nuclear Science **43** (1996) 1855–1859.
11. N. Takeda et al., "A Development of NRESP Monte Carlo Code for the Calculation of Neutron Response Function for Gas Counters," Nuclear Instruments and Methods in Physics Research **A422** (1999) 69–74.

12. R. C. Byrd, "Calculations and Measurements of the Energy-Dependent Response of a Shielded Gamma-Ray Detector," Los Alamos National Laboratory report LA-13030-MS (March 1996).
13. M. C. Moxon and E. R. Rae, "A Gamma-Ray Detector for Neutron Capture Cross-Section Measurements," Nuclear Instruments and Methods **24** (1963) 445–455.
14. B. Nilsson, A. Montelius, and P. Andreo, "A Study of Interface Effects on Co-60 Beams Using a Thin-Walled Parallel Plate Ionization Chamber," Medical Physics **19** (1992) 1413–1421.
15. R. C. Byrd, R. W. Klebesadel, J. L. Longmire, S. G. Blair, and E. Noveroske, "Characteristics of a Sensor for Recording High-Intensity Gamma-Ray Pulses," Los Alamos National Laboratory report LA-13530-MS (Revised) (OUO) (1999) (available from the author).
16. J. P. Anthes, "X-ray Response of AlGaSA/GaAs Radiation-Hardened Double-Heterostructure Photodiode Compared to Si:p-I-n Photodiodes," Review of Scientific Instruments **59** (1988) 1846–1848.
17. W. Baird, W. P. Unruh, and G. O. Bjarke, "A Solid State Directional Gamma Detector," IEEE Transactions on Nuclear Science **33** (1986) 660–663.
18. M. Reier and G. H. Anno, "The Response of a Shielded 300-Micron Silicon Detector to Gamma Rays," Transactions of the American Nuclear Society **13** (1970) 534–535.
19. Y. Eisen, et al., "A Small Size Neutron and Gamma Dosemeter with a Single Silicon Surface Barrier Detector," Radiation Protection Dosimetry **15** (1986) 15–30.
20. W. R. Johnson, R. A. Causey, P. J. Rodi, and G. E. Carlson, "Development of a Wide Range Environmental Gamma-Ray Dosimeter," Nuclear Technology **60** (1983) 151–154.
21. C.-R. Chen, S.-H. Jiang, H.-H. Tseng, and H.-F. Chang, "Energy Response and Filter Compensation of PIN Si Photodiode for Personal Dosimetry Application," IEEE Transactions in Nuclear Science **40** (1993) 857–862.
22. R. C. Byrd, J. D. Drabanski, and B. L. Barraclough, "Monte Carlo Calculations of the Effective Area and Directional Response of a Polyethylene-Moderated Neutron Counter," Los Alamos National Laboratory report LA-12850-MS (January 1995).
23. R. C. Byrd and P. A. Russo, "Experimental Tests of a Radiation Direction Finder," Los Alamos National Laboratory report LA-13212-MS (November 1996).
24. R. D. Evans, *The Atomic Nucleus* (McGraw-Hill, New York, 1955), Chaps. 21 and 23.